NASA Contractor Report 3805

An Improved Viscid/Inviscid Interaction Procedure for Transonic Flow Over Airfoils

R. E. Melnik, R. R. Chow,
H. R. Mead, and A. Jameson

CONTRACT NAS1-12426
OCTOBER 1985

NASA

NASA Contractor Report 3805

An Improved Viscid/Inviscid Interaction Procedure for Transonic Flow Over Airfoils

R. E. Melnik, R. R. Chow,
H. R. Mead, and A. Jameson
Grumman Aerospace Corporation
Bethpage, New York

Prepared for
Langley Research Center
under Contract NAS1-12426

National Aeronautics
and Space Administration

**Scientific and Technical
Information Branch**

1985

ABSTRACT

This paper describes a new interacting boundary-layer approach for computing the viscous transonic flow over airfoils. The theory includes a complete treatment of viscous-interaction effects induced by the wake and accounts for normal pressure gradient effects across the boundary layer near trailing edges. The method is based on systematic expansions of the full Reynolds equation of turbulent flow in the limit of Reynolds numbers, $Re \to \infty$. The theory employs a local inner solution to describe the strong interaction region at trailing edges. Procedures are developed for incorporating the local trailing-edge solution into the numerical solution of the coupled full-potential and integral boundary-layer equations. Although the theory is strictly applicable to airfoils with cusped or nearly-cusped trailing edges and to turbulent boundary layers that remain fully attached to the airfoil surface, the method has been successfully applied to more general airfoils and to flows with small separation zones. Comparisons of theoretical solutions with wind-tunnel data indicate the present method can accurately predict the section characteristics of airfoils including the absolute levels of drag. The results of the study clearly demonstrate the importance of including both wake and normal pressure-gradient effects in the theoretical formulation and of using a fully conservative difference scheme in the solution of the inviscid equations. This study indicates that a simple interacting boundary-layer approach can be an effective tool for the prediction of viscous effects on airfoils.

ACKNOWLEDGEMENT

The authors gratefully acknowledge Dr. B. Grossman of Virginia Polytechnic Institute for his helpful discussions during the formulation of the problem.

TABLE OF CONTENTS

LIST OF ILLUSTRATIONS

LIST OF ILLUSTRATIONS (CONT)

LIST OF ILLUSTRATIONS (CONT)

LIST OF TABLES

NOMENCLATURE

a	Speed of sound
$a_{1,2,3}$	Compressibility parameters defined by Eqs (26) and (56)
A	Parameter defined by Eq. (53c)
B	Prandtl-Glauert Factor, $\sqrt{1-M_{te}^2}$
B_∞	Prandtl-Glauert Factor, $\sqrt{1-M_\infty^2}$
c	Airfoil chord
c_0	Parameter defined by Eq. (113c)
c_E	Entrainment function
c_f	Skin friction coefficient, $\tau_w/\frac{1}{2}\rho_e U_e^2$
c_2	Constant controlling the accuracy of the finite difference approximation
c_r, c_0	Parameters defined by Eq. (113c)
c_α	Parameter appearing in inviscid solution, Eq. (24)
c_w	Wake Momentum Coefficient, Eq. (9e)
C_L	Lift coefficient
C_0	$= 1 + (\gamma - 1) M_{te}^2$
$C_{1,2}$	Constants defining wake function, Eq. (44)
D	Scaling parameter defined by Eq. (65d) and (74f)
E	Circulation at infinity divided by 2π
f	Law-of-the-wake function, Eq. (15)
F	Law-of-the-wall function, Eq. (16)
$F_{1,2}$	Particular integral defined by Eq. (43)
$g_{1,2}(z)$	Analytic functions defined by Eqs. (46) and (47)
G	Reduced potential function, Eq. (79a)
h, $\bar{h}$	Boundary Layer Shape Factors, Eq. (102)
$h_{1,2}$	Law of wake functions defined by Eq. (35c)
$\mathcal{H}$	Modulus of transformation multiplied by $\bar{r}$
I, $\bar{I}$	Functions defined by Eq. (67)
J_w	Functions defined by Eq. (71b)
k	von Karman constant (0.41)
$K, \bar{K}$	Functions defined by Eqs. (64) and (65)
M	Mach Number
n,s	Coordinates normal and tangent to airfoil and wake surface

$\bar{n}$	Stretched normal coordinate (n/τ)
p	Static pressure in the boundary layer
$\tilde{p}$	Static pressure in the trailing edge region
$\bar{p}$, $\hat{p}_{1,2}$	Perturbation pressure defined by Eqs. (24) and (38)
p_σ	Pressure function appearing in the matching conditions, Eq. (6b)
P	static pressure in the outer inviscid region
$\mathcal{P}$	Static pressure in the composite solution
q_r, q_ω	Physical velocity components in the radial and azmuthial directions, Eq. (77)
Q_c	Parameter controlling the switch from backward to forward differences
Q_r, Q_ω	Computational velocity components Eq. (76)
r, Ω	Local polar coordinates, trailing edge region
$\bar{r}, \omega$	Polar coordinates in circle plane
R	Density in the outer inviscid region
$\mathcal{R}$	Density in the composite solution
Re	Reynolds number
t	Independent variable defining wake function Eq. (44)
$\mathcal{T}$	static temperature
u, v	Velocity components in the boundary layer
$\tilde{u}, \tilde{v}$	Velocity components in the trailing edge region
$\bar{u}, \bar{v}$	Velocity components defined by Eq. (24)
u^*	Friction velocity $\sqrt{\tau_w/\rho_e} \approx O(\epsilon)$
U, V	Velocity components in the outer inviscid region
$U_1, V_1, \hat{U}, \hat{V}$	Normalized inviscid velocity functions defined by Eqs. (24d) and (40b)
v_σ	Surface source velocity, Eq. (6a)
v_w	Source velocity discontinuity in the wake, Eq. (9d)
$\mathcal{U}, \mathcal{V}$	Velocity components in the composite solution
W	Law-of-the-wake function, Eqs. (15b) and (44)
x, y	Stretched local cartesian coordinates, trailing edge region Eq. (21)
z	Complex coordinate, trailing edge region $(z = \zeta + i\eta)$

α	angle of attack
β	flow angle
$\beta_{1,2}, \bar{\beta}_{1,2}$	Real part of complex function, $g_{1,2}(z)$ defined by Eqs. (45) and (52)
γ	Ratio of specific heats
γ^*	Law of wall parameter defined by Eq. (36)
Γ	Wake circulation function defined Eq. (11b)
δ	Boundary layer thickness
δ^*	Displacement thickness
δ_w^*	Wake displacement thickness $\delta_w^* = \delta_+^* + \delta_-^*$
ϵ	Small parameter that is $O(u^*/U_\infty) \approx O(\ell n\ R_e)^{-1}$
$\hat{\epsilon}$	Small parameter equal to the ratio of sublayer to boundary layer thickness $(\tau^2 R_e)^{-1}$
$\bar{\zeta}$	Perturbation vorticity
η, ξ	Scale cartesian coordinates, trailing edge region defined by Eq. (34)
θ	Momentum thickness
κ	Wake streamline curvature $d\beta/ds$
λ	Weighting factor in partially conservative scheme and parameter defined by Eq. (72b)
$\lambda_{1,2}$	Complex pressure-flow deflection, Eq. (40c)
$\tilde{\pi}$	Coles wake parameter
ν	Scaled polar coordinate, trailing edge region, Eq. (34)
ρ	Density in the boundary layer region
ρ_∞	Free Stream Density
σ_d	Mass flow constant in Eq. (79c)
$\sigma_{1.2}$	Imaginary part of complex function $g_{1,2}(z)$ defined by Eq. (45)
τ_w	Wall shear stress
Φ	Velocity potential, outer inviscid region
χ	Law of the wake stream function $\int_o^y f(y)dy$
$\bar{\psi}$	Perturbation stream function, trailing edge region
ψ_1	Normalized inviscid stream function defined by Eq. (24e)
$\bar{\omega}, \hat{\omega}$	Perturbation flow deflection defined by Eq. (32a) and (38b)
$[\![\ ]\!]$	Denotes jump across the wake

Subscripts

cp	Denotes "common part"
e	Denotes boundary layer edge values and inviscid flow surface values
i,j	Mesh point indices
p	Particular solution
te	Trailing edge
w	Denotes wake edge values and inviscid flow values at wake axis
∞	Free stream
+,-	Denotes upper, lower surface value

Superscripts

(1), (2)	Perturbation indices
+,-	Denotes upper, lower surface value

ABBREVIATIONS

BGKJ	Bauer, Garbedian, Korn and Jameson Method
F-C	Fully - Conservative
GK1	Garabedian - Korn 1 Airfoil
IBLT	Interacting Boundary Layer Theory
LaRC	Langley Research Center
NS	Navier-Stokes
NAE	National Aeronautical Establishment (Canada)
N-C	Non-Conservative
P-C	Partially - Conservative
RAE	Royal Aircraft Establishment (Great Britain)

1. INTRODUCTION

The development of theoretical methods for the prediction of the section characteristics of airfoils has always been an important problem area in aerodynamics. It continues to receive much attention today, with interest focusing on the numerical solution of various theoretical models for the viscous flow over airfoils. Recent advances in numerical techniques for solving the full non-linear potential equation have led to practical methods for computing the lift and drag of inviscid transonic flows containing shock waves (Refs. 1, 2 & 3). It is, however, well known that viscous effects are important and must be taken into account in these flows if accurate section characteristics are to be predicted. This is particularly true for supercritical flow over rear-loaded airfoils for which the combination of shock waves and aft camber combine to produce significantly thickened boundary layers over the rear upper surface. This in turn leads to much larger viscous effects than are experienced on conventional airfoils in supercritical flow. For heavy rear loading, the boundary layer can reduce the lift by a factor of two below inviscid levels, even at Reynolds numbers as large as 10^7.

In most practical problems the Reynolds number is large, the boundary layers are mostly turbulent, and the direct effects of viscosity and turbulent transport are confined to thin shear layers on the airfoil surface and along the wake. In these situations the viscous flow can be effectively analyzed by interacting boundary-layer theory (IBLT) in which the flow field is divided into a primary inviscid region, thin shear layers, and localized strong-interaction regions. Previous applications of the theory to airfoils used a highly simplified formulation based on the neglect of pressure variations across the shear layers and neglect of all interaction effects induced by the wake. This formulation led to a description in terms of the coupled inviscid and Prandtl boundary-layer equations which are solved by standard iterative schemes. These theories account for the primary viscous effect due to the displacement thickness on the airfoil but do not properly treat viscous effects due to the wake and in shock-wave/boundary-layer and trailing-edge interaction regions.

The new formulation developed in the present study extends the conventional boundary-layer approach to include a full treatment of the wake and normal pressure-gradient effects at the trailing edge. Our method is based on systematic expansions of the full Reynolds equation of turbulent flow in the limit of Reynolds number, $Re \to \infty$. The method of matched asymptotic expansions leads to a description of the flow in terms of inviscid regions and thin shear layers near the airfoil and wake. A local inner solution is developed to correct the standard Prandtl boundary-layer formulation for strong-interaction effects at the trailing edge. This work can be viewed as an extension and further development of Melnik and Chow's turbulent-interaction theory previously described in Refs. 4 & 5. The method is applicable for high Reynolds number flow over general airfoil shapes with cusped or nearly cusped trailing edges and free-stream Mach numbers less than one. The method is intended for flows that are turbulent over most of the airfoil and that are not separated. However, provisions were made to allow for the presence of small separation zones so that the resulting code will function and provide at least a rough description of the solution for these cases.

The formulation of the present paper employs a version of the mixed-flow relaxation technique developed by Jameson (Refs. 6 & 7) for solving the full-potential equation in conservation form*. The method employs a conformal mapping of the airfoil to a circle to obtain a useful computational grid and uses a direct solver to accelerate convergence. The inviscid boundary conditions are modified to account for viscous effects using a surface-source formulation of the matching conditions thus avoiding the need to carry out repeated conformal mappings as required in displacement-thickness approaches. An iterative scheme is employed to obtain a self-consistent solution of the coupled boundary-layer and inviscid-flow equations. The viscous matching conditions employed in the theory account for displacement effects on the airfoil as well as both wake-thickness and wake-curvature effects. The local inner solution developed in Ref. 5 is used to correct the standard boundary-layer solution for strong-interaction effects at the trailing edge. The modified viscous method accounts for the significant pressure variation across the

- - - - - - -

*A nonconservative option is also provided in the computer code.

boundary layer and removes the nonuniformity of classical boundary-layer theory near trailing edges. The resulting theory provides a completely rational treatment of the trailing-edge region for cusped airfoils at lift. It does not account for the additional nonuniformity arising on airfoils with sharp but non-cusped trailing edges. However, this nonuniformity can be ignored and the resulting computer code can be applied to general airfoils with nonzero included angles. Results given later in the paper indicate that the method gives good overall results for airfoils with small trailing-edge angles (less than 10°).

The present theory also does not provide for a proper treatment of the strong-interaction phenomenon near shock-wave/boundary-layer interaction zones. It ignores the fact that the boundary-layer approximations fail in these regions and determines the solution with a conventional interacting boundary-layer formulation. Nevertheless, results obtained with this code reported in Refs. 5 & 8, and in the present study indicate that the method yields remarkably accurate results for the pressure distribution near shock waves.

The boundary-layer development on the airfoil and in the wake is determined from simple integral methods. The laminar boundary layer starting from the stagnation point is computed by an extention of Thwaites' method to compressible flow (Ref. 9). A transition to turbulent flow is made at a given point on the airfoil on the basis of either assigned position or by the use of established transition criteria. The method also checks for leading-edge separation and whether it is of the long or short bubble type and then assigns transition at the separation point. The development of the turbulent boundary layer and wake downstream of transition is determined from the lag-entrainment method of Green et al. (Ref. 10).

Calculations carried out with a preliminary version of code (Refs. 5 & 8) employed a great deal of numerical smoothing of the surface-pressure distribution and boundary-layer parameters near the shock wave and trailing edge. It has since been determined (Ref. 11) that the smoothings were responsible for the "spiked" pressure distributions observed near the trailing edge in these early studies. We have also found that numerical smoothings are not necessary for convergence and they have, therefore, been eliminated from the method.

There have been a number of other recent attempts to incorporate boundary-layer corrections into full-potential flow codes. The work of Bauer, Garabedian and Korn (BGK) (Ref. 12) is based on a non-conservative (N-C) treatment of the full potential equation and a Nash-McDonald integral method for the turbulent boundary layer. It does not solve for the laminar boundary layer near the leading edge and does not use transition criteria to start the turbulent flow. It treats boundary-layer displacement effects on the airfoil through a displacement-thickness formulation, requiring repeated conformal mappings of the equivalent airfoil to a circle. Similar methods have also been developed by Bavitz (Ref. 13) and Carlson (Ref. 14). These methods take no account of wake-induced viscous effects nor strong-interaction effects near shock waves or trailing edges. They all employ extensive numerical smoothings which are apparently needed to assure convergence of the inviscid/boundary layer iteration. These codes also contain adjustable parameters which can be used to improve agreement with experiment. The non-conservative formulation employed in these methods leads to the generation of spurious mass at the shock wave which causes an extra "sink" drag. A post-solution correction for the spurious sink drag was added to a later version of the BGK code (Ref. 15) resulting in improved drag predictions.

A similar method was also developed by Lock and Collyer (Refs. 16, 17 & 18) of the Royal Aircraft Establishment (RAE). They employed a more complete boundary-layer formulation, similar in many respects to the present method. A surface-source formulation was used to represent displacement effects on the airfoil with both wake-thickness and wake-curvature terms included in the matching conditions. However, strong interaction effects at the trailing edge were not taken into account. Numerical difficulties in implementing the wake-curvature condition were reported and extensive numerical smoothing of the solution near the trailing edge was required to obtain converged solutions. It is likely that the neglect of strong interaction at the trailing edge was at least partially responsible for these problems.

There has been some controversy regarding the proper choice of differencing, fully-conservative (F-C) or non-conservative, to be used in these calculations. As mentioned previously, non-conservative differencing introduces large errors into the drag prediction that require correction. There are also indications (Refs. 5, 8 & 11) that the pressure rise across the shock wave is underestimated with a non-conservative formulation. Lock (Ref. 19) also produced some results with a version

of the RAE viscous method employing a quasi-conservation formulation showing shock waves that are too far aft. To improve the performance of their method, a partially conservative (P-C) scheme was also developed by the RAE (Ref. 18) consisting of a linear combination of non-conservative and quasi-conservative differencing. The method contained an arbitrary parameter, λ, that defines the weighting of the non-conservative and quasi-conservative formulae, and which was adjusted to obtain good agreement in shock position for a few selected cases. The present study indicates that the fully-conservative method clearly gives the best predictions of shock position, shock strength, and drag provided that the complete boundary-layer formulation of the present method is employed in the computations.

It is difficult to form a firm opinion regarding the adequacy of interacting boundary-layer theory for the airfoil problem on the basis of results obtained with either the BGK or RAE methods. The neglect of potentially important viscous effects in the theoretical formulation and the use of extensive numerical smoothing and adjustable parameters in the computer code definitely obscure the meaning of the results obtained to date. The shortage of reliable experimental data with boundary-layer information and the uncertainties associated with wind-tunnel wall effects have also impeded progress on the evaluation of the theoretical methods. Accurate Navier-Stokes (NS) solutions obtained on fine grids could fill this void but, unfortunately, suitable solutions have not yet appeared in the literature.

The present work is a step in the direction of eliminating some of the above problems. For airfoils with cusped trailing edges, the present method includes all of the leading-order viscous terms consistent with a rational asymptotic analysis, aside from the neglect of normal pressure gradient effects at shock waves. The absence of these latter effects in the theoretical model does not appear to be of great consequence if the shock wave is not "too close" to the trailing edge. The present method also avoids all numerical smoothings, contains no adjustable parameters (aside from those appearing in the turbulence model and transition criteria), and yields accurate solutions to the interacting boundary-layer equations unencumbered by extraneous numerical issues. The organization of the remainder of this paper is outlined below.

In Section 2 we describe the viscous-interaction formulation used in the present work including a brief description of the classical boundary-layer formulation and an outline of the Melnik-Chow strong-interaction trailing-edge theory. In Section 3 we describe the boundary value problem governing the outer inviscid flow and outline the numerical procedures used to solve the inviscid equations. In Section 4 we discuss the methods used to determine the solution in the laminar and turbulent boundary layers and to evaluate the matching conditions. In Section 5 results are given for various airfoils which illustrate the importance of the individual viscous effects that appear in the theoretical model. These include wake thickness, wake curvature, and strong interactions at the trailing edge. Comparisons with experimental data are also provided including some date for several important boundary-layer quantities. In Section 6 we discuss the significance of this work, summarize the principal conclusions of the study, and identify related problem areas requiring further research. An epilogue is presented in sections which summarizes some improvements that have been made to the method since a preliminary version of this report was completed in 1980.

2. VISCOUS FLOW THEORY

In this section we describe the viscous flow formulation employed in the present work. We will review conventional boundary-layer theory, describe the development of the local trailing-edge solution, and will indicate how the conventional matching conditions can be corrected for strong interactions at the trailing edge. We first briefly review previous theoretical studies of viscous interaction on airfoils.

2.1 BACKGROUND

Traditionally, two classes of methods have been used for viscous interactions on airfoils at high Reynolds numbers. One is based on the direct numerical solution of the full Reynolds equations of turbulent flow (Ref. 20) while the second is based on Interacting Boundary Layer Theory (IBLT) (e.g., see Ref. 21). A combination of these methods leading to a direct numerical solution of a "thin-layer" or parabolized approximation to the full Reynolds equations have also recently appeared (Refs. 22, 23 & 24). Although methods based on the numerical solution of the full or approximate Reynolds equations should be expected to yield the best solutions, they have obtained only qualitative results to date. The methods are computationally expensive and, consequently, have suffered from poor resolution due to the use of coarse meshes - particularly in the streamwise direction. At present, it seems that more accurate solutions can be obtained with far less computing time with a boundary-layer type approach that takes advantage of the availability of fast numerical methods for solving the full-potential equation. These methods permit the use of relatively fine grids leading to solutions with good spatial resolution. Because of their basic simplicity and high speed, boundary-layer methods have gained widespread favor in the engineering community.

It should be noted, however, that although boundary-layer methods have been used for many years and have become one of the standards methods for computing viscous flows over airfoils, a completely satisfactory interacting boundary-layer formulation for this problem has not yet been achieved. The standard boundary-layer approach leads to a description of the flow in terms of coupled inviscid and boundary-layer equations which are solved by iteration to obtain self-consistent

solutions. The theory is based on an asymptotic expansion of the full viscous equations in the limit of Reynolds number, $Re \to \infty$. The asymptotic theory leads to a formal derivation of the matching conditions coupling the inviscid and viscous flows. In this way, several terms appear in the matching conditions, all of which should be included in a consistent, lowest-order description. Unfortunately, in most previous works potentially important terms associated with the wake have been dropped from the matching conditions. In addition, there are local failures of the boundary-layer approximations in strong-interaction regions near shock waves and trailing edges. Thus, a complete interacting boundary-layer formulation should, in principle, consider all of the following factors:

- displacement-thickness effects on the airfoil
- displacement-thickness effects in the wake
- wake-curvature effects
- strong-interaction effects at the trailing edge
- strong-interaction effects at shock waves.

The relative magnitude of these effects can be expressed in terms of a basic small parameter, ε, related to the Reynolds number, Re, such that ε vanishes as $Re \to \infty$. For turbulent flow it is convenient to identify ε with a typical value of the friction velocity on the airfoil surface. For the choice $\varepsilon = O(1/\ell nRe)$, the boundary-layer thickness, δ, is $O(\varepsilon)$ and the displacement and momentum thicknesses, δ^* and θ, are both $O(\varepsilon^2)$. The boundary-layer formulation can be developed in a formal asymptotic expansion in the limit $\varepsilon \to 0$. A formal asymptotic theory has been developed for non-interacting turbulent boundary levels by Mellor (Ref. 25), Bush and Fendell (Ref. 26), Yajnik (Ref. 27), and Afzal (Ref. 28) leading to a boundary layer with a law-of-the-wake/law-of-the-wall, two-layer structure.

The displacement effect arises from a matching of the inviscid and boundary-layer solutions. It produces an $O(\varepsilon^2)$ perturbation to the outer inviscid solution which can be incorporated into the solution through the concept of an equivalent displacement body or equivalent source flow at the surface. In the first approach, the equivalent body is formed by adding the boundary-layer displacement thickness to the airfoil and trailing streamline, while in the source formulation, sources and sinks are placed on the airfoil and trailing streamline. The equivalence of these formulations (and others) was demonstrated by Lighthill (Ref. 29). The works of Stuper (Ref. 30) (1933), Pinkerton (Ref. 31) (1936), and Nitzberg (Ref. 32)

(1946)-in a rough-way, and Preston (Refs. 33 & 34) (1945, 1949) more accurately, were the first to apply the Prandtl boundary-layer theory to compute displacement effects on airfoils. Preston used the surface-source formulation to account for displacement effects on both the airfoil and wake by distributing sources and sinks along the airfoil and wake. These methods have come into common usage although there has been a tendency in recent work to ignore, without justification, the displacement effects induced by the wake.

The wake-curvature effect arises from the turning of low momentum fluid in the wake along curved streamlines. The turning of the flow induces a pressure drop across the curved wake that leads to additional terms in the matching conditions. These terms enter the formulation of the outer inviscid problem through a boundary condition specifying a discontinuity in pressure along the trailing streamline. The magnitude of the effect is $0(\varepsilon^2)$ and it produces effects on the outer inviscid flow that are similar to a jet flap with a negative jet-momentum coefficient of strength $0(\varepsilon^2)$. From this is follows that wake curvature leads to a reduction in left that is the same order as that produced by the displacement thickness. The importance of the wake-curvature effect and its relationship to the jet flap was first noted by Preston (Ref. 35) in 1954 (see also Spence and Beasely - Ref. 36). However, serious attempts to include wake-curvature effects in interacting boundary-layer calculations were not undertaken again until the mid 1970's in a series of papers by Firmin, Hall, Lock, and Coyller of the RAE (Refs. 16-19 and 37-39) and by the present authors in Refs. 4, 5 and 8. Although there were differences in the individual results, all displayed significant effects of wake-curvature on section characteristics.

Interacting boundary-layer theory, as just described, is not uniformly valid at trailing edges of airfoils. Non-uniformities in the theory are caused by singularities in the inviscid solution for the pressure gradient and streamline curvature at the trailing edge and by the change in the no-slip condition across the trailing edge. The singularities of the inviscid solution lead to large local streamline curvatures and to a breakdown of the boundary-layer approximations near trailing edges. Because of this non-uniformity, the pressure can no longer be regarded as constant across the boundary layer near trailing edges. This is especially important since pressure variations across the boundary layer affect the Kutta condition and, therefore, lead to relatively large global effects. Two types of singularities arise in the outer inviscid solution. One is related to lift and

arises at the trailing edge of any lifting airfoil carrying a non-zero load at the trailing edge. The second, due to the stagnation point singularity, appears at the trailing edge of an airfoil with a non-zero included angle.

An analysis of the strong interaction problem associated with lift was initiated by the first two authors in Ref. 4 and completed in Ref. 5. In these papers it was shown that the inviscid flow leads to square root singularities in the pressure gradient and wake curvature at the trailing edge and that, as a result, normal pressure gradients were important in the boundary layer near the trailing edge, and must be retained in a consistent description of the flow in these regions. It was also concluded that a self-consistent boundary-layer formulation and the related concept of an equivalent displacement body was not valid near trailing edges in turbulent flow.

A rational asymptotic theory was developed to describe the local flow near trailing edges of cusped airfoils. The analysis was carried out for compressible flow under the assumption that the flow as subsonic in the immediate vicinity of the trailing edge. It was also assumed that the boundary layer was an attached, fully-developed turbulent flow near the trailing edge and that the velocity profiles could be adequately represented by Cole's law-of-the-wake/law-of-the-wall form. Under these assumptions, it was shown that, in the limit $\varepsilon \to 0$, the boundary layer developed a three-layer structure near the trailing edge that is a generalization of the two-layer structure arising in non-interacting boundary layers. The three-layer structure extended over a streamwise extent of the order of a boundary-layer thickness (i.e., $O(\varepsilon)$). The pressure distribution was completely determined from the solution in the outermost region, encompassing most of the boundary layer. To leading order, the flow in the outer region is governed by linearized inviscid, rotational flow equations. The dominant vorticity in the trailing-edge region is "frozen" along the streamlines of the inviscid flow and is therefore completely determined by the upstream velocity profiles.

The theoretical model accounts for both the pressure variation across the boundary layer and for the vorticity in the boundary layer. The two inner layers were asymptotically thin compared to the outer, inviscid shear layer and, hence, did not effect the latter to lowest order. Thus, the solution of the outer problem for the pressure distribution was independent of the Reynolds stresses and closure

assumptions except through their influence on the shape of the velocity profile just upstream of the trailing-edge region. Analytic solutions were given for the local trailing-edge problem in Ref. 5. These solutions showed that the pressure perturbations generated in the trailing edge region are $O(\varepsilon^{3/2})$ which is an order of magnitude larger than the $O(\varepsilon^2)$ disturbances generated by conventional displacement and wake-curvature effects.

Similar interaction effects are also expected from the non-uniformity associated with the stagnation point singularity arising on airfoils with non-zero trailing-edge angles. Theoretical evidence indicates that the turbulent interaction changes the pressure by O(1) from the stagnation pressure arising in the inviscid solution. Thus, this effect is clearly larger than the others considered so far and can be expected to have important effects on the drag of airfoils with wedge-shaped trailing edges. Unfortunately, definitive studies of this important strong-interaction problem have not yet been carried out.

Aside from the non-uniformities stemming from singularities in the inviscid pressure distribution, an additional non-uniformity arises from the discontinuous change of the no-slip boundary condition across the trailing edge. The jump in boundary condition at the trailing edge causes an additional breakdown of the interacting boundary-layer solution. A similar effect arises in laminar flow with the transition of the laminar boundary layer to a wake across the trailing edge. In this case, local asymptotic solutions were developed for the non-lifting flat plate by Stewartson (Ref. 40), Jobe and Burggraf (Ref. 41), Veldman and van de Vooren (Ref. 42), and Chow and Melnik (Ref. 44) and for the lifting case by Brown and Stewartson (Ref. 43) and Chow and Melnik (Ref. 44). These solutions were based on the triple-deck theories of laminar interacting flows. Unfortunately, because of the difference in structure of laminar and turbulent flows, the laminar triple-deck theories do not apply to the turbulent problem. In turbulent flow the transition of the boundary layer to a wake is largely controlled by the law-of-the-wall region which has no counterpart in laminar flow. Since the law-of-the-wall region is exponentially thin compared to the boundary-layer thickness, the transition process will have no effect on the leading-order outer solution for the pressure distribution in turbulent flow, while in laminar flow it has a dominant effect. In general, the turbulent boundary layer/wake transition process in the wall layer will have only a higher-order effect on the outer solution and need not be considered in the solution

for the pressure distribution and section characteristics. However, for a symmetric, cusped airfoil at zero incidence the pressure-induced, strong interaction vanishes and the local flow is dominated by the turbulent boundary/layer/wake transition which then becomes the most important interaction effect near the trailing edge. Although there have been some exploratory studies of this latter problem by Robinson (Ref. 45) in 1967 and more recently by Alber (Ref. 46), these works were not definitive and they did not establish the correct asymptotic flow structure at large Reynolds numbers. Fortunately, the lack of knowledge of this aspect of the solution will only affect higher-order terms and need not be taken into account in order to determine the leading-order solution for the pressure, lift and drag.

For transonic flow an additional strong interaction arises at points where shock waves impinge on the boundary layer. In turbulent flow, discontinuities in pressure across the shock wave induce corresponding discontinuities in displacement thickness (Refs. 47-48), leading to a breakdown of theories based on an interacting boundary-layer description. The shock wave penetrates into the boundary layer and generates large pressure variations across the layer that invalidate the standard boundary layer approximations.

Rational asymptotic theories, recently developed (Refs. 47-53) to describe shock-wave/turbulent boundary-layer interactions, are based on a large Reynolds number ($\varepsilon \to 0$) asymptotic expansion of the full Reynolds equations. The boundary layer develops a multi-layer structure, similar to the turbulent trailing-edge interaction discussed previously. The pressure disturbances generated by the interaction were shown to be the order of ε x (shock strength) and hence larger than the classical displacement effect for shock strengths greater than $0(\varepsilon)$. The analyses in Refs. 47-53 considered weak shock waves of various strengths. It was also demonstrated in these works that the shock strength required to separate a turbulent boundary layer is 0(1). These works considered only local behavior and did not address the question of integrating these solutions into a complete airfoil problem. Fortunately, this is not a major concern here since the normal pressure gradient effect in shock-wave/boundary-layer interactions seem to have only a highly localized effect on the pressure distribution. Alternative formulations of shock-wave/boundary-layer interactions in the turbulent flow have also been proposed recently by Inger and his co-workers (Refs. 54 & 55). This work was based on application of Lighthill's laminar interaction theory (Ref. 56) to the turbulent

problem. Inger's theory represents an ad-hoc approach to the problem that is not related to a rational asymptotic description of the flow.

2.2 INTERACTING BOUNDARY-LAYER THEORY

We consider the problem of a uniform viscous flow over an airfoil of chord, c, free-stream speed, U_∞, and density, ρ_∞, at an angle of attack, α, and Mach number, M_∞. The main assumptions of the work are that the Reynolds number Re is large in an asymptotic sense and the free-stream Mach number is less than one. Under these conditions the problem can be analyzed by rational asymptotic methods based on expansions of the full Reynolds equations in the limit $Re \to \infty$ or $\varepsilon \to 0$. In this limit, a boundary-layer type flow structure develops as sketched in Fig. 1. The flow outside the strong-interaction region can be described by a standard inviscid/boundary-layer formulation with conventional matching conditions coupling the solution. In the standard approach, the solution in the outer region is represented by a sum-type asymptotic expansion. The solution in the outer region is inviscid to all orders, apart from exponentially small terms, with the leading term given by a solution to the full non-linear inviscid equations. Second and higher-order terms of the outer solution are governed by linearized inviscid flow equations.

This representation is somewhat inconvenient for supercritical flows because of the need to deal with perturbations of discontinuous solutions. This problem can be avoided by use of a slightly different representation for the outer solution. In

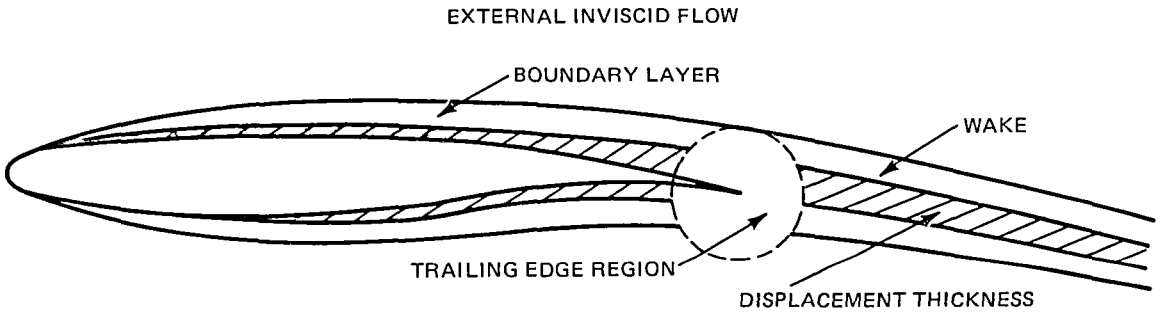

Figure 1 Flow Field Regions at High Reynolds Numbers

this alternative formulation, the outer inviscid flow is governed to all orders, by the full non-linear inviscid-flow equations with boundary conditions on the airfoil and in the wake determined from the viscous matching conditions. Higher-order viscous effects on the outer inviscid flow appear only through the matching conditions. Thus, in this formulation the full non-linear inviscid equations must be solved repetitively, employing successively improved matching conditions.

The form of the solution in the inner boundary-layer region depends on whether the boundary layer is a laminar or turbulent. In the laminar case, the solution has the form given by higher-order boundary-layer theory with the leading term governed by the usual non-linear Prandtl boundary-layer equations. For turbulent boundary layers, the form of the solution changes because of the two-layer structure of turbulent boundary layers at high Reynolds numbers. The appropriate asymptotic theory has been worked out for fully-developed turbulent boundary layers in Refs. 25-28. The leading-order solution is governed by boundary-layer equations with linearized convective terms. However, the usual non-linear boundary-layer equations do provide a composite equation that is valid to second-order in both the wake and wall regions of the turbulent boundary layer. In the present work we follow the composite equation approach and use the standard non-linear boundary-layer equations to describe the flow in both the laminar and turbulent boundary-layer regions.

The outer inviscid and inner boundary-layer solutions can be combined in the usual fashion to form a single composite expression that is uniformly valid in both regions. We employ curvilinear coordinates (s,n) and corresponding velocity components ($\mathcal{U}$,$\mathcal{V}$) along and normal to the streamline defining the airfoil and wake. In this study we employ nondimensionalized quantities with the velocities and density normalized by free stream velocity and density (U_∞, ρ_∞), the pressure and shear stresses by twice the dynamic pressure, ($\rho_\infty U_\infty^2$) and all lengths are scaled by the chord (c) of the airfoil. Composite expressions are denoted by the upper case script letters. The composite solution for the velocity components and the pressure are then represented in the form of a sum of the inviscid solution (capital letters) plus boundary layer solution (lower-case letters) minus the common part (subscript cp) as follows:

$$\mathcal{U} = U(s, n; v_\sigma; [\![V]\!]; \Gamma) + u(s, \bar{n}) - u_{cp}(s, \bar{n}) \qquad (1a)$$

$$\mathcal{U} = V(s, n; v_\sigma; [\![V]\!]; \Gamma) + v(s, \bar{n}) - v_{cp}(s, \bar{n}) \tag{1b}$$

$$\mathcal{P} = P(s, n; v_\sigma; [\![V]\!]; \Gamma) + p(s, \bar{n}) - p_{cp}(s, \bar{n}) \tag{1c}$$

where $\bar{n}$ is a stretched inner variable defined by

$$\bar{n} = n/\epsilon \tag{2}$$

Similar expression are also assumed for the density, $\mathcal{R}$, and temperature, $\mathcal{T}$. The quantities, v_σ, $[\![V]\!]$ and Γ appearing in the inviscid solution are functions entering the boundary conditions that are determined by matching the inviscid and boundary-layer solutions. The function $v_\sigma(s)$ specifies the source velocity on the surface of the airfoil, $[\![V(s)]\!]$ specifies the jump in source velocity across the wake and $\Gamma(s)$ is the circulation distribution along the wake. For an inviscid flow all three functions are zero as are the contributions from the boundary-layer and common-part term in the above representation. The solution is then given by the first term with boundary condition $V(s,o) = 0$.

If $u(s,\bar{n})$ and $\rho(s,\bar{n})$ are the boundary-layer solutions for the streamwise velocity and density profiles, the boundary-layer solution for the normal component of velocity and pressure distribution can be written in

$$v(s, \bar{n}) = v(s, 0) - \frac{d\rho_e U_e}{\rho_e ds}\, n + \frac{d}{\rho_e ds} \int_0^n (\rho_e U_e - \rho u)\, dn + 0(\epsilon^3) \tag{3a}$$

$$p(s, \bar{n}) = p(s, 0) - \kappa(s)\, \rho_e U_e^2\, n + \kappa(s) \int_0^n (\rho_e U_e^2 - \rho u^2)\, dn + 0(\epsilon^3) \tag{3b}$$

where $\kappa(s)$ is curvature of the airfoil or the wake streamline and where ρ_e and U_e are the surface values of the inviscid solution defined by

$$\rho_e(s) = \lim_{n \to 0} R(s, n) \tag{4a}$$

$$U_e(s) = \lim_{n \to 0} U(s, n) \tag{4b}$$

We introduce here the definitions of the surface values of the normal velocity and pressure from the outer inviscid solution as:

$$V_e(s) = \lim_{n \to 0} V(s, n) \tag{4c}$$

$$P_e(s) = \lim_{n \to 0} P(s, n) \tag{4d}$$

Note that the above quantities are generally different for $n \to 0^+$, the upper surface and $n \to 0^-$, the lower surface. When necessary to distinguish between the surfaces we will include a + or - as a superscript.

Comparisons of the boundary-layer solution for $\bar{n} \to \infty$ to the inviscid solution for $n \to 0$ leads to the following identification of the common parts:

$$u_{cp} = U_e(s) + O(\epsilon^2) \tag{5a}$$

$$v_{cp} = v(s, 0) - \frac{d \rho_e U_e}{\rho_e ds} n + \epsilon^2 v_\sigma(s) + O(\epsilon^3) \tag{5b}$$

$$p_{cp} = p(s, 0) - \kappa(s) \rho_e U_e^2 n + \epsilon^2 p_\sigma(s) + O(\epsilon^3) \tag{5c}$$

where

$$v_\sigma(s) = \pm \frac{d \rho_e U_e \delta^*}{\rho_e ds} \tag{6a}$$

$$p_\sigma(s) = \rho_e U_e^2 \kappa(s) (\delta^* + \theta) \tag{6b}$$

and where δ^* and θ are the usual boundary-layer displacement and momentum thicknesses. Note that δ^* is defined such that it is positive on both upper and lower surfaces. Matching conditions on the airfoil surface can be derived by substituting the above expressions for the common parts into Eq. (1). The requirement that the normal component of velocity, $\mathcal{U}$, vanish on the airfoil surface then leads to the usual matching condition on $V(s,n)$ for $n \to 0$:

$$V_e(s) = \epsilon^2 v_\sigma(s) + O(\epsilon^3) \tag{7}$$

Similarly, substitution of Eq. (5c) into Eq. (1c) leads to the following expression for the surface pressure distribution

$$\mathcal{P}_e(s) \equiv \mathcal{P}(s, o) = P_e(s) - \epsilon^2 p_\sigma(s) + O(\epsilon^3) \tag{8}$$

where $P_e(s)$ is the surface value of pressure as determined from the inviscid solution and the second term in Eq. (8) represents a correction for the pressure variation across the boundary layer.

The corresponding expressions in the wake are somewhat more complicated because of discontinuities of the common-part terms across the wake. If we impose the condition that the full solution for $\mathcal{U}, \mathcal{V}, \mathcal{P}$, etc. is continuous across the wake and take proper care for the discontinuities of the common-part terms we can arrive at the following jump conditions for the outer inviscid solution:

$$[\![V]\!] \equiv V(s, 0^+) - V(s, 0^-) = \epsilon^2 v_w(s) + O(\epsilon^3) \tag{9a}$$

$$[\![P]\!] \equiv P(s, 0^+) - P(s, 0^-) = -\epsilon^2 \rho_w U_w c_w \kappa(s) + O(\epsilon^3) \tag{9b}$$

Moreover, since

$$[\![U]\!] = -\frac{1}{\rho_w U_w} [\![P]\!] + O([\![P]\!]^2)$$

then

$$[\![U]\!] = U(s, 0^+) - U(s, 0^-) = \epsilon^2 c_w \kappa(s) + O(\epsilon^3) \tag{9c}$$

where

$$\epsilon^2 v_w(s) = v_\sigma^+(s) - v_\sigma^-(s) = \frac{d \rho_w U_w \delta_w^*}{\rho_w ds} \tag{9d}$$

$$\epsilon^2 c_w(s) = -U_w(\delta_w^* + \theta_w) \tag{9e}$$

and where, ρ_w and U_w are the surface values of the outer inviscid solution on the wake streamline, and δ_w^* and θ_w are the respective sums of the upper and lower displacement and momentum thicknesses. The composite solution for the pressure at the wake axis is continuous and is given by

$$\mathcal{P}_e(s) \equiv \mathcal{P}(s, o) = P_e^+(s) - p_\sigma^+(s) = P_e^-(s) - p_\sigma^-(s) \tag{10}$$

where the plus and minus superscripts refer to the upper and lower sides of the wake axis. (In deriving the above expressions we have used the fact that the jumps in ρ_e and U_e across the wake axis are $O(\varepsilon^2)$). Equations (9a) and (9b) are jump conditions to be imposed along the wake axis of the outer inviscid flow. It should be noted that Eqs. (9) imply that the streamline slopes of the outer inviscid flow are also discontinuous across the wake axis to $O(\varepsilon^2)$ and that this in turn implies that the wake axis cannot be chosen as a streamline of the outer inviscid solution (to this order). A convenient choice for the wake axis is the composite solution for the streamline passing through the trailing edge. An equivalent analysis of the matching conditions in the wake is included in the more general work of Viviand (Ref. 57). In the present study we use an irrotational approximation to justify the introduction of a velocity potential in the outer inviscid problem. The above matching condition on the streamwise velocity component implies the velocity potential, Φ, must also be discontinuous across the wake. The appropriate jump condition on Φ can be determined

from Eq. (9c), rewritten in the form

$$\frac{d\Gamma}{ds} = \epsilon^2 c_w \kappa(s) \tag{11a}$$

where the circulation strength, Γ, is equal to the jump in potential across the axis. That is,

$$\Gamma \equiv \Phi(s, 0^+) - \Phi(s, 0^-) \tag{11b}$$

If β is defined as the angle between the wake streamline (defined by the composite solution) and the airfoil chord then,

$$\kappa = \frac{d\beta}{ds} \tag{12}$$

The expression for Γ can then be written in differential form,

$$d\Gamma = \epsilon^2 c_w \, d\beta \tag{13}$$

relating changes in circulation to the turning angle of the wake. The interested reader is referred to Refs. 5, 8, 16, 17, and 39 for further discussion of this condition.

The complete set of matching conditions derived above are summarized in Fig. 2. Note that within this formulation the wake thickness is prescribed but the location is not. The location of the wake is determined as part of the outer inviscid solution and is free to assume an equilibrium position consistent with the prescribed pressure jump across the wake.

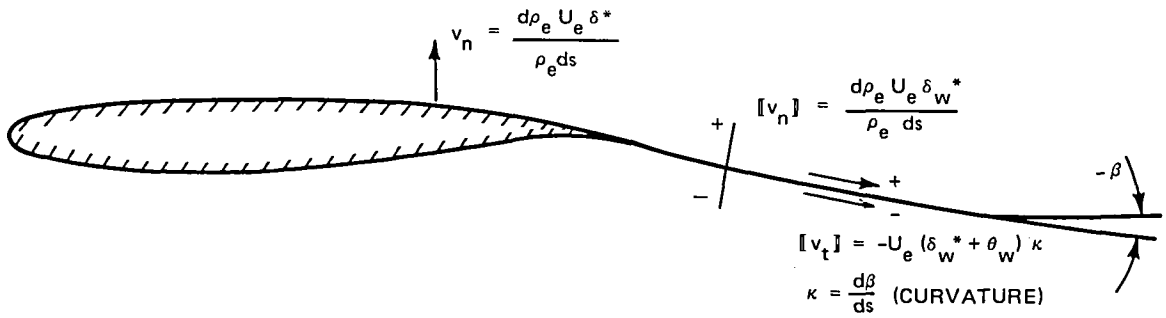

Figure 2 Viscous Matching Conditions

For cusped airfoils at lift, both the pressure gradient and streamline curvature generally become unbounded at the trailing edge with the following behavior:

$$\lim_{s \to s_{te}^-} \frac{dP_e}{ds} = \pm \frac{R_{te} U_{te}^2 c_\alpha}{2B} \, | s - s_{te} |^{-1/2} \tag{14a}$$

$$\lim_{s \to s_{te}^+} \kappa = \frac{c_\alpha}{2} \, | s - s_{te} |^{-1/2} \tag{14b}$$

where the subscripts (te) denote values at the trailing edge, R_{te} and U_{te} are the density and speed at the trailing edge, c_α is a constant that depends on the overall inviscid solution, B is the Prandtl-Glauert factor $\sqrt{1 - M_{te}^2}$, and the upper and lower signs in Eq. (14a) refer to the two sides of the airfoil. From the momentum integral equation and the definition of the surface-source velocity v_σ in Eq. (6a), we can show that Eq. (14a) implies a corresponding singularity in v_σ, as follows

$$\lim_{s \to s_{te}^-} v_\sigma = \pm \frac{U_{te} c_\alpha \delta_\pm^*}{2} \left(\frac{h_{te} + 1}{h_{te}} \right) | s - s_{te} |^{-1/2} \tag{14c}$$

where $\delta_\pm^*$ is the boundary-layer displacement thickness of either the upper or lower surface boundary layers at the trailing edge. In deriving this result we assumed the total temperature is constant across the boundary layer and have used the large Reynolds number limit for the shape factor, h. That is,

$$h = h_{te} = 1 + (\gamma - 1) M_{te}^2 \text{ for } R_e \to \infty$$

Similarly, from Eqs. (9b), (9e) and (14b) we obtain:

$$\lim_{s \to s_{te}^+} [\![P]\!] = \frac{\rho_{te} U_{te}^2 c_\alpha (\delta_w^* + \theta_w)}{2} \, | s - s_{te} |^{-1/2} \tag{14d}$$

Detailed analysis indicates that these singularities lead to a breakdown of conventional boundary-layer theory at trailing edges and to a growth in the magnitude of viscous effects induced by both the displacement thickness and wake curvature terms from $O(\varepsilon^2)$ to $O(\varepsilon^{3/2})$ near trailing edges. A separate "inner" solution is required to resolve the nonuniformity at the trailing edge as described in the next subsection.

2.3 TRAILING-EDGE REGION

In this section we present the results of an analysis of the strong-interaction region that develops in turbulent flows near trailing edges. An analysis for the incompressible case was first presented in Ref. 4 and later extended to compressible flow in Ref. 5. The analysis is based on a formal application of the method of matched asymptotic expansions (Ref. 58) to the full Reynolds equations of turbulent

flow for Reynolds number Re $\rightarrow \infty$. The theory was developed under the following assumptions:

- the trailing edge of the airfoil is cusped
- the flow is locally subsonic in the trailing-edge region
- total temperature is constant in the trailing-edge region
- the boundary layer upstream of the trailing-edge region is a fully-developed turbulent flow
- the boundary layer approaching the trailing-edge region is not separated

In the present context, the assumption of a fully-developed turbulent flow is taken to mean that the velocity profile in the outer part of the boundary layer can be adequately represented by a Coles' law-of-the-wall/law-of-the-wake, with a small velocity defect. That is, we assume the velocity profile in the outer part of the boundary layer, upstream of the trailing edge can be represented in the form

$$u = U_e(s)[1 + \epsilon f(s, \bar{n}) + \cdots] \tag{15a}$$

with

$$\epsilon f = \frac{u^*(s)}{k U_e(s)} \left[\ln\left(\frac{\epsilon \bar{n}}{\delta(s)}\right) - \tilde{\pi} W\left(\frac{\epsilon \bar{n}}{\delta(s)}\right) \right] \tag{15b}$$

and

$$u^* = \sqrt{\tau_w / \rho_e} \tag{15c}$$

where τ_w, u^*, and δ are the local skin friction, friction velocity and boundary-layer thickness, k is the von Karman constant, $\tilde{\pi}$ is Coles' wake parameter, and W is the wake function which, in the present work, is assumed to be expressible as a simple third-order polynomial. It is also assumed that the profile function, $f(s, \bar{n})$ approaches a definite limit, $f_{te}(\bar{n})$ at the trailing edge, $s = s_{te}$. The above assumptions permit a relatively complete solution to be obtained for the local flow near the trailing edge. In this region the solution develops the multi-layer structure shown schematically in Fig. 3. The upstream flow is divided into conventional inviscid and boundary layer regions over a streamwise length of 0(1). The turbulent boundary layer has a two-layer structure consisting of an outer, wake region and an inner, equilibrium wall layer. The velocity profile in the outer region is described by Eq. (15).

The velocity profile in the inner layer is expressed in a law-of-the-wall form, which for incompressible flow is written as

$$u = \epsilon U_e(s) F\left(s, \frac{n}{\epsilon \hat{\epsilon}}\right) \tag{16}$$

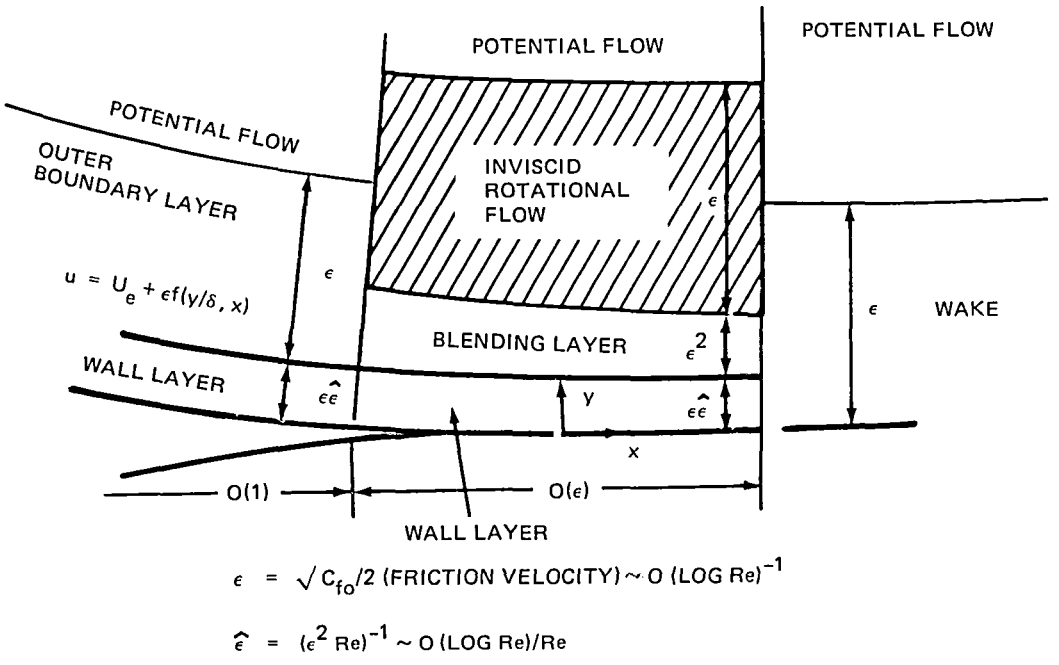

Figure 3 Flow Field Structure Near the Trailing Edge

where $\hat{\epsilon}$ is the ratio of wall-layer to boundary-layer thickness and is given by

$$\hat{\epsilon} = (\epsilon^2 R_e)^{-1} \tag{17}$$

It follows that the wall layer is exponentially thin compared to the boundary layer thickness.

The formal justification of the two-layer structure in terms of an asymptotic limit solution for Re $\to \infty$ was carried out by Mellow (Ref. 25), Bush and Fendall (Ref. 26), and Yajnik (Ref. 27) for incompressible flow. These studies showed that the velocity profile functions satisfied simplified boundary layer equations with linearized convective-terms. The usual non-linear boundary layer equations can be viewed as composite equations valid in both inner and outer regions and containing additional higher order terms.

An extension to compressible flow was attempted by Afzal (Ref. 28) but the analysis was in error, with the result that his assumed inner and outer expansions did not match. The reasons for the error and the modifications necessary to obtain a valid compressible solution are discussed in Ref. 47. It was shown there that the small defect form given in Eq. (15) carries over to the compressible case, but that the inner expansion required modification to incorporate a preliminary van Driest compressibility transformation. One of the more firm rational results in turbulence theory concerns the logarithmic behavior of the velocity profiles in the overlap

region between the inner and outer regions, i.e., $n/\epsilon \ll 1$ and $n/\epsilon\hat{\epsilon} \gg 1$ leading to the form of the velocity profile given in Eq. (15).

The present work can be viewed as an extension of the asymptotic theory of non-interacting boundary layers to the strong interaction problem. The boundary layer in the interaction region develops a compact, multi-layer structure as sketched in Fig. 3. Three layers are required:

1. An outer layer that is inviscid and rotational. The vorticity arises from the nonuniform flow in the upstream boundary layer. In a fully-developed turbulent flow the total vorticity is small and the solution in this region can be described as a perturbation of the external potential flow induced by the small vorticity. To lowest order, it can be assumed that the vorticity is convected along the nearly parallel streamlines of the potential flow. In the terminology of secondary-flow analysis, the flow in this region is classified as a small shear, small-disturbance flow (Ref. 59).

2. An inner layer next to the wall. In this region the flow is described as equilibrium wall layer that is a continuation of the wall layer from the upstream flow. The total stress, laminar plus Reynolds stress, is constant across the layer. The thickness of the layer is exponentially small compared to the outer layer.

3. A blending layer situated between the outer and wall layers. It is necessary in order to match the Reynolds stresses in the outer and wall layers. The layer is thinner than the overall boundary layer but thicker than the wall layer.

Turbulent closure approximations are required to lowest order, only in the two inner layers. The inner layers are thin and do not affect the determination of the solution in the outer inviscid region. The outer region is most important since it alone determines the pressure distribution

Outer Expansion and Governing Equations. The solution in the outer region is developed as a perturbation to the basic external inviscid flow in the following form:

$$\tilde{u} = U(x, y; \epsilon) + \epsilon\, U_{te} f(y) + \epsilon^{3/2} \tilde{u}^{(1)}(x, y) + \cdots \tag{18}$$

$$\tilde{v} = V(x, y; \epsilon) + \epsilon^{3/2} \tilde{v}^{(1)}(x, y) + \cdots \tag{19}$$

$$\tilde{p} = P(x, y; \epsilon) + \epsilon^{3/2} \tilde{p}^{(1)}(x, y) + \cdots \tag{20}$$

where (x,y) form a local Cartesian coordinate system with an origin at the trailing edge and scaled as follows

$$x = \frac{s - s_{te}}{\epsilon B}, \quad y = n/\epsilon \tag{21}$$

with the Prandtl-Glauert factor B defined as

$$B = \sqrt{1 - M_{te}^2} \tag{22}$$

The leading terms of Eqs. (18) - (20) are meant to include all terms that result from expanding the known inviscid solution in powers of (s,n), transforming to (x,y) and expressing the result as an expansion in ε. For a cusped airfoil this leads to the expansion

$$U = U_{te}[1 + \epsilon^{1/2} U_1(x, y)/B + \cdots] \tag{23a}$$

$$V = U_{te}[\epsilon^{1/2} V_1(x, y) + \cdots] \tag{23b}$$

where U_1, V_1 are known algebraic functions and U_{te} is the trailing-edge value of the inviscid velocity. The second term in Eq. (18), f(y), arises from the nonuniform flow in the upstream boundary layer and is a known function of the form given in Eq. (15).

Notice that the expansion for u is similar to the law-of-the-wake in the upstream boundary layer, except that now the full y-dependence of the inviscid flow is accounted for in the leading term, U(x,y;ε). The equations governing the perturbation terms $\tilde{u}^{(1)}$, $\tilde{v}^{(1)}$, $\tilde{p}^{(1)}$ are arrived at by substituting the above expansion into the full Reynolds equations of turbulent flow. The series solution must be augmented with similar expansions for the density and temperature. For convenience we assume the total temperature in the upstream boundary layer is constant across the boundary layer. The density can then be computed from the equation of state and the total temperature. This is known to be a highly satisfactory approximation in the speed range of interest.

The above analysis leads to a set of partial differential equations governing the disturbance to a weakly sheared, compressible, inviscid flow. The disturbance equations can be reduced to incompressible form by a generalization of the Prandtl-Glauert transformation of subsonic potential flow. After transforming to the scaled coordinates x,y by Eq. (21) we transform the dependent variables $\tilde{u}^{(1)}$, $\tilde{v}^{(1)}$, $\tilde{p}^{(1)}$ by

$$\tilde{u}^{(1)} = U_{te} B^{-1/2} \left[a_2 \bar{u} + (a_0 - \gamma M_{te}^2) \frac{df}{dy} \Psi_1 - a_0 f U_1 + a_1 \chi \frac{\partial V_1}{\partial x} \right] \tag{24a}$$

$$\tilde{v}^{(1)} = U_{te} B^{1/2} \left[a_2 \bar{v} + (1 - a_2) f V_1 - a_1 \chi \frac{\partial U_1}{\partial x} \right] \tag{24b}$$

$$\tilde{p}^{(1)} = \rho_{te} U_{te}^2 B^{-1/2} \left[a_2 \bar{p} - a_1 \chi \frac{\partial V_1}{\partial x} \right] \tag{24c}$$

where U_1, V_1 and Ψ_1 are normalized velocities and streamfunction determined from the inviscid expansion given in Eqs. (23). For cusped airfoils we have

$$U_1 - iV_1 = -i\, c_\alpha (x + iy)^{1/2} \tag{24d}$$

or in real form,

$$U_1 = c_\alpha r^{1/2} \sin \frac{\Omega}{2}, \quad V_1 = c_\alpha r^{1/2} \cos \frac{\Omega}{2}$$

$$\Psi_1 = -\frac{2}{3} c_\alpha r^{3/2} \cos \frac{3\Omega}{2} \tag{24e}$$

where c_α is a known constant and (r,Ω) are polar coordinates with $r^2 = x^2 + y^2$ and $\tan \Omega = y/x$. The function χ is the streamfunction corresponding to $f(y)$,

$$\chi = \int_0^y f(y)\, dy \tag{25}$$

The parameters a_0, a_1, a_2 and C_0 are Mach number dependent constants defined by

$$a_0 = \tfrac{1}{2}(C_0 - 1) - \frac{M_{te}^2}{4B^2}(C_0 + 1) \tag{26a}$$

$$a_1 = -\frac{M_{te}^2}{2B^2}(C_0 + 1) \tag{26b}$$

$$a_2 = \tfrac{1}{4}(1 + B^{-2})(C_0 + 1) \tag{26c}$$

$$C_0 = 1 + (\gamma - 1) M_{te}^2 \tag{26d}$$

With these transformations the basic equations governing the disturbances in the outer region reduce to the following linearized, incompressible equations of mass and vorticity

$$\frac{\partial \bar{u}}{\partial x} + \frac{\partial \bar{v}}{\partial y} = 0 \tag{27}$$

$$\frac{\partial \bar{u}}{\partial y} - \frac{\partial \bar{v}}{\partial x} = \Psi_1(x, y) \frac{d^2 f(y)}{dy^2} \tag{28}$$

The transformed static pressure is determined from the linearized Bernoulli equation

$$\bar{p} = -\bar{u} - fU_1 + \frac{df}{dy}\,\Psi_1 \tag{29}$$

If the disturbance streamfunction, $\bar{\psi}$, is introduced, Eq. (28) becomes

$$\nabla^2 \bar{\psi} = -\bar{\zeta} = \Psi_1(x, y)\,\frac{d^2 f}{dy^2} \tag{30}$$

where $\bar{u} = \partial\psi/\partial y$, $\bar{v} = -\partial\psi/\partial x$. This is the same basic equation derived in Ref. 4 for the incompressible trailing edge problem. Equation (30) is a simple Poisson equation relating the disturbance streamfunction, $\bar{\psi}$, to the perturbation vorticity, $\bar{\zeta}$. The vorticity perturbation arises from generation in the upstream boundary layer and convection along the curved streamlines of the external potential flow, as sketched in Fig. 4. The vorticity is known in terms of the upstream boundary layer velocity profile and the inviscid streamfunction. The Poisson equation must be solved subject to the boundary condition that the normal component of velocity vanish on the airfoil surface, which, to the same order of approximation, is represented by a slit along the negative x axis. Thus,

$$\bar{v}(x, 0) = 0 \text{ for } x < 0 \tag{31}$$

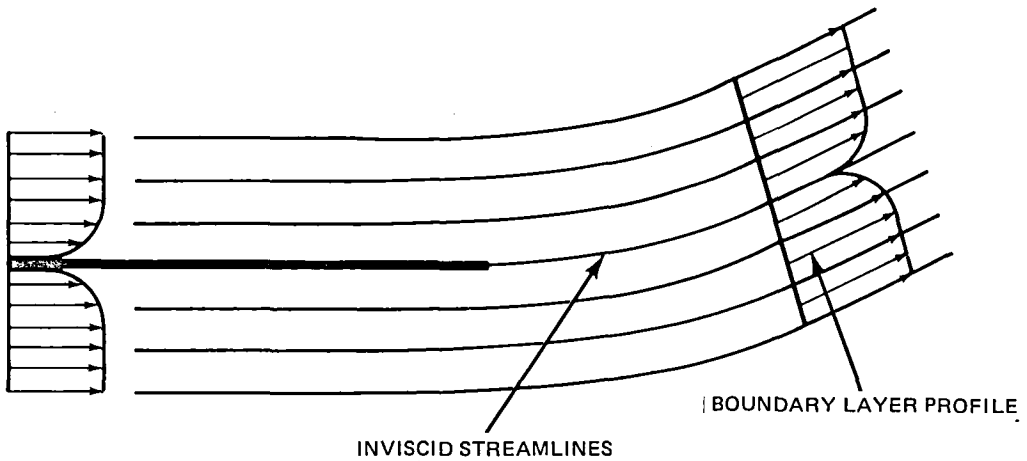

$$\bar{\zeta}(\Psi) = \zeta_0\,(Y + \epsilon^{1/2}\Psi_1 + \cdots) + \cdots$$

$$= \zeta_0\,(Y) + \epsilon^{1/2}\zeta_0\,(Y)\Psi_1 + \cdots$$

$$= -\epsilon\, f'(Y) - \epsilon^{3/2} f''(Y)\,\Psi_1 + \cdots$$

INITIAL PROFILE — INTERACTION

Figure 4 Vorticity Distribution in the Trailing Edge Region

In addition, we must impose the condition that the pressure and flow deflection be continuous across interfaces at the boundary layer edges and wake centerline. We must also assure that the disturbances decay in the far field rapidly enough to allow matching to the outer inviscid potential solution.

It is convenient to introduce the pressure and a variable $\bar{\omega}$, related to the disturbance flow angle, as dependent variables. Thus, we transform from $(\bar{u}, \bar{v})$ to $(\bar{p}, \bar{\omega})$ defined by

$$\bar{v} = \bar{\omega} + fV_1 \tag{32a}$$

$$\bar{u} = -\left[\bar{p} + fU_1 - \frac{df}{dy}\Psi_1\right] \tag{32b}$$

and arrive at the symmetric pair of differential equations

$$\frac{\partial \bar{p}}{\partial x} - \frac{\partial \bar{\omega}}{\partial y} = -2f\frac{\partial U_1}{\partial x} \tag{33a}$$

$$\frac{\partial \bar{p}}{\partial y} + \frac{\partial \bar{\omega}}{\partial x} = -2f\frac{\partial V_1}{\partial x} \tag{33b}$$

The function f(y) contains contributions from boundary layers on the upper and lower surfaces of the airfoil. Since the equations are linear the two layers can be treated separately and the results superposed to obtain a complete solution.

Scale Transformation. - The solution to the outer problem can be reduced to the determination of universal functions through the introduction of the following scale transformations appropriate to either the upper or lower surface boundary layer. First, change coordinates according to

$$\eta = y/\delta \quad \xi = x/\delta \quad \nu = r/\delta \tag{34}$$

where δ is the thickness of the boundary layer at the trailing edge. Then the boundary-layer profile functions f and χ are expressed in the law-of-the-wake form as

$$f = \gamma^* [h_1'(\eta) + \tilde{\pi}\, h_2'(\eta)] \quad 0 < \eta < 1 \tag{35a}$$

$$\chi = \gamma^* \delta [h_1(\eta) + \tilde{\pi}\, h_2(\eta)] \quad 0 < \eta < 1 \tag{35b}$$

$$h_1 = \eta \log \eta - \eta, \quad h_2 = -\int_0^\eta W(\eta)\, d\eta \tag{35c}$$

and are zero outside the strip $0 \le \eta \le 1$ (primes denote $\partial/\partial\eta$). $\tilde{\pi}$ is Coles' wake parameter, defined by the initial boundary-layer profile, and γ^* is a friction parameter defined by

$$\gamma^* = \frac{\sqrt{\tau_w/\rho_{te}^2 U_{te}^2}}{k} \tag{36}$$

and τ_w is the skin friction of the upper surface boundary layer at the trailing edge. The following additional scalings are employed

$$U_1 = c_\alpha \delta^{1/2} \hat{U}(\xi, \eta), \quad V_1 = c_\alpha \delta^{1/2} \hat{V}(\xi, \eta) \tag{37a}$$

where

$$\hat{U} = \nu^{1/2} \sin\frac{\Omega}{2}, \quad \hat{V} = \nu^{1/2} \cos\frac{\Omega}{2} \tag{37b}$$

$$\nu^2 = \xi^2 + \eta^2, \quad \Omega = \tan^{-1}(\eta/\xi) \tag{37c}$$

and

$$\bar{p} = c_\alpha \gamma^* \delta^{1/2} [\hat{p}_1(\xi, \eta) + \bar{\pi}\, \hat{p}_2(\xi, \eta)] \tag{38a}$$

$$\bar{\omega} = c_\alpha \gamma^* \delta^{1/2} [\hat{\omega}_1(\xi, \eta) + \bar{\pi}\, \hat{\omega}_2(\xi, \eta)] \tag{38b}$$

The functions $\hat{p}_{1,2}$ and $\hat{\omega}_{1,2}$ are universal functions of (ξ, η) that are independent of all parameters appearing in the problem; although $\hat{p}_2$ and $\hat{\omega}_2$ depend on the functional form used to represent the wake function $W(\eta)$.

The $\hat{p}$ and $\hat{\omega}$ functions satisfy the following inhomogeneous Cauchy-Riemann equations,

$$\frac{\partial \hat{p}_{1,2}}{\partial \xi} - \frac{\partial \hat{\omega}_{1,2}}{\partial \eta} = -2h'_{1,2}(\eta) \frac{\partial \hat{U}(\xi, \eta)}{\partial \xi} \tag{39a}$$

$$\frac{\partial \hat{p}_{1,2}}{\partial \eta} + \frac{\partial \hat{\omega}_{1,2}}{\partial \xi} = -2h'_{1,2}(\eta) \frac{\partial \hat{V}(\xi, \eta)}{\partial \xi} \tag{39b}$$

with

$$\hat{\omega}_{1,2}(\xi, 0) = 0 \text{ for } \xi < 0 \tag{39c}$$

Particular Solution. - A particular solution to the inhomogeneous Cauchy-Riemann equations can be found by standard complex variable analysis. Following Ref. 60 we introduce the complex representation

$$z = \xi + i\eta \tag{40a}$$

$$\hat{U} - i\hat{V} = -iz^{1/2} \tag{40b}$$

$$\lambda_{1,2} = \hat{p}_{1,2} + i\hat{\omega}_{1,2} \tag{40c}$$

With (z,η) considered as independent complex variables, Eq. (30) can be written as the single complex equation

$$\frac{\partial \lambda_{1,2}}{\partial \eta} = - \frac{h'_{1,2}(\eta)}{\sqrt{z - 2i\eta}} \tag{41}$$

where the derivative with respect to η is applied holding z constant. The solution to Eq. (41) can be expressed as the sum,

$$\lambda_{1,2} = \lambda_{p_{1,2}}(z, \eta) + \lambda_{H1,2}(z) \tag{42}$$

where the first term is any particular solution satisfying Eq. (41) and the second is an arbitrary analytic function that is determined from boundary and interface conditions. The interface conditions now simply require continuity of $\lambda_{1,2}$ across interfaces. A particular integral is easily found by quadrature

$$\lambda_{p1,2} \equiv F_{1,2}(z, \eta) = \begin{cases} 0 & \eta > 1 \\ -\int_1^{\eta} \frac{h'_{1,2}(\eta)}{\sqrt{z - 2i\eta}} \, d\eta & 0 < \eta \leq 1 \\ 0 & \eta < 0 \end{cases} \tag{43}$$

The above solution is continuous across the interface, $\eta = 1$, but has jump discontinuities across the real axis, $\eta = 0$.

The component corresponding to the logarithmic term in the velocity profile is found by direct integration. The quadrature for the second component can be carried out for polynomial approximations to the wake function $W(\eta)$. We employ the representation

$$W(\eta) = 1 - \frac{C_1 t}{8}\left[\left(1 - \frac{t^2}{3}\right) + \frac{C_2}{2}\left(1 - \frac{t^4}{5}\right)\right] \quad , \; t \equiv 2\eta - 1. \tag{44}$$

With $C_1 = 15.369157$ and $C_2 = -0.36536$. Eq. (44) is an accurate (to four places), rational approximation to Cole's wake function, $1 + \cos \pi\eta$. Thus, Eq. (44) should provide an acceptable fit to most turbulent velocity profiles. These procedures lead to explicit algebraic expressions for the particular solution $\lambda_{p1,2}(z,\eta)$. They are somewhat lengthy and, hence, will not be written-out here. For the purposes of the present study we require only the limiting values on the real axis, $\eta \to 0^+$, leading to the jump discontinuity referred to above. We introduce the real functions $\beta_{1,2}(\xi)$ and $\sigma_{1,2}(\xi)$ defined as the real and imaginary values of $\lambda_{p1,2}$ as the real axis is approached from above. That is,

$$\beta_{1,2}(\xi) + i\sigma_{1,2}(\xi) = \lim_{\eta \to 0_+} \lambda_{p_{1,2}}(z, \eta)$$

These functions can be conveniently computed from the limiting values of analytic functions $g_{1,2}(z)$ determined from $\lambda_{p1,2}$. Thus,

$$\beta_{1,2} + i\sigma_{1,2} = \lim_{\eta \to 0_-} g_{1,2}(z) \tag{45}$$

where

$$g_1(z) = 2i\left\{\sqrt{z} - \sqrt{z-2i} + \sqrt{z}\log\left(\frac{\sqrt{z}+\sqrt{z-2i}}{2\sqrt{z}}\right)\right\} \tag{46}$$

$$g_2(z) = -\frac{C_1}{3}\left\{1 - \frac{8C_2}{33}(z-i)^2\right\}\left\{\tfrac{1}{5}[z-i]\,[z^{5/2} - (z-2i)^{5/2}] - \tfrac{1}{7}\,[z^{7/2} - (z-2i)^{7/2}]\right\}$$
$$-\frac{C_1C_2}{33}\left\{\tfrac{2}{3}[z-i]\,[z^{5/2} - (z-2i)^{5/2}] - i[z^{5/2} + (z-2i)^{5/2}]\right\} + 2iz^{1/2} \tag{47}$$

The only singularities in the strip are branch points at infinity and the origin. The appropriate branch of the multivalued functions are defined by a cut along the negative real axis and the limit $\eta \to 0_-$. The functions $\sigma_{1,2}(\xi)$ and $\beta_{1,2}(\xi)$ can be shown to possess the following symmetry

$$\sigma_{1,2}(\xi) = \beta_{1,2}(-\xi) \tag{48}$$

Thus, only values on the negative (or positive) real axis need be computed. The functions are plotted in Figs. 5 and 6. For $\xi \to -\infty$ they possess the following asymptotic behavior

$$\sigma_{1,2} \to -|\xi|^{-1/2} \tag{49a}$$

$$\beta_1 \to -\frac{1}{4}|\xi|^{-3/2},\quad \beta_2 \to -\frac{C_1}{40}|\xi|^{-3/2} \tag{49b}$$

The behavior for $\xi \to 0^-$ is given by

$$\sigma_1 \to -2 + \frac{\pi}{2}\sqrt{-\xi} + 0(\xi) \tag{49c}$$

$$\sigma_2 \to -1.3740 + 0(\xi) \tag{49d}$$

$$\beta_1 \to -2 - \sqrt{-\xi}\ln|2\xi| + 2\sqrt{-\xi} + 0(\xi) \tag{49e}$$

$$\beta_2 \to -1.3740 + 2\sqrt{-\xi} + 0(\xi) \tag{49f}$$

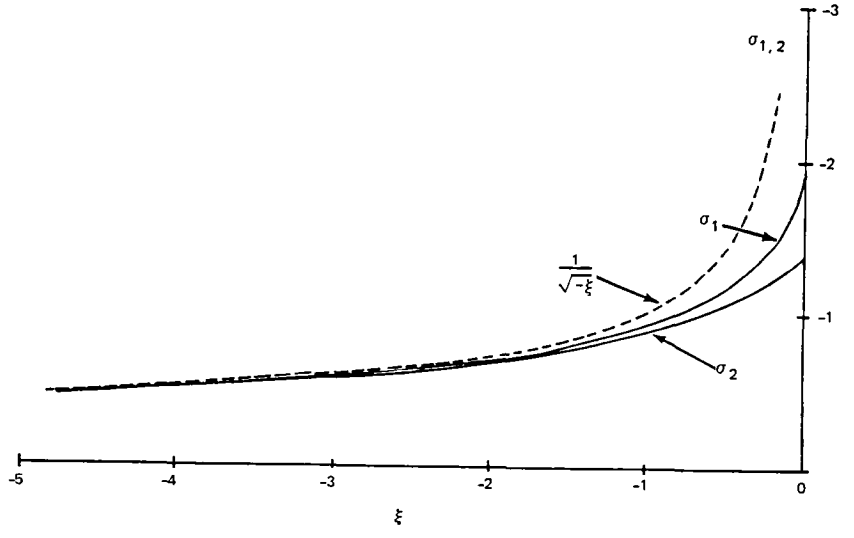

Figure 5 Particular Solutions for the Downwash Functions σ_1, σ_2

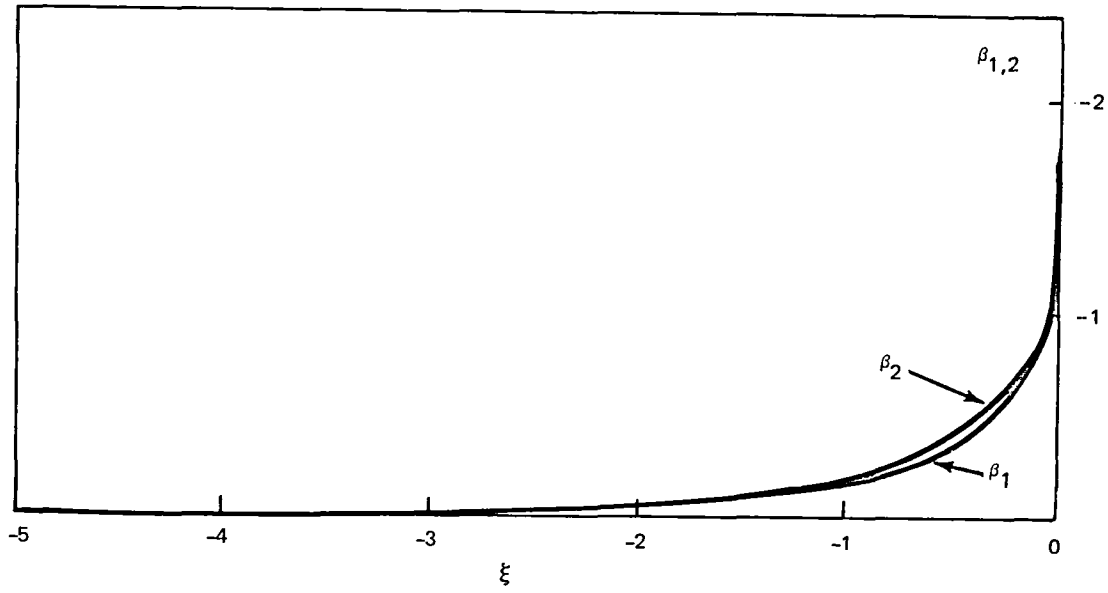

Figure 6 Particular Solutions for the Loading Functions β_1, β_2

The particular integral specified above is not unique and to it we can add arbitrary analytic functions of z to obtain other solutions. From the above expressions we can determine the contributions of the particular solution to the normal component of velocity on the airfoil and to the jump in pressure across the wake. These quantities have a direct correspondence to the source velocity and pressure jump appearing in the matching conditions of the external flow discussed in Section 2.2. It is convenient to arrange the particular solution so that these quantities match the limiting behavior of the external solution for $x \to 0$, $\varepsilon \to 0$ as given in Eqs. (7 and 9). This can be accomplished by adding the following piecewise analytic function to the particular solution $F_{1,2}(z, \eta)$,

$$\Delta F_{1,2}(z) = \frac{a_3}{(z+i)^{1/2}} \quad \eta > 0 \tag{50}$$

where a_3 is a constant. The function $\Delta F_{1,2}(z)$ is analytic in the upper half plane and is defined to be zero in the lower half plane. Hence, it contributes to the discontinuity of the particular solution across the real axis. The contribution to the jump across $\eta = 0$ is given by

$$\Delta\beta_{1,2} + i\Delta\sigma_{1,2} = \frac{a_3}{(\xi+i)^{1/2}} \to \frac{a_3}{\xi^{1/2}} \quad \text{for } |\xi| \to \infty \tag{51}$$

The full discontinuity of the particular solution across the real axis is therefore equal to

$$\bar{\beta}_{1,2}(\xi) + i\bar{\sigma}_{1,2}(\xi) = \beta_{1,2} + i\sigma_{1,2} + \frac{a_3}{(\xi + i)^{1/2}} \tag{52}$$

The contributions of the above solution to the normal component of velocity on the airfoil and to the pressure jump in the wake are given by

$$\epsilon^{3/2}\tilde{v}_p = \frac{\epsilon^{3/2}A}{(1+\bar{\pi})}\left[\bar{\sigma}_1\left(\frac{s - s_{te}}{\epsilon\delta B}\right) + \bar{\pi}\bar{\sigma}_2\left(\frac{s - s_{te}}{\epsilon\delta B}\right)\right] \tag{53a}$$

$$\epsilon^{3/2}\tilde{p}_p = \pm\frac{\epsilon^{3/2}A}{(1+\bar{\pi})}\left[\bar{\beta}_1\left(\frac{s - s_{te}}{\epsilon\delta B}\right) + \bar{\pi}\bar{\beta}_2\left(\frac{s - s_{te}}{\epsilon\delta B}\right)\right] \tag{53b}$$

where

$$\epsilon^{3/2}A = c_\alpha U_{te} B^{1/2} a_2 \gamma^* \delta^{1/2}(1+\bar{\pi}) \tag{53c}$$

and where $\tilde{v}_p$ and $\tilde{p}_p$ are contributions of the particular integral to the inner solution Eqs. (24). The above expressions correspond to both upper and lower surfaces with the appropriate values of δ, γ^*, and $\bar{\pi}$. The plus and minus signs in Eq. (53b) refer to the upper and lower surfaces, respectively.

To demonstrate matching to the external solution, we expand the above expressions for $|\xi| \to \infty$ using Eqs. (49) and (51) to obtain

$$\lim_{\xi \to -\infty} \epsilon^{3/2}\tilde{v}_p = -\frac{\epsilon^{3/2}A(1+a_3)}{(-\xi)^{3/2}} = -\frac{\epsilon^2 A(1+a_3)B^{1/2}\delta^{1/2}}{(s_{te} - s)^{1/2}} \tag{54a}$$

$$\lim_{\xi \to +\infty} \epsilon^{3/2}\tilde{p}_p = -\frac{\epsilon^{3/2}A(1-a_3)}{(\xi)^{1/2}} = -\frac{\epsilon^2 A(1-a_3)B^{1/2}\delta^{1/2}}{(s - s_{te})^{1/2}} \tag{54b}$$

For constant total temperature and large Reynolds number the displacement thickness is given by

$$\delta^* \to C_0(1+\bar{\pi})(\gamma^*\delta) \text{ for } R_e \to \infty \tag{55}$$

From the above relations and the definition of a_2 in Eq. (26c) we can show that Eqs. (54) reduce to the singular expressions given in Eqs. (14c, d) provided the constant a_3 is given the value

$$a_3 = \frac{M_{te}^2}{2 - M_{te}^2} \tag{56}$$

Note that is is the negative of the particular integral that corresponds to the surface source velocity in Eq. (7). These results establish the close

correspondences between the matching conditions of the external solution and the discontinuities of the particular solution on the real axis. The determination of the particular integral is the most important result of this section.

The particular integral provides the contributions generated by the inhomogeneous forcing term of the differential equations. It is not a complete solution to the problem because it is discontinuous across the wake axis and it has a nonzero imaginary part on the negative real axis and, therefore, violates the boundary conditions given by Eq. (39c).

The complete solution in the trailing-edge region can be obtained by adding a complementary solution to the particular integral determined above. The complementary solution can be represented by an arbitrary analytic function of the complex variable, z, which can be adjusted to satisfy the boundary conditions. The analytic function is determined from conditions that $\bar{v} = \bar{v}_p + \bar{v}_H$ is zero on the airfoil and the solution is continuous across the wake axis.

The solutions just described account for contributions generated by the upper surface boundary layers. Similar contribution from the lower surface boundary layers must be added to complete the solution. Since knowledge of the complementary solutions are not needed in the present study, we will not discuss them further.

In the following section we show how the particular solution, by itself, can be employed to correct the external viscid/inviscid solution for trailing-edge interaction effects. A procedure for removing the singularities of second-order boundary-layer theory and accounting for normal pressure-gradient effects will also be described.

2.4 COMPOSITE SOLUTION

In this section we describe a procedure for using the inner trailing-edge solution to correct the conventional boundary-layer formulation described in Sec. 2.2. The composite solution given in Sec. 2.2 is uniformly valid in the inviscid, boundary-layer and wake regions but is not valid in the strong-interaction region at

trailing edges. A solution, uniformly valid in the trailing edge region, can be constructed by adding terms corresponding to the trailing-edge solution minus its common part to the "outer" composite solution given in Eqs. (1). This extends the domain of validity of the "outer" composite solution to include the trailing-edge region. Thus, a composite solution that is uniformly valid in the trailing edge region can be written in the following form

$$\mathcal{U} = U(s,n;\ v_\sigma;\ [\![V]\!];\ \Gamma) + [u(s,\bar{n}) - u_{cp}(s,\bar{n})] + [\tilde{u}(\xi,\eta) - \tilde{u}_{cp}(\xi,\eta)] \tag{57a}$$

$$\mathcal{V} = V(s,n;\ v_\sigma;\ [\![V]\!];\ \Gamma) + [v(s,\bar{n}) - v_{cp}(s,\bar{n})] + [\tilde{v}(\xi,\eta) - \tilde{v}_{cp}(\xi,\eta)] \tag{57b}$$

$$\mathcal{P} = P(s,n;\ v_\sigma;\ [\![V]\!];\ \Gamma) + [p(s,\bar{n}) - p_{cp}(s,\bar{n})] + [\tilde{p}(\xi,\eta) - \tilde{p}_{cp}(\xi,\eta)] \tag{57c}$$

where $\tilde{u}$, $\tilde{u}_{cp}$, etc. are the contributions from the trailing-edge solution and its associated common part. Similar representations are also assumed for the density and temperature. As discussed in the previous section, the complete trailing-edge solution is the sum of a particular integral and a homogeneous solution. The homogeneous solution is a solution of the inviscid irrotational-flow equations that is added to the particular integral in order to satisfy boundary conditions in the trailing-edge region. The necessity of utilizing homogeneous solutions can be avoided if we include only the contributions from the particular integral in the expressions for the trailing-edge solution appearing in the last bracket of Eqs. (57). With this choice, the matching conditions and the functions v_σ, $[\![v]\!]$ and Γ which determine the outer inviscid solution, are modified such that the homogeneous solution is automatically included in the inviscid outer solution given by the first term in Eqs. (57). Thus the trailing-edge terms in Eq. (57) are given by

$$\tilde{v} - \tilde{v}_{cp} = \epsilon^{3/2}\tilde{v}_p \tag{58a}$$

$$\tilde{p} - \tilde{p}_{cp} = \epsilon^{3/2}\tilde{p}_p \tag{58b}$$

$$\tilde{u} - \tilde{u}_{cp} = \epsilon^{3/2}\tilde{u}_p \tag{58c}$$

where $\tilde{v}_p$ and $\tilde{p}_p$ are determined from the contributions to the particular integral as given in Eqs. (53). The term $\tilde{u}_p$ is obtained from $\tilde{p}_p$ through the definitions in Eqs. (24a), (32b) and (38a).

The modified matching conditions can be derived from Eqs. (57) by imposing the condition that the normal velocity components $\mathcal{U}$ and v vanish on the airfoil surface

(n = n = 0) and the condition that both the full solution ($\mathcal{U}, \mathcal{V}, \mathcal{P}$) and the boundary-layer solution (u,v,p) be continuous in the wake. Specializing Eqs. (57a, b) to the airfoil surface and wake axis leads to the following expression for the composite solution of the normal velocity and pressure on the airfoil surface and wake axis:

$$\mathcal{V}_e(s) = V_e(s) + \epsilon^{3/2}\left[\tilde{v}_p(\xi) + \frac{A(1+a_3)}{(-\xi)^{1/2}}\, H(-\xi)\right] - \epsilon^2 v_\sigma(s) \tag{59a}$$

$$\mathcal{P}_e(s) = P_e(s) + \epsilon^{3/2}\left[\tilde{p}_p(\xi) + \frac{A(1-a_3)}{(\xi)^{1/2}}\, H(\xi)\right] - \epsilon^2 p_\sigma(s) \tag{59b}$$

where $H(\xi)$ is the unit step function, and

$$v_\sigma = \pm \frac{d\rho_e U_e \delta^*}{\rho_e ds} \tag{60a}$$

$$p_\sigma = \pm \rho_e U_e^2 (\delta^* + \theta)\, \kappa(s) \tag{60b}$$

The plus (minus) sign is for the upper (lower) side of the airfoil and the constants A and a_3 are given by Eqs. (53c) and (56).

The condition that the V vanish on the airfoil surface leads to the following expression for the corrected source velocity on the airfoil:

$$V_e(s) = -\epsilon^{3/2}\left[\tilde{v}_p(\xi) + \frac{A(1+a_3)}{(-\xi)^{1/2}}\right] + \epsilon^2 v_\sigma \tag{61}$$

The requirement that the composite normal velocity and pressure, as determined from Eqs. (59), be continuous across the wake axis leads to the following relationships for the jumps in source velocity $[\![V]\!]$ and pressure $[\![P]\!]$ across the wake axis:

$$[\![V]\!] \equiv V_e^+(s) - V_e^-(s) = -\epsilon^{3/2}[\tilde{v}_p^+(\xi^+) - \tilde{v}_p^-(\xi^-)] + \epsilon^2 v_w \tag{62a}$$

$$[\![P]\!] \equiv P_e^+(s) - P_e^-(s) = -\epsilon^{3/2}\left[\tilde{p}_p^+(\xi^+) - \tilde{p}_p^-(\xi^-) + \left(\frac{A^+}{\sqrt{\xi^+}} + \frac{A^-}{\sqrt{\xi^-}}\right)(1-a_3)\right] - \epsilon^2 \rho_w U_w c_w \kappa \tag{62b}$$

The "w" subscripted quantities are defined by Eqs. (9).

The terms containing A^+ and A^- in the above equations are contributions from the common-part terms. Note, there are no common-part contributions to the

normal-velocity component terms in the wake or to the pressure distributions on the airfoil surface since these common-part contributions vanish to the order of terms retained in Eqs. (59). The formula given in Eq. (59) for $\mathcal{P}_e(s)$ provides composite solutions for the pressure on the airfoil surface and wake axis as corrected for pressure variations across the boundary layer and wake.

The matching conditions given in Eqs. (61) and (62) form a sum-type composite expansion being given by the sum of a boundary-layer type solution plus the trailing-edge solution minus the common part. The added terms from the trailing-edge solution cancel the singular contributions appearing in the boundary-layer solution (Eqs. 14c, d) resulting in "corrected" viscous matching conditions that are uniformly valid in the "outer" boundary-layer and "inner" trailing-edge regions. The modified matching conditions are valid in a formal asymptotic sense for the limit $Re \to \infty$. In our applications of these equations, the inner trailing edge solution is not carried out to the same order as the outer boundary-layer solution. Consequently, in this situation, the singular terms in the outer and inner solutions will not be identical, but will differ by terms that are formally of higher order than 0 ($\varepsilon^{3/2}$). Thus, although the inner and outer solutions will formally match term by term if Eqs. (59) - (62) are expanded in Re, the singular terms will not exactly match in our method where the outer boundary-layer solution is not expanded in a formal asymptotic expansion. This would lead to technical problems in numerical solutions based on Eqs. (59) - (62). The problem can be avoided and a form suitable for numerical computation can be obtained by rearranging part of the matching conditions into a multiplicative-type composite solution. Thus, if we consider the boundary-layer and trailing edge solutions as the "outer" and "inner" viscous solutions, we can replace Eq. (59a) by:

$$\mathcal{U}_e(s) = \begin{cases} V_e(s) - \epsilon^2 v_\sigma(s) \left[\dfrac{\tilde{v}_n(\xi)}{\tilde{v}_{cp}(\xi)}\right] & \text{(airfoil)} \qquad (63a) \\ V_e(s) - \epsilon^{3/2} a \tilde{v}_p(\xi) - \epsilon^2 v_\sigma(s) & \text{(wake)} \qquad (63b) \end{cases}$$

where

$$\frac{\tilde{v}_n}{\tilde{v}_{cp}} = \sqrt{|s - s_{te}|}\, K \qquad (64a)$$

$$K = -\frac{1}{B^{1/2}\delta^{1/2}(1+a_3)} \left[\frac{\bar{\sigma}_1(\xi) + \tilde{\pi}\bar{\sigma}_2(\xi)}{1+\tilde{\pi}}\right] \qquad (64b)$$

The leading order ($\varepsilon^{3/2}$) term in the source velocity given by Eq. (63) is continuous across the trailing edge, but the second-order term is discontinuous with a small jump across the trailing edge. This jump is a consequence of the viscid-inviscid interaction, which acts to smooth the corner formed by the airfoil surface and the dividing streamline of the viscous flow leaving the trailing edge (see Fig. 8). The value of the constant, a, is determined from the condition that the jump in source velocity across the trailing edge is equal to $\mathcal{U}(s_{te})\tan\beta(s_{te})$, where

$\mathcal{U}(s_{te})$ and $\beta(s_{te})$ are the values of the composite velocity and wake streamline angle at the trailing edge. With this condition and Eq. (64), we can rearrange Eq. (63) into the form,

$$\mathcal{U}_e(s) = \begin{cases} V_e(s) - \epsilon^2 v_\sigma(s)\sqrt{|s - s_{te}|}\,K(\xi) & \text{(airfoil)} \quad (65a) \\ V_e(s) - D\,\bar{K}(\xi) - \epsilon^2 v_\sigma(s) & \text{(wake)} \quad (65b) \end{cases}$$

where

$$\bar{K} = \frac{\bar{\sigma}_1(\xi) + \tilde{\pi}\bar{\sigma}_2(\xi)}{\bar{\sigma}_1(0) + \tilde{\pi}\bar{\sigma}_2(0)} \qquad (65c)$$

$$D = V_e(s_{te}) - \epsilon^2 v_\sigma(s_{te}) - \mathcal{U}_e(s_{te})\tan\beta(s_{te}) \qquad (65d)$$

where $V_e(s_{te})$ is the limiting trailing edge value from the airfoil side as determined from Eq. (65a) and $v_\sigma(s_{te})$ is the limiting value from the wake side.

In the above formulae, a multiplicative-type representation is used for the velocity on the airfoil surface while a sum-type representation is used in the wake. A multiplicative-type composite solution is not possible in the wake because the common part vanishes in the wake to the order of the terms retained in Eq. (65). However, the above representation is sufficient for our purposes. The square root term appearing in Eq. (65a) cancels the corresponding singular term appearing in the boundary-layer solution, $v_\sigma(s)$ for $s \to s_{te}$. This leads to a smooth solution near the trailing edge, independent of the order of the terms carried in the inner and outer viscous solutions. The parameter, D, is a scaling parameter introduced to assure a continuous transition of the inner solution across the trailing edge. The representation in Eqs. (65) is formally equivalent to the original sum-type composite expansion in Eq. (59a) in the sense that the difference between the two solutions is less than $O(\varepsilon^2)$.

The same considerations lead to the following representation for the airfoil surface and wake pressure distribution. Thus,

$$\mathcal{P}_e(s) = \begin{cases} P_e(s) - \epsilon^{3/2}\bar{I}(\xi)\,[\![P(s_{te})]\!] - \epsilon^2 p_\sigma(s) & \text{(airfoil)} \quad (66a) \\ P_e(s) - [\![P(s)]\!] & \text{(wake)} \quad (66b) \end{cases}$$

where

$$[\![P]\!] = \epsilon^2 p_\sigma(s)\sqrt{|s - s_{te}|}\, I(\xi) \quad (67a)$$

$$[\![P(s_{te})]\!] = P_e(s_{te}) - \mathcal{P}_e(s_{te}) \quad (67b)$$

$$I = \frac{1}{B^{1/2}\delta^{1/2}(1-a_3)}\left[\frac{\bar{\beta}_1(\xi) + \bar{\pi}\bar{\beta}_2(\xi)}{1+\bar{\pi}}\right] \quad (67c)$$

$$\bar{I} = \frac{\bar{\beta}_1(\xi) + \bar{\pi}\bar{\beta}_2(\xi)}{\bar{\beta}_1(0) + \bar{\pi}\bar{\beta}_2(0)} \quad (67d)$$

The viscous matching conditions can be obtained directly from the above representation for the velocity $\mathcal{U}_e$ and pressure $\mathcal{P}_e$. The condition that the normal velocity component vanish on the airfoil yields

$$V_e(0) = \epsilon^2 v_\sigma(s)\sqrt{|s - s_{te}|}\, K(\xi) \quad (68)$$

The requirement that the viscous solution be continuous across the wake axis leads to the following expressions for the jump in source velocity $[\![V]\!]$ and pressure $[\![P]\!]$ across the wake:

$$[\![V]\!] = [D^+\bar{K}^+(\xi^+) - D^-\bar{K}^-(\xi^-)] + v_w(s) \quad (69a)$$

$$[\![P]\!] = [\![P]\!]^+ - [\![P]\!]^- \quad (69b)$$

The matching conditions for the circulation, Γ, follow from Eq. (69b) and the relation

$$\frac{d\Gamma}{ds} = [\![U]\!] = -\frac{1}{\rho_w U_w}[\![P]\!] + O([\![P]\!]^2) \quad (70)$$

Thus, substitution of Eq. (69b) into Eq. (70) followed by some rearrangement leads to the expression

$$d\Gamma = \epsilon^2 c_w\,[\sqrt{|s - s_{te}|}\; J_w]\, d\beta \quad (71a)$$

where

$$J_w(s) = \left[\frac{1}{B^{1/2}(1-a_3)}\right]\left[\frac{1}{(\delta^+)^{1/2}}\left(\frac{\delta^*_+ + \theta^+}{\delta^*_w + \theta_w}\right)\left(\frac{\bar{\beta}_1(\xi^+) + \bar{\pi}^+\bar{\beta}_2(\xi^+)}{1+\bar{\pi}^+}\right)\right.$$

$$\left. + \frac{1}{(\delta^-)^{1/2}}\left(\frac{\delta^*_- + \theta^-}{\delta^*_w + \theta_w}\right)\left(\frac{\bar{\beta}_1(\xi^-) + \bar{\pi}^-\bar{\beta}_2(\xi^-)}{1+\bar{\pi}^-}\right)\right] \quad (71b)$$

and

$$\delta^*_w = \delta^*_+ + \delta^*_- \qquad \theta_w = \theta^+ + \theta^- \quad (71c)$$

Equations (68), (69) and (71) constitute the principal results of our viscous theory. These equations provide all the boundary conditions needed to determine the second-order, outer, inviscid solution. The formulae provide a rational method for correcting the matching conditions of conventional interacting boundary layer to account for strong-interaction effects near trailing edges of cusped airfoils.

Before concluding this section we provide alternative formulae for determining the pressure on the airfoil and in the wake which are required in the solution of the boundary-layer equations. The composite solution for the pressure on the wake axis is given by Eq. (66b). Following some straightforward algebraic manipulations, it can be expressed in terms of the inviscid quantity $P_e(s)$ and a boundary-layer function λ^*, as follows:

$$\mathcal{P}_e(s) = P_e^+(s) - \frac{\lambda}{1+\lambda}[\![P]\!] \tag{72a}$$

where

$[\![P]\!] = P_e^+(s) - P_e^-(s)$ and λ is defined by

$$\lambda = \left(\frac{\delta_+^* + \theta^+}{\delta_-^* + \theta^-}\right)\left[\frac{(\delta^+)^{1/2}(1+\bar{\pi}^+)}{(\delta^-)^{1/2}(1+\bar{\pi}^-)}\right]\left[\frac{\bar{\beta}_1(\xi^+) + \bar{\pi}^+\bar{\beta}_2(\xi^+)}{\bar{\beta}_1(\xi^-) + \bar{\pi}^-\bar{\beta}_2(\xi^-)}\right] \tag{72b}$$

The pressure on the airfoil surface can be written in the form

$$\mathcal{P}_e(s) = P_e(s) - \epsilon^{3/2}[\![P(s_{te})]\!]\left[\frac{\bar{\beta}_1(\xi) + \bar{\pi}\bar{\beta}_2(\xi)}{\bar{\beta}_1(0) + \bar{\pi}\bar{\beta}_2(0)}\right] - \epsilon^2 p_0(s) \tag{73a}$$

where

$$[\![P(s_{te})]\!] = P_e(s_{te}) - \mathcal{P}_e(s_{te}) \tag{73b}$$

The last two terms in Eq. (73a) account for the $O(\epsilon^{3/2})$ and $O(\epsilon^2)$ variation in pressure across the boundary layer.

2.5 SUMMARY OF THE CORRECTED MATCHING CONDITIONS

In the theory presented in this report, the inviscid and viscous solutions are coupled through viscous matching conditions, just as in the standard interacting boundary-layer theory. In the new theory, however, the matching conditions are corrected as described in the previous subsection to account for strong interaction and normal pressure-gradient effects in the trailing-edge region. The resulting numerical problem is then very similar to the problem arising in standard interacting boundary-layer theory. In both theories the inviscid and boundary-layer equations are solved by iteration to obtain self-consistent solutions satisfying the matching conditions coupling the two solutions. The new features arising in the present method are concerned with corrections to the matching conditions and the need to accommodate the wake matching conditions in the numerical solution. The new matching conditions are summarized below:

Source velocity:

$$V_e(s) = \epsilon^2 V_\sigma \left[\sqrt{|s - s_{te}|}\, K\left(\frac{s_{te} - s}{B\delta} \right) \right] \qquad \text{(airfoil)} \qquad (74a)$$

$$[\![V]\!](s) = \left[D^+ \bar{K}\left(\frac{s - s_{te}}{B\delta^+} \right) - D^- \bar{K}\left(\frac{s - s_{te}}{B\delta^-} \right) \right] + \epsilon^2 V_w \qquad \text{(wake)} \qquad (74b)$$

Wake circulation:

$$\Gamma(s) = \Gamma_\infty + \epsilon^2 \int_{\beta_{te}}^{\beta} c_w \sqrt{s - s_{te}}\, J_w(s)\, d\beta \qquad (74c)$$

Pressure distribution:

$$\mathcal{P}_e(s) = P_e(s) - \epsilon^{3/2}[\![P(s_{te})]\!]\,\bar{I}\left(\frac{s - s_{te}}{B\delta}\right) \pm \rho_e U_e^2 \kappa\,(\delta^* + \theta) \qquad \text{(airfoil)} \qquad (74d)$$

$$\mathcal{P}_e(s) = P_e^+(s) - \frac{\lambda}{1+\lambda}[\![P]\!] \qquad \text{(wake)} \qquad (74e)$$

where

$$[\![P]\!] = P_e^+ - P_e^-$$

The trailing edge corrections used in the above coupling conditions are strictly applicable only to airfoils with cusped trailing edges. Although the local strong interaction theory can, in principle, be generalized to wedge shaped trailing edges, this has not as yet been done. The present theory as formulated in Eqs. (74) leads to an equivalent source velocity and flow deflection that has a discontinuity that exactly cancels the geometric corner at the trailing edge of an airfoil with a wedge shaped trailing edge. This is exactly the same behavior as in standard interacting boundary layer theory. This discontinuity in source velocity across the trailing edge requires us to modify the determination of the constant D defined by Eq. (65d). For airfoils with included trailing edge angles, θ_{te}, the equation for the scaling parameter, D, should be changed to,

$$D^{\pm} = V_e^{\pm}(s_{te}) - \epsilon^2 v_\sigma^{\pm}(s_{te}) - \mathcal{U}(s_{te}) \tan[\beta(s_{te}) \pm \theta_{te}/2] \qquad (74f)$$

where the last term accounts for the jump in source velocity due to the nonzero trailing edge angle.

3. OUTER (POTENTIAL FLOW) SOLUTION

In this section we outline the procedures used to solve the outer inviscid problem, assuming the boundary-layer quantities appearing in the matching conditions are known from a previous iteration. The solution in the outer inviscid region is based on a potential-flow approximation which should be adequate for weak shock waves. We employ Jameson's (Refs. 6 & 7) hybrid, relaxation/direct-solver scheme for solving the full-potential equation in conservative form. The particular version we employ is described in Ref. 7. For completeness, we briefly review Jameson's scheme and indicate where modifications are necessary to accommodate the viscous matching conditions.

3.1 GOVERNING EQUATIONS AND BOUNDARY CONDITIONS

Jameson's method is carried out in a computational plane that is developed from the conformal transformation of the region exterior to the airfoil to the interior of the unit circle. A polar coordinate system, (r, ω) is used in the circle plane to generate a desirable grid system for the finite-difference approximation. The potential-flow problem to be solved in the circle plane is indicated in Fig. 7. The conservation equation for the velocity potential in the circle plane can be written in the form

$$\frac{\partial}{\partial \omega}(RQ_{\omega}) + \bar{r}\,\frac{\partial}{\partial \bar{r}}(RQ_{\bar{r}}) = 0 \tag{75}$$

where

$$Q_{\omega} = \frac{\partial \Phi}{\partial \omega}, \quad Q_{\bar{r}} = \bar{r}\,\frac{\partial \Phi}{\partial \bar{r}} \tag{76}$$

and where, in the notation of the previous section, R is the density in the outer (inviscid region) and $Q_{\bar{r}}$ and Q_{ω} are the mapped velocity components in the $\bar{r}$ and ω directions, respectively. If $\mathcal{K}/r$ is the modulus of the transformation of the airfoil into the exterior of the circle, the physical velocity components in the $\bar{r}$ and ω directions may be written as

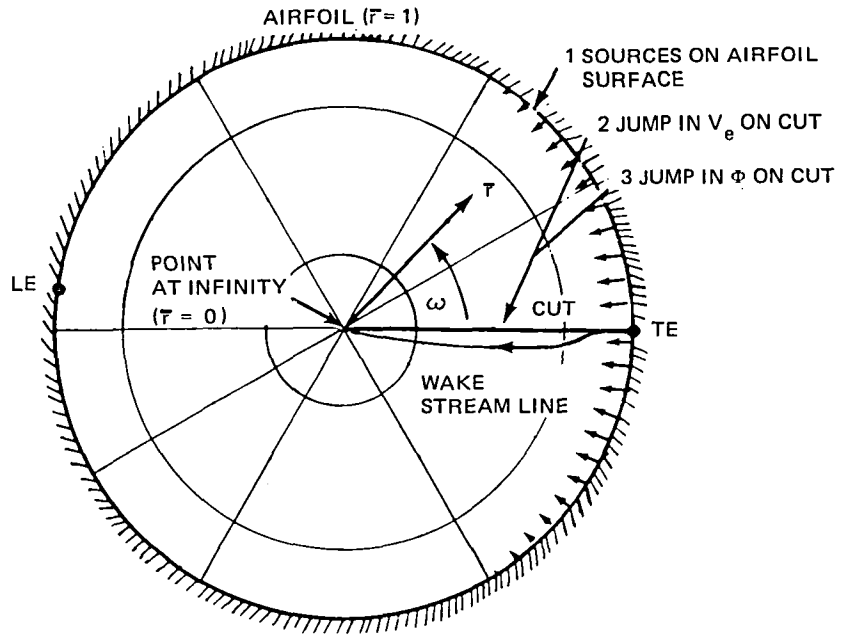

Figure 7 Computational Domain for the Inviscid Problem

$$q_\omega = \frac{\bar{r} Q_\omega}{\mathcal{H}}, \quad q_{\bar{r}} = \frac{\bar{r} Q_{\bar{r}}}{\mathcal{H}} \tag{77}$$

The density, R, is determined from speed of sound, a, and the energy equation in isentropic flow, as follows

$$a^2 = a_0^2 - \frac{\gamma - 1}{2} (q_{\bar{r}}^2 + q_\omega^2) \tag{78a}$$

$$R = (M_\infty^2 a^2)^{1/\gamma - 1} \tag{78b}$$

where a_o is the stagnation speed of sound. The uniform free stream and the net mass flow from the boundary layer introduce singularities at the origin, $\bar{r} = 0$, in the circle plane. These are removed by introducing a reduced potential, G, defined by

$$G = \Phi - \frac{\cos(\omega + \alpha)}{\bar{r}} - \epsilon^2 \sigma_d \ln \bar{r} + E(\omega + \alpha) \tag{79a}$$

where $2\pi E$ is the circulation at infinity and σ_d is the source flow at infinity introduced by the boundary layer and wake. Thus,

$$E = \lim_{\bar{r} \to 0} \frac{\Gamma(\bar{r})}{2\pi} \tag{79b}$$

$$\epsilon^2\sigma_d = \lim_{\bar{r}\to 0} \frac{\delta_w^*(\bar{r})}{2\pi B_\infty} \tag{79c}$$

where

$$B_\infty = \sqrt{1 - M_\infty^2} \tag{79d}$$

The transformation leads to a reduced potential that is single-valued and bounded at infinity. The corresponding far-field boundary condition is

$$\lim_{\bar{r}\to 0} G = E\{(\omega+\alpha) - \tan^{-1}[B_\infty \tan(\omega+\alpha)]\} - \frac{\epsilon^2\sigma_d}{2} \ln[1 - M_\infty^2 \sin^2(\omega+\alpha)] \tag{80}$$

The last term in Eq. (80) arises from the viscous-induced source flow at infinity. The mapped velocity components Q_r and Q_ω can be written in terms of the reduced potential as

$$Q_\omega = \frac{\partial G}{\partial \omega} - E - \frac{\sin(\omega+\alpha)}{\bar{r}} \tag{81a}$$

$$Q_{\bar{r}} = \bar{r}\,\frac{\partial G}{\partial \bar{r}} - \frac{\cos(\omega+\alpha)}{\bar{r}} + \epsilon^2\sigma_d \tag{81b}$$

The boundary condition on the airfoil surface (r = 1) is

$$\frac{\partial G}{\partial \bar{r}} = \cos(\omega+\alpha) - \epsilon^2\sigma_d + \mathcal{K}V_e \tag{82}$$

where V_e is the surface-source velocity defined in Eqs. (68).

To be consistent with the theoretical analysis, the wake boundary conditions should be imposed along a reference curve that is close to the wake, say within 0 (ε) from the wake centerline. We stress the fact that the reference wake axis need not be a streamline, but that it must only meet the requirement that it be sufficiently close to the wake centerline. In the present study we align the reference wake axis with the radial cut $\omega = 0$ in the circle plane as sketched in Fig. 8. Both the "cut" and the inviscid streamline are tangent to the airfoil bisector at the trailing edge. With this choice, the wake axis is tangent to the trailing streamline of the inviscid solution and will, therefore, be positioned close to the wake near the trailing edge.

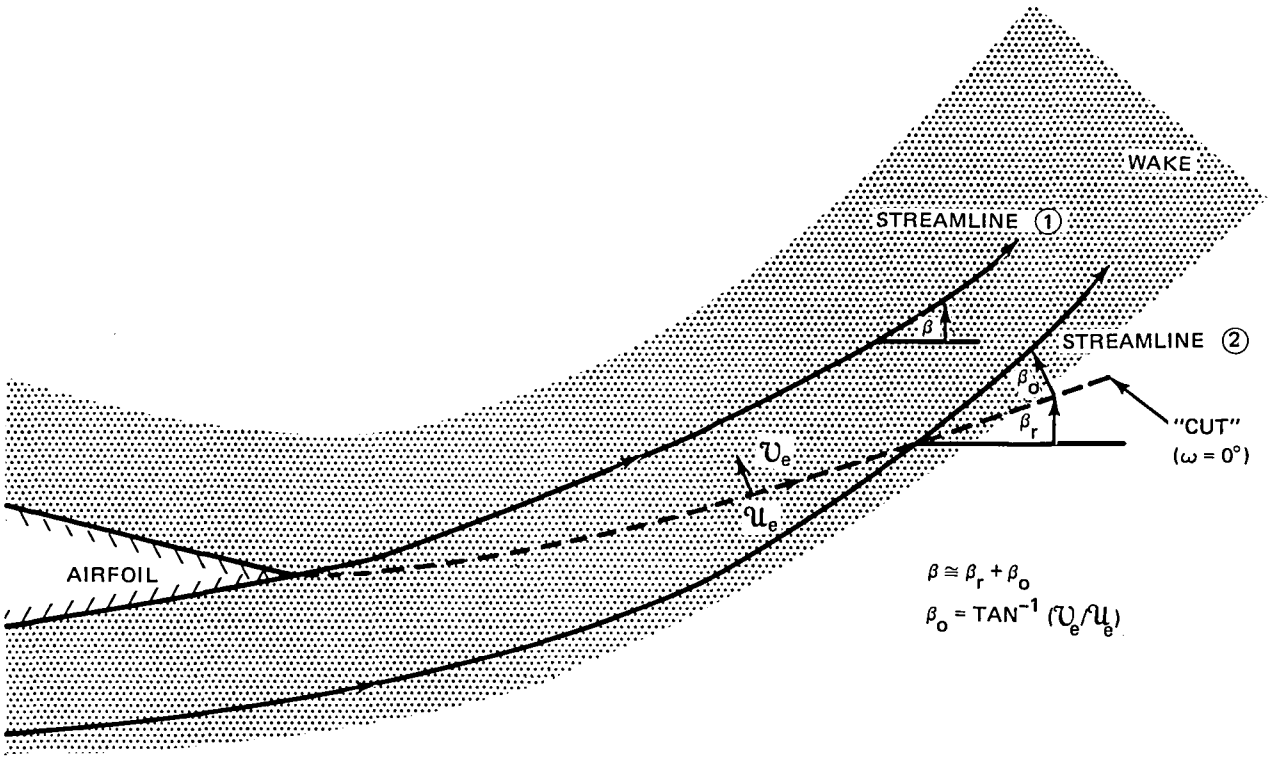

Figure 8 Wake Reference Axis

Since the wake matching terms decrease rapidly away from the trailing edge and are quite small at distances greater than the present chord, the approximation should be more than adequate. Thus, the matching conditions in the wake along $\omega = 0$ can be written in the form

$$\left(\frac{\partial G}{\partial \omega}\right)^{+} - \left(\frac{\partial G}{\partial \omega}\right)^{-} = E + \sin(\omega + \alpha) + \mathcal{K}[\![V]\!] \tag{83a}$$

$$G^{+} - G^{-} = \Delta\Gamma(\bar{r}) \equiv \Delta\Gamma(\bar{r}) - \Gamma(0) \tag{83b}$$

where $[\![V]\!]$ is the jump in source velocity given by Eq. (69a) and $\Gamma(r)$ is the circulation distribution along the wake which is determined from the integration of Eq. (17a) subject to the boundary condition at $r = 0$

$$\Gamma(0) = 2\pi E \tag{84}$$

The circulation at infinity ($\bar{r} = 0$) and the constant E are determined from the Kutta condition requiring the velocity at the trailing edge to be bounded. This is satisfied by requiring Q_ω to be zero at the trailing edge. Therefore, from Eq. (81) we arrive at the following condition for E

$$E = \sin\alpha + \frac{\partial G}{\partial \omega} \quad \text{at } \bar{r} = 1,\ \omega = 0 \tag{85}$$

The determination of Γ (r) from Eq. (71a) requires knowledge of the wake angle, β. In the present work β is defined to be equal to the angle between the extension of

the airfoil chord and the composite streamline leaving the trailing edge (streamline 1 in Fig. 8). If this streamline is assumed to be close to the position of the cut, then a sufficiently accurate approximation is

$$\beta = \beta_r + \beta_0 + O(y_{cut} - y_0) \tag{86}$$

where β_r is the angle between the radial line $\omega = 0$ and the extension of the airfoil chord and β_0 is the local flow angle at the "cut" as depicted in Fig. 8. The local flow angle, β_0, can be determined from the composite solutions for the two velocity components $\mathcal{U}_e, \mathcal{U}_e$ at the cut, $\omega = 0$; thus, by definition

$$\beta_0 = \tan^{-1}(\mathcal{U}_e/\mathcal{U}_e) \tag{87}$$

where $\mathcal{U}_e$ is evaluated from Eq. (65b) using the modified expression for the scaling parameter D given in Eq. (74f)

$$\mathcal{U}_e(S) = V_e(s) - D\bar{K}(\xi) - \epsilon^2 v_\sigma(s) \tag{88}$$

The error term, $(y_{cut} - y_0)$ appearing in Eq. (86) is the distance between the cut and the wake centerline. For inviscid flow, the terms σ_d, V_e and $[\![V]\!]$ are zero, the circulation, Γ, is equal to $2\pi E$ and the above formulation reduces exactly to Jameson's original fully-conservative scheme for the full potential equation.

3.2 NUMERICAL SOLUTION

The outer inviscid problem formulated above is solved by Jameson's (Refs. 6 and 7) fully-conservative relaxation method. The method employs a rotated-difference scheme and a convergence acceleration technique based on a combined SLOR-Poisson direct solver. Convergence is improved by carrying out the computations on a sequence of three meshes. Options for a standard non-conservative formulation are also programmed into the method. The basic numerical method is fully described in the original references (Refs. 6 and 7). Here, we describe only the changes needed to accommodate the viscous terms in the boundary conditions.

The computational grid employed in the calculations is indicated in Fig. 9 together with a sketch illustrating the grid distribution in the physical plane. The flow field in the computational plane is contained between the airfoil surface $\bar{r} = 1$, the "point" at infinity $\bar{r} = 0$, and the two sides of the "cut" $\omega = 0$, $\omega = 2\pi$. The computational mesh consists of interior points, image points used to satisfy the airfoil boundary condition and overlap points employed to satisfy the wake matching conditions. The indices i, j are used to label grid points on the ω, r axes, respectively. The present method overlaps the grid on both the upper and lower sides

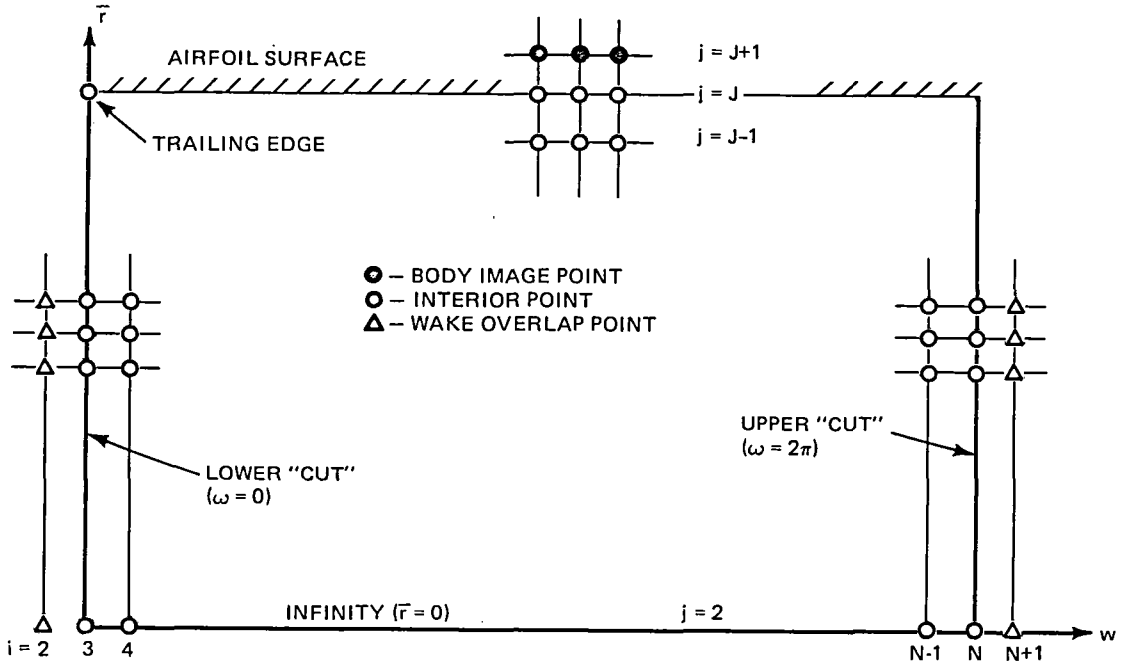

a) CIRCLE PLANE

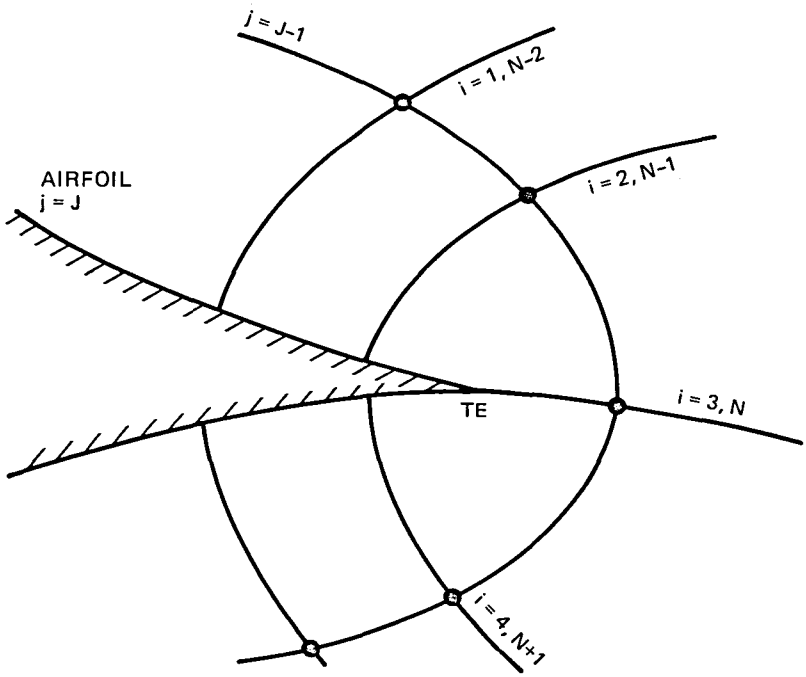

b) PHYSICAL PLANE

Figure 9 Computional Grid

of the cut, in contrast to Jameson's original method which uses overlap points only on the lower side of the cut.

The body boundary condition is imposed by inserting appropriate values of mass flux normal to the airfoil surface, $RQ_{\bar{r}}$, into the image points. The values at the image points (i, J+1) are obtained by setting the mass flux at the surface, j = J, equal to the average of the points (J + 1) and (J - 1). Thus,

$$(RQ_{\bar{r}})_{i,J+1} = -(RQ_{\bar{r}})_{i,J-1} - 2\,\mathcal{K}\,R_e V_e \tag{89}$$

The wake conditions are imposed by setting appropriate values of the potential into the overlap, i = 2, and "cut", rows i = N. The solution in the overlap row, i = N + 1, is used in the derivation of the wake conditions but is not actually employed in the numerical solution. The arrangement of the grid points across the cut is indicated in Figs. 9 and 10. The reflection rules for the determination of the potentials $\Phi_{2,j}$ and $\Phi_{N,j}$ can be found from the finite-difference expressions for the jumps in G, G_ω and $G_{\omega\omega}$ across the cut. Thus, from the definition of Γ we have

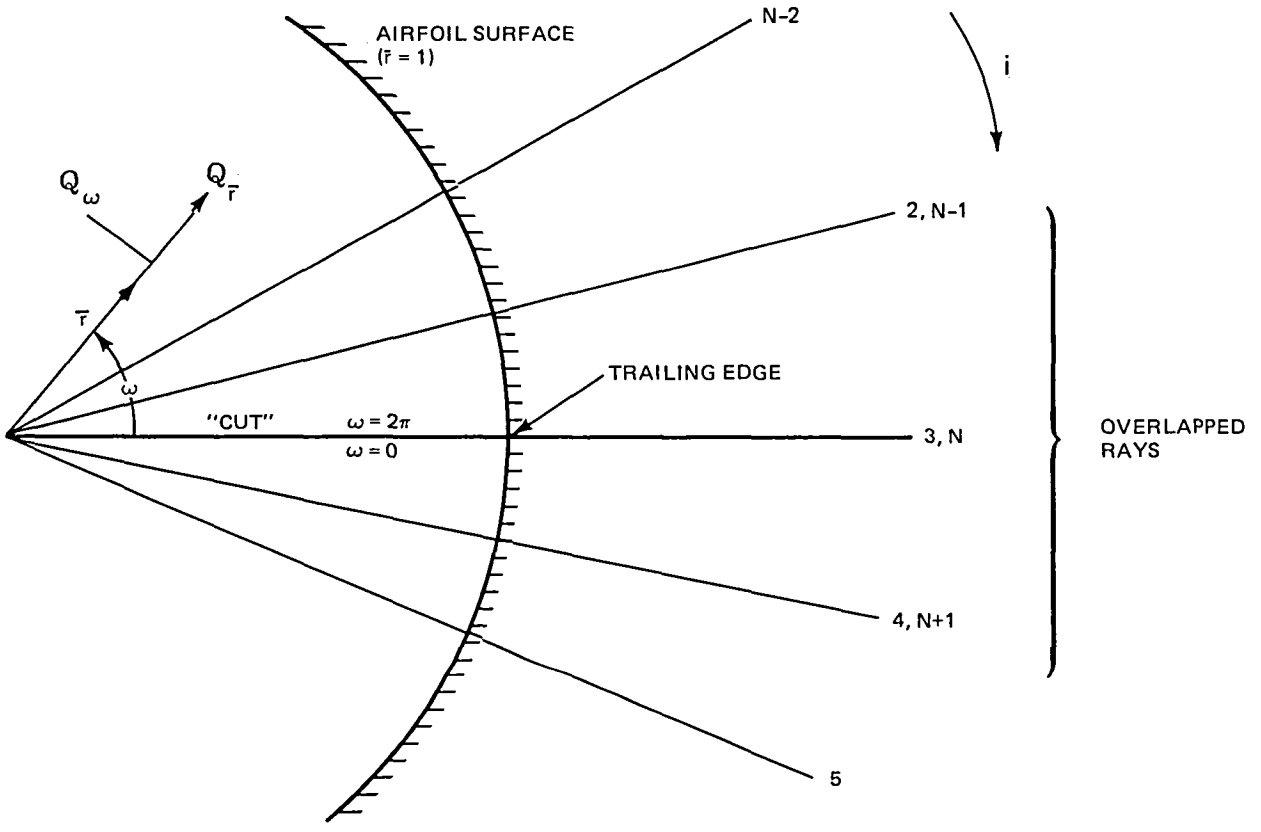

Figure 10 Wake Overlap Rays

$$G_{N,j} = G_{3,j} + \Delta\Gamma_j \tag{90}$$

where $\Delta\Gamma_j$ is the value of $\Delta\Gamma$ at $r = r_j$. By using centered-difference expressions for G_ω on both sides of the cut in Eq. (83a), we can obtain the following expression for the mass-flux discontinuity across the cut

$$(G_{N+1,j} - G_{N-1,j}) - (G_{4,j} - G_{2,j}) = -2\Delta\omega\mathcal{H}[\![V]\!] \tag{91}$$

Similarly, an expression for the jump in $G_{\omega\omega}$ across the cut can be obtained in the form

$$(G_{N+1,j} - 2G_{N,j} + G_{N-1,j}) - (G_{4,j} - 2G_{3,j} + G_{2,j}) = \Delta\omega^2 [\![G_{\omega\omega}]\!] \tag{92}$$

where $[\![G_{\omega\omega}]\!]$ is the jump in $G_{\omega\omega}$ across the cut. A procedure for the evaluation of $[\![G_{\omega\omega}]\!]$ is given below. These equations can be used to express $G_{2,j}$ and $G_{N+1,j}$ in terms of $G_{N-1,j}$ and $G_{4,j}$, respectively. Thus,

$$G_{2,j} = G_{N-1,j} - \Delta\Gamma_j + \Delta\omega\mathcal{H}[\![V]\!] - \tfrac{1}{2}\Delta\omega^2[\![G_{\omega\omega}]\!] + O(\Delta\omega^3) \tag{93a}$$

$$G_{N+1,j} = G_{N-1,j} + \Delta\Gamma_j\ \Delta\omega\mathcal{H}[\![V]\!] + \tfrac{1}{2}\Delta\omega^2[\![G_{\omega\omega}]\!] + O(\Delta\omega^3) \tag{93b}$$

The solution is carried out by sweeping the field along columns i = constant from the leading edge towards the trailing edge, first on the lower surface and then on the upper surface. In carrying out the sweep on the lower surface, the value of $G_{2,j}$ is used from Eq. (93a) with $G_{N-1,j}$ and Γ evaluated from the previous sweep. The sweep on the upper surface employs the potential $G_{N,j}$ as determined from Eq. (90) as a boundary value in the solution. The circulation is obtained from an integration of Eq. (71a) using a simple central difference approximation to yield

$$\Gamma_{j+1} = \Gamma_j + \frac{\epsilon^2}{2}\left[(c_w\sqrt{|s - s_{te}|}\,J_w)_{r=r_j+1} + (c_w\sqrt{|s - s_{te}|}\,J_w)_{r=r_j}\right](\beta_{j+1} - \beta_j) \tag{94a}$$

with

$$\Gamma_2 = 2\pi E \tag{94b}$$

The value of E is determined from the Kutta condition, expressed in finite-difference form as

$$E = \frac{G_{4,J} - G_{2,J}}{2\Delta\omega} - \sin\alpha + O(\Delta\omega^2) \tag{95}$$

The second-derivative term, $[\![G_{\omega\omega}]\!]$, could be determined from the differential equation evaluated on each side of the cut. However, we follow a simpler procedure and evaluate this term numerically from central difference formulae centered one grid

point on either side of the cut. This provides a first-order accurate estimate for $[\![G_{\omega\omega}]\!]$ which is sufficient to evaluate the second-order terms in Eq. (93). Thus, we can write

$$[\![G_{\omega\omega}]\!] = (G_{\omega\omega})_{N-1,j} - (G_{\omega\omega})_{4,j} + O(\Delta\omega) \tag{96a}$$

and hence

$$[\![G_{\omega\omega}]\!] = [\,(G_{N,j} - 2G_{N-1,j} + G_{N-2,j}) - (G_{5,j} - 2G_{4,j} + G_{3,j})\,]/\Delta\omega^2 + O(\Delta\omega) \tag{96b}$$

The flow angle β_j appearing in the equation for the circulation, Eq. (94a), is determined from the velocities on the cut through Eqs. (86) - (88). To minimize numerical error we compute $\mathcal{U}_e$ as the average of $\mathcal{U}_e^{\pm}(s)$ on the upper and lower surfaces of the wake. Thus $\mathcal{U}_e(s)$ in Eq. (87) is computed from the following expression

$$\mathcal{U}_e(s) = \tfrac{1}{2}[\mathcal{U}_e^{+}(s) + \mathcal{U}_e^{-}(s)] \tag{97}$$

where V^{+}_{e} (s) and $V^{-}e$ (s) appearing in Eqs. (88) and (97) are the velocity components normal to the cut (in Jameson's notation; the q_ω component defined by Eq. (77)). These can be expressed in terms of the reduced potential by a central-difference expression of G centered about the column i = N and i = 3, respectively. Thus,

$$V_e^{+}(s) = -\frac{\bar{r}}{\mathcal{H}}\left[\frac{G_{N+1,j} - G_{N-1,j}}{2\Delta\omega} - E - \frac{\sin\alpha}{\bar{r}}\right] \tag{98a}$$

$$V_e^{-}(s) = -\frac{\bar{r}}{\mathcal{H}}\left[\frac{G_{4,j} - G_{2,j}}{2\Delta\omega} - E - \frac{\sin\alpha}{\bar{r}}\right] \tag{98b}$$

where the potentials $G_{N+1,j}$ and $G_{2,j}$ appearing in the above equations are evaluated from Eq. (93). The evaluation of the composite expression for radial velocity component, $\mathcal{U}$, required in Eq. (87) is described in Section 4.

The formula for determining the velocities from the reduced potential, Eq. (77) are indeterminate at the trailing edge since the metric, $\mathcal{H}$, vanishes at this point. Hence, special formulae are needed to compute both the velocity and potential at this point. In the original inviscid method (Refs. 6 and 7) the velocity at the trailing edge was determined from a simple extrapolation of the velocity from neighboring points on the airfoil side of the trailing edge. In the present work we employ a simple extrapolation from the wake side. Since the velocity variations are more

gradual in the wake, this change provides an improved determination of the velocity at the trailing edge. A special formula is also needed to evaluate the potential at the trailing edge since the transformed potential-flow equation is also indeterminate at this point. We employ the simple interpolation formula used in the inviscid solution in Refs. 6 and 7 based on the grid points indicated in the Fig. 11. Thus, with this scheme the trailing-edge potential, $G_{3,j}$ is determined from the formula

$$\frac{G_{4,J} - 2G_{3,J} + G_{2,J}}{\Delta\omega^2} + \frac{G_{3,J-1} - 2G_{3,J} + G_{3,J+1}}{\Delta\bar{r}^2} = 0 \qquad (99a)$$

A somewhat more complicated procedure based on the use of an approximate Prandtl-Glauert equation in the physical plane near the trailing edge is employed in Ref. (17).

The difference equations are solved for fixed estimates of the boundary-layer parameters V_e, Γ, and $[\![V]\!]$. The equations are solved by the fast iterative scheme described in Refs. 6 and 7 which is based on alternating a sequence of SLOR and Poisson iterative methods. In each work cycle, we first perform a Poisson step, followed by a specified number of relaxation steps. During the computation we monitor the ratio of the maximum residuals at the start and end of a work cycle. When this "residual ratio" is reduced to a prescribed level, the boundary-layer calculations are repeated and the boundary-layer parameters appearing in the matching conditions are updated. The inviscid computations are then repeated. This alternating sequence of inviscid and boundary layer computations is continued until a set of convergence criteria are satisfied. The criteria employed are based on the

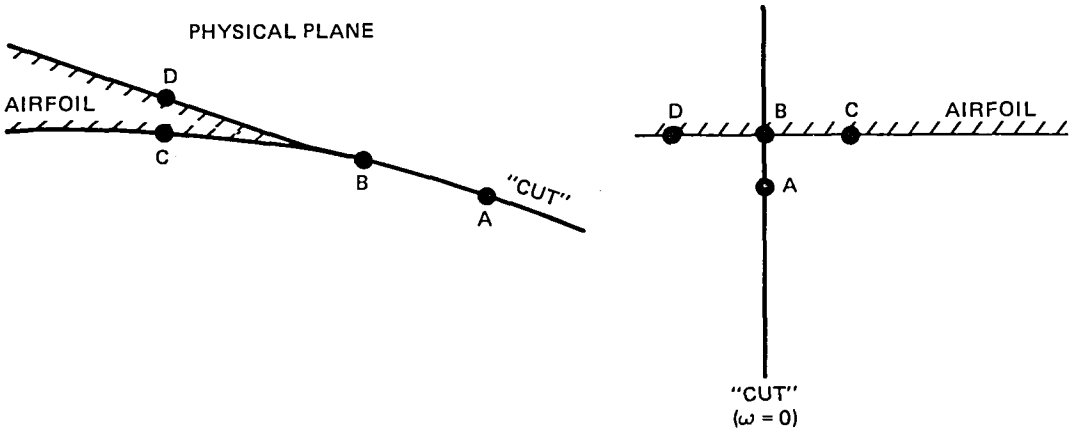

Figure 11 Interpolation Points for the Trailing Edge Potential

maximum residual in the inviscid computation and the change in lift coefficient (α prescribed) or angle of attack (C_L prescribed) between successive work cycles. We also provide for a termination of the computation based on a maximum number of iterations. The calculations are carried out on a sequence of three meshes. The solution on the crude grid is initiated using built-in estimates for the boundary-layer parameters and reduced potential. The solutions on succeeding grids are initiated from interpolated boundary-layer parameters and reduced potentials. The solution on each grid starts with a solution of the inviscid equations.

4. BOUNDARY LAYER SOLUTION

The boundary-layer parameters appearing in the matching conditions are evaluated from solution to the boundary-layer equations with a known pressure distribution determined from the previous iterate. Since the present method accounts for pressure variations across the boundary layer and wake, there is a certain degree of arbitrariness in the choice of the pressure distribution to be used in the boundary layer computations. We could, for example, use the pressure distribution at either the edge of the boundary layer or at the surface or, could use an appropriate average across the boundary layer. Since the pressure variations across the boundary layer and wake are small, being at most of 0 ($\varepsilon^{3/2}$) near the trailing edge, the various choices lead to equivalent solutions, to lowest order in ε. In the present work we use the composite solution for the pressure, $\mathcal{P}_e(s)$, on the airfoil surface, Eq. (73), and cut, Eq. (72a), neglecting the small second-order term $P_\sigma(s)$ appearing in Eq. (73.) In the solution of the boundary layer equations it is assumed the pressure is constant across the boundary layer and is given by $\mathcal{P}_e(s)$.

The edge velocity, $U_{e,w}(s)$, and density, $\rho_{e,w}(s)$, appearing in the boundary layer equations and matching conditions can be evaluated from the exact isentropic relations.

$$U^2_{e,w}(s) = 1 + \frac{[\gamma M^2_\infty \mathcal{P}_e(s)]^{\gamma/\gamma-1} - 1}{(\gamma-1) M^2_\infty/2} \tag{100a}$$

$$\rho_{e,w}(s) = [\gamma M^2_\infty \mathcal{P}_e(s)]^{1/\gamma} \tag{100b}$$

In the evaluation of the flow angle β_o in Eq. (87), we approximate $\mathcal{U}_e(s)$ by $U_w(s)$ as determined from Eq. (100a) which is a consistent approximation to lowest order in ε.

In the present work both the laminar and turbulent boundary-layer equations are solved using simple integral methods. In this section we briefly describe the

methods used to solve the boundary-layer equations and the procedures employed for transition and leading edge separation.

4.1 LAMINAR BOUNDARY LAYER, LEADING-EDGE SEPARATION AND TRANSITION

The laminar boundary-layer equations are solved for δ^*, θ, h and c_f by a compressible version (Ref. 9) of Thwaites' integral method (Ref. 61) for incompressible flow. The laminar equations are integrated from the forward stagnation point to a transition point whose location is either assigned or determined by a specified transition criteria. Three semi-empirical, transition prediction methods have been programmed into our method as user selected options. These include transition criteria based on Crabtree's correlation (Ref. 62), Michel's correlation (Ref. 63), and the correlation in Stevens, Goradia, and Braden (Ref. 64). We also test the laminar solution for leading-edge separation according to the criterion in Ref. 64. If leading-edge separation is present, a diagnostic is written indicating that separation has occurred and whether it is of the long or short bubble type. If transition is not predicted before laminar separation, transition to turbulent flow is assumed to occur at the laminar separation point. The user may choose both an assigned transition location and one of the above transition criteria. In this case the transition point used in the calculations is the most upstream of 1) the assigned location, 2) the position predicted by the transition criteria or 3) the laminar separation point. It is, of course, well known that these and other existing methods of predicting transition are not reliable. They are included in the present method merely as a guide to be used in the absence of any information regarding the position of transition.

The turbulent boundary-layer calculation is initiated at the transition point, generally, under the assumption that the momentum thickness is continuous and the shape factor is discontinuous across transition. The initial value of the shape factor in the turbulent flow is determined under the assumption that the increment in the "incompressible" shape factor, $\bar{h}$, is given by

$$\Delta\bar{h}_t = 1.1 \tag{101}$$

where, in turbulent flow

$$h = (\bar{h} + 1)\left(1 + \frac{r M_e^2}{2}\right) - 1 \tag{102}$$

where r is the recovery factor and M_e is the local Mach number at the boundary layer edge. A more elaborate correlation in Schlichting (Ref. 65) based on the assumption that Δh_t is a universal function of the momentum thickness Reynolds number at transition, can be used in place of Eq. (101). However, the turbulent boundary layer downstream of transition is not sensitive to the initial conditions at transition and the simple relationship given in Eq. (101) is adequate. In our method, we also allow for a jump in momentum thickness, $\Delta\theta_t$, across the transition point. This jump can be used to simulate an increase in momentum thickness due to a roughness strip. Thus, the initial values of the reduced shape factor and momentum thickness employed in the calculation of the turbulent boundary layer are written in the form

$$\bar{h} = \bar{h}_{laminar}(\omega_t) + \Delta\bar{h}_t \tag{103a}$$

$$\theta = \theta_{laminar}(\omega_t) + \Delta\theta_t \tag{103b}$$

where $\omega = \omega_t$ is the circle plane angle of the transition point.

The integrals appearing in the laminar solution are evaluated by a simple trapezoidal rule and the surface source velocity at points where the flow is laminar is evaluated from the following central-difference approximation:

$$V_e(\omega_i) = \left(\frac{1}{\rho_e \mathcal{H}}\right)_i \left[\frac{(\rho_e U_e \delta^*)_{i+1} - (\rho_e U_e \delta^*)_{i-1}}{\omega_{i+1} - \omega_{i-1}}\right] \tag{104}$$

4.2 TURBULENT BOUNDARY LAYER SOLUTION

The solution of the turbulent boundary layer and wake are carried out by the lag-entrainment method of Green et al. (Ref. 10). This is an entrainment-type integral method that includes an approximate treatment of the turbulent energy equation. The method has been demonstrated to provide accurate solutions for airfoil-type flows with large adverse pressure gradients. Such flows arise, for example, near shock waves and trailing edges of rear-loaded supercritical airfoils.

The basic method employs the momentum-integral equation, a shape-factor equation, and a differential equation for the entrainment function. To avoid interpolating between the inviscid and boundary-layer solutions, the latter are integrated in the circle plane using the same grid points employed in the inviscid solution. The

basic equations for the momentum thickness, reduced shape factor, and entrainment function and are written in the form

$$\frac{1}{\mathcal{K}}\frac{d\theta}{d\ell} = \tfrac{1}{2}c_f - (h+2-M_e^2)\frac{\theta}{U_e\mathcal{K}}\frac{dU_e}{d\ell} \tag{105}$$

$$\frac{1}{\mathcal{K}}\frac{d\bar{h}}{d\ell} = \frac{1}{\theta}\frac{d\bar{h}}{dh_1}\left\{ c_e - h_1\left[\tfrac{1}{2}c_f - (h+1)\frac{\theta}{U_e}\frac{dU_e}{d\ell}\right]\right\} \tag{106}$$

$$\frac{1}{\mathcal{K}}\frac{dc_E}{d\ell} = \frac{1}{\theta}F_e \tag{107}$$

where ℓ is equal to the polar angle ω on the airfoil surface and to the radius, r, in the wake (We recall that $\mathcal{K}$ is the modulus of the transformation.). The shape factor, h, is determined from h by Eq. (102) and the displacement thickness is given by

$$\delta^* = h\theta \tag{108}$$

The velocity-profile function, h_1, is given in terms of h by

$$h_1 = 3.15 + \frac{1.72}{(\bar{h}-1)} - .01\,(\bar{h}-1)^2 \tag{109}$$

The skin friction is computed from the following empirical relations

$$c_f = c_{f0}\left[\frac{9\bar{h}_0}{10\bar{h}-4} - \frac{1}{2}\right] \tag{110}$$

where

$$\bar{h}_0 = [1 + 6.55\sqrt{\tfrac{1}{2}c_f(1+.04\,M_e^2)}]^{-1/2} \tag{111a}$$

$$c_{f0} = \frac{1}{F_c}\left[\frac{0.01013}{\log_{10}(F_R R_\theta) - 1.02} - 0.00075\right] \tag{111b}$$

$$F_c = \sqrt{1+.2M_e^2},\quad F_R = 1.0 + 0.056\,M_e^2 \tag{111c}$$

and R_θ is the local Reynolds number based on momentum thickness. The function F_e appearing in the entrainment equation is an empirical function defined in Ref. 10 that depends on boundary-layer parameters, the external-velocity gradient $\frac{1}{Ue}\frac{dU}{ds}e$, and the local external Mach number M_e. This function also involves parameters that permit a rough treatment of the effects of longitudinal curvature and mean dilatation

on the turbulence. The same model is used to solve for both the flow in the boundary layer and the wake. The wake is analyzed as if it were two separate symmetric half wakes.

The integration of Eqs. (105) - (107) is initiated at the transition point using values for h and θ determined from Eqs. (103). The initial value of the entrainment function, C_E, is determined from an equilibrium value defined in Ref. 10. For further details of the model see Ref. 10.

The differential equations are integrated using a standard variable-step Runge-Kutta method. The integrations are carried out on a basic grid formed by the ω nodal values used in the inviscid solution. The integration scheme allows repeated grid halving, subject to an error measure, to maintain accuracy in regions of rapid variation as occur near shock waves and the trailing edge. In this way the solution for the boundary-layer parameters are determined directly at the nodal points of the inviscid flow without interpolation.

A useful expression for the source velocity, v_σ, in turbulent flow can be obtained from the momentum-integral and shape-factor equations. Thus, employing Eqs. (105) and (106) in the definition of v_σ we arrive at the following expression for v_σ as a function of the gradient of the edge velocity U_e:

$$v_\sigma = c_1 - c_2 \frac{dU_e}{ds} \tag{112}$$

where

$$c_1 = \frac{U_e}{2}\left[hc_f + (c_E - \tfrac{1}{2}h_1 c_f)(c_r + 1)\frac{d\bar{h}}{dh_1}\right] \tag{113a}$$

$$c_2 = \theta\,(h+1)\left[h - \frac{(c_E - 1)\,(c_0 + 1)}{(c_r + 1)} - \frac{1}{2}(c_r + 1)\,h_1 \frac{d\bar{h}}{dh_1}\right] \tag{113b}$$

and

$$c_r = 1 + r(\gamma - 1)M_e^2\,,\quad c_0 = 1 + (\gamma - 1)\,M_e^2 \tag{113c}$$

$$\frac{d\bar{h}}{dh_1} = -\frac{(\bar{h} - 1)^2}{1.72 + 0.02(\bar{H} - 1)^3} \tag{113d}$$

In the numerical method, the velocity derivative appearing in Eq. (112) is approximated by a simple centered difference in the circle plane. It is of some interest to note that in the limit $Re \to \infty$, $h \to 1$ and v_σ approaches the following limit (for recovery factor $r = 1$)

$$v_\sigma = U_e\left[\frac{1}{2}\, c_0 c_f - \left(c_0 + \frac{1}{c_0}\right)\delta^* \frac{1}{U_e}\frac{dU_e}{ds}\right] + O(\epsilon^3) \tag{114}$$

The boundary layer thickness, δ, and Coles' wake parameter, $\tilde{\pi}$, are determined by matching the skin friction and displacement thickness corresponding to Coles' compressible law-of-the-wake (Refs. 66 & 67) to the solution of the lag equations just upstream of the trailing edge.

The lag-entrainment method was not designed to deal with separation of the boundary layer. In many cases of interest, small separation zones will appear in airfoils flows, without significant influence on the surface-pressure distribution or other section characteristics. For example, small separation regions can occur at the foot of the shock wave or near the trailing edge without exerting a strong influence on the outer inviscid flow. In the case of shock-induced separation, the shape factor is observed to undergo a very rapid increase as the shock wave is approached, followed by an even steeper decrease behind the shock wave. In these cases, the lag-entrainment method will predict an increase in the shape factor to unrealistically large values (e.g., h 15), completely outside the range of data correlations on which the method is founded. The method will also predict unrealistic values of the skin friction in the separated zone. In order to enable the present method to function in these cases, we have set arbitrary bounds on both the skin friction and shape factor when the flow is separated. Flow separation is predicted in the theory when the skin friction computed by the lag-entrainment method is zero. If separation is predicted, we set an upper bound on h given by h_{max}. Then, if h computed according to Eq. (106) is greater than h_{max}, it is set equal to h_{max}. The value of the upper bound can be specified as part of the input; typically, we take $h_{max} = 4.0$. For the skin friction, we follow Hunter and Reeves (Ref. 68) in their "wake like" model of separation and set $c_f = 0$ if it is predicted to be less than zero in the lag-entrainment solution. This approximation of the skin friction in separation zones can be expected to have only a small influence on the solution since c_f is generally small in the slender separation bubbles that occur on airfoils. The overall accuracy of

this approach to separation is not expected to be very high but it should provide useful estimates of incipient separation at the shock wave or trailing edge.

5. RESULTS

The theoretical method described in previous sections has been developed into a computer code GRUMFOIL to solve the viscous transonic flow over airfoils. A complete description of the most recent version of the code is given in Ref. 69 along with instructions for its operation. In the version of the code used for the present computations, we allow for the choice of the constant, c_2, which controls the accuracy of the difference approximation in the supersonic zone and for the choice of the parameter, Q_c, which determines the Mach number of the switch from a central to a backward difference. The difference formulae are second (first)-order accurate at supersonic points for $c_2 = 1$ (0) independent of the value of Q_c. In this section comparisons of theoretical solutions for various values of c_2 and Q_c are presented to demonstrate the effect of the difference approximation on the solution. We also present solutions that illustrate the effect of switching from a F-C or N-C difference scheme. In the program we also provide an option for deleting the trailing-edge corrections and for selectively dropping each of the terms appearing in the viscous matching conditions. These options are used to generate results which illustrate the effect of wake curvature, wake thickness, and trailing-edge correction on the solution.

Although the basic theory used in the present work formally applies only to closed airfoils with cusped trailing edges, the code can be applied to more general airfoils not satisfying these conditions. Open trailing-edge airfoils are modeled by continuing the airfoil surface downstream with a semi-infinite streamtube. The region outside the airfoil plus extensions is then mapped to the region outside a unit circle with the two edges of the wake streamtube mapped to a single curve in the circle plane. This procedure leads to a constant-thickness airfoil extension and to a solution that is continuous across the wake streamtube. For an open airfoil, we must also prescribe the base pressure and determine the base-drag contribution to the total drag. In the present work we assume the base pressure is equal to the pressure at the trailing edge as given by the viscous solution. This approximation is valid if the base thickness is less than the boundary-layer momentum thickness at the trailing edge. The base drag contribution is usually negative, leading to a

reduction in drag. The contribution is sensitive to the accuracy of the predicted trailing edge pressure and can be significant. Unfortunately, the base drag contribution has been missed in recent investigations (Refs. 12-15).

In this section we also present comparisons of theoretical solutions with experimental data for a series of airfoils tested in various wind tunnels. The influence of wall-interference effects on the wind-tunnel data introduces considerable uncertainty into the interpretation of these comparisons. For small enough models, the main effect of wall interference can be taken into account through standard downwash and blockage corrections to the experimental values of the incidence and free-stream Mach numbers. Unfortunately, reliable estimates for these corrections are not available for most transonic wind tunnels, including all those considered in the present study. Therefore, in the present investigation we avoid interpretational difficulties associated with the angle of attack by comparing theory and experiment at the same (measured) lift coefficient. In these calculations the lift coefficient is prescribed and the angle of attack is adjusted during the relaxation process to satisfy the Kutta-condition at the trailing edge. If reliable incidence corrections were available for a set of data, the difference between the experimental and theoretical incidence could be used to judge the adequacy of the theory. However, because of the absence of reliable incidence corrections, we have not attempted such comparisons in the present study. The problem with blockage corrections also remains. The main effect of wall-induced Mach number corrections is to alter the position of shock waves on the airfoil surface. Mach number corrections as small as $M = 0.001$ can produce noticeable shifts in shock-wave location. When available, we followed the recommendations of tunnel operators in applying Mach number corrections to the data. Unfortunately, accurate blockage corrections to the Mach number were not generally available for most of the wind-tunnel data considered in the present study. Therefore, in carrying out the comparisons presented later in this section, we employed Mach number shifts for each tunnel that produced the best overall agreement between the theoretical and experimental shock locations. Because of the uncertainty in the free-stream Mach number, the conclusions drawn from the present study must be regarded as tentative. More definitive evaluations of the theory must await the availability of interference-free data or accurate wall-interference corrections. All theoretical calculations presented in this report were carried out on a sequence of three ($N_r \times N_\omega$) grids consisting of (40 x 8), (80 x

16) and (160 x 32) points. Except where noted, all calculations were carried out with the fully-conservative, first-order accurate (c_2 - 0, Q_c = 1) version of the method.

5.1 EFFECT OF INVISCID FINITE-DIFFERENCE PARAMETERS ON SOLUTION ACCURACY

The formal accuracy of the windward finite-difference approximation employed in and near the supersonic zone is controlled by the parameter c_2, with the solution being first-order accurate for c_2 = 0 and second-order for c_2 = 1. Here we present typical results which illustrate the effect of c_2 on the solution. In general, convergence slows and the solution becomes more difficult to obtain as c_2 is increased from zero to one. Fortunately, convergence is facilitated by reducing the value of the parameter, Q_c, which controls the points at which the numerical scheme is switched from central to backward differences. In the basic setup, Q_c = 1 and the switch is made at the sonic line (M = Q_c = 1). Reducing Q_c below one tends to smooth the solution near shock waves and to speedup convergence. This smoothing effect of Q_c is especially helpful for values of c_2 close to one. We have been able to routinely obtain fully second-order results (c_2 = 1) with Q_c = 0.9. We should stress that the finite-difference approximation is formally second-order accurate for c_2 = 1 independent of the value of Q_c.

To illustrate the effect of c_2 on inviscid solutions we carried out fully-conservative computations on an RAE 2822 airfoil at M = 0.725 for three values of C_L with various combinations of c_2 and Q_c. This resulted in supercritical flow with shock waves in all cases. The results for C_D, α, and shock position, X_s, are summarized in Table 1.

We first note, the choice of Q_c has only a minimal effect on the solutions for fixed values of c_2. Second, and more importantly, we note that the solutions for all three values of C_L, are only weakly dependent on the value of c_2. The drag coefficient is seen to increase by only two counts in going from a first-order (c_2 = 0) to a second-order (c_2 = 1) scheme. The shock position is uneffected and the angle of attack is only slightly increased ($\Delta\alpha$ .01) as c_2 is increased from zero to one. The results also indicate that the solution for c_2 = 0.8 and 0.9 are virtually identical to the second-order (c_2 = 1) solution. The pressure distribution on the airfoil surface for the C_L = 0.95 cases given in Fig. 12. The two solutions are indistinguishable in this plot. These results indicate that the first-order accurate

TABLE 1. EFFECT OF c_2 AND Q_c ON SOLUTIONS FOR INVISCID FLOW OVER A RATE 2822 AIRFOIL AT $M_\infty = 0.725$

C_L	c_2	Q_c	C_D	α	X_s
0.9	0	1	0058	1.844	.65
0.9	0	.90	0058	1.853	.65
0.9	.8	.90	0060	1.830	.65
0.9	.8	.95	0060	1.829	.65
0.9	.9	.90	0060	1.827	.65
0.9	.9	.95	0060	1.827	.65
0.9	1.0	.90	0060	1.824	.65
.925	0	1	0069	1.904	.66
.925	.90	.90	0071	1.885	.66
.925	1.0	.90	0071	1.881	.66
.950	0	1	0082	1.960	.66
.950	.9	.9	0084	1.938	.66

version of the F-C scheme employed in the present method is surprisingly accurate suggesting that the first-order truncation error terms must be relatively small. Our experience with the present method is at variance with the results of Collyer and Lock (Ref. 18), obtained for a similar case with their partially-conservative P-C scheme. Their results showed a much larger effect of c_2, with the drag increasing by about twenty counts as c_2 increased from zero to one. The major discrepancy is between the two first-order solutions, with Collyer and Lock's solutions producing much lower drags. The reason for the poor performance of the Collyer and Lock first-order P-C method has not been ascertained.

The above results indicate that the first-order accurate version of the present method should be adequate for most purposes. However, there are some cases involving weak shock waves for which variations of c_2 produce more noticeable effects. In these cases weak shock waves near the leading edge were not adequately resolved with the first-order accurate version of the method. We found improved resolution could be obtained by either refining the mesh or by increasing c_2 toward one. A typical result illustrating this effect in a full viscous solution is given in Fig. 13. In

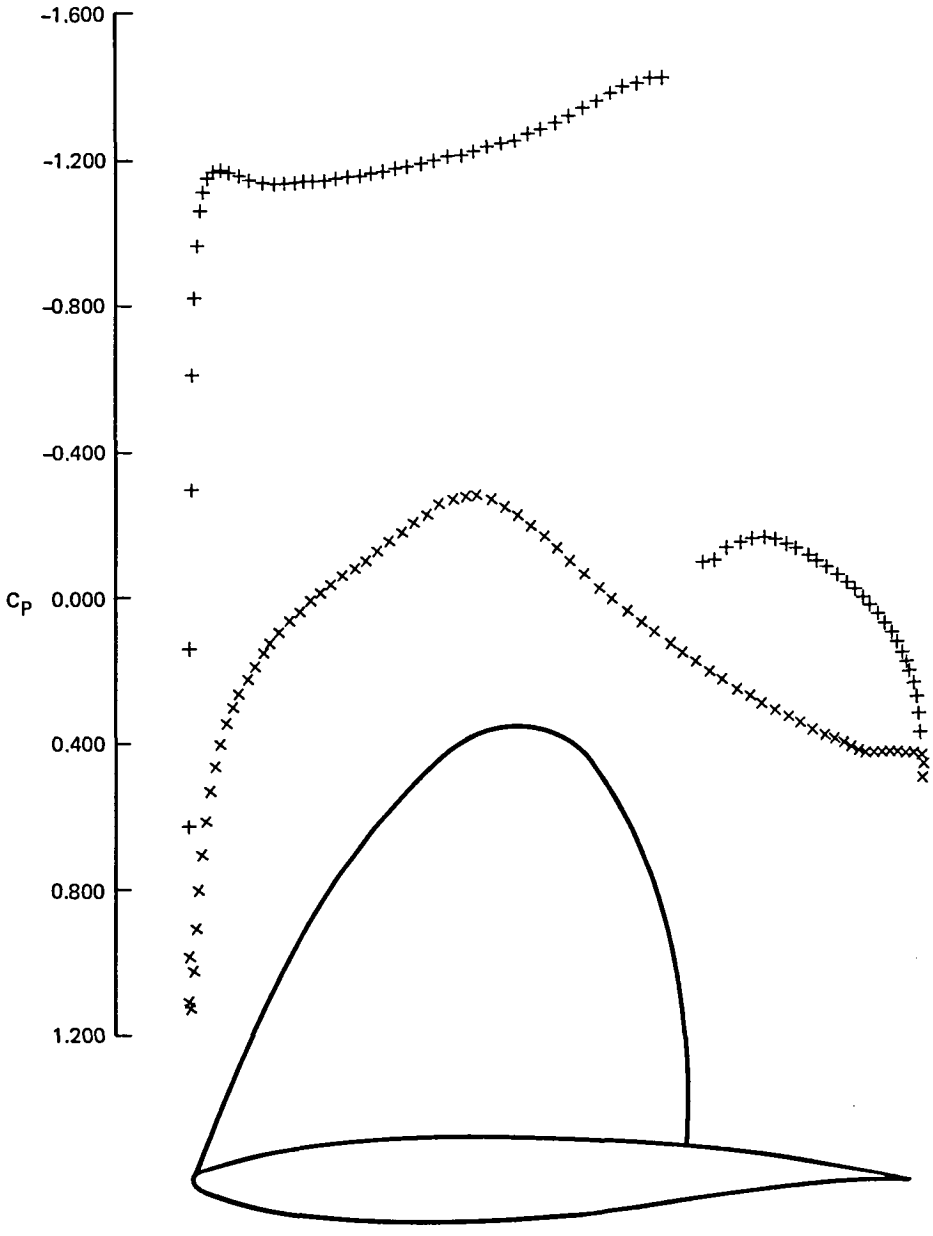

Figure 12 RAE 2822 – Inviscid Pressure Distribution at $M_\infty = 0.725$, $C_L = 0.95$, $c_2 = 0$ and $c_2 = 0.90$

this figure first and second-order accurate solutions for the surface-pressure distributions are compared for $M_\infty = 0.725$ and $C_L = 0.521$. This case involves two shock waves on the upper surface of the airfoil. The results indicate that the forward, weak shock wave is not adequately resolved by the first-order scheme on the (160 x 32) grid employed in the computation, but that good resolution is achieved with the second-order scheme. Note that, as is generally the case, the drag and angle of attack are only slightly affected by the choice of c_2.

The dotted line extending from the airfoil trailing edge in Figure 13 (and in all others C_p plots to follow) is the transformed "cut" ($\omega = 0$) location in the physical plane. The nearby solid curve is an approximation to the composite solution for the streamline from the trailing edge as determined from an itegration of the flow angle, $\beta = \beta_r + \beta_0$, along the "cut". The closeness of these two curves near the trailing edge is supportive of the approximations used in the evaluation of the wake-curvature terms.

The first-order scheme is less expensive to use and has been found to be generally adequate for most cases. Therefore, it is recommended for general use and has been employed in all solutions presented in this report. The second-order scheme is reserved for certain special cases requiring greater accuracy to resolve fine details of the flow field as in Fig. 13.

5.2 EFFECTS OF THE WAKE AND TRAILING EDGE INTERACTION

The computer code has been organized so that individual terms appearing in the viscous matching conditions can be selectively dropped from the computations. This option has been employed to generate a series of solutions that illustrate the importance of the individual terms in the matching conditions. Three cases have been carried out, corresponding to subcritical and supercritical flows over an RAE 2822 airfoil and to supercritical flow over a more heavily rear-loaded supercritical airfoil developed by the NASA (LaRC). For each case, a series of solutions have been obtained with each of the terms appearing in the matching conditions selectively dropped. Solutions for the drag, lift, and trailing edge pressure are summarized in Tables 2A and 2B. In these tables C_{DB} is the total drag, determined from integration of the pressure and skin friction over the airfoil surface, and C_{D_∞} is the profile drag determined from the wake momentum thickness far downstream (i.e., $C_{D_\infty} = 2\theta_\infty$). Profile drag is equal to the total drag less the wave drag and is due solely to

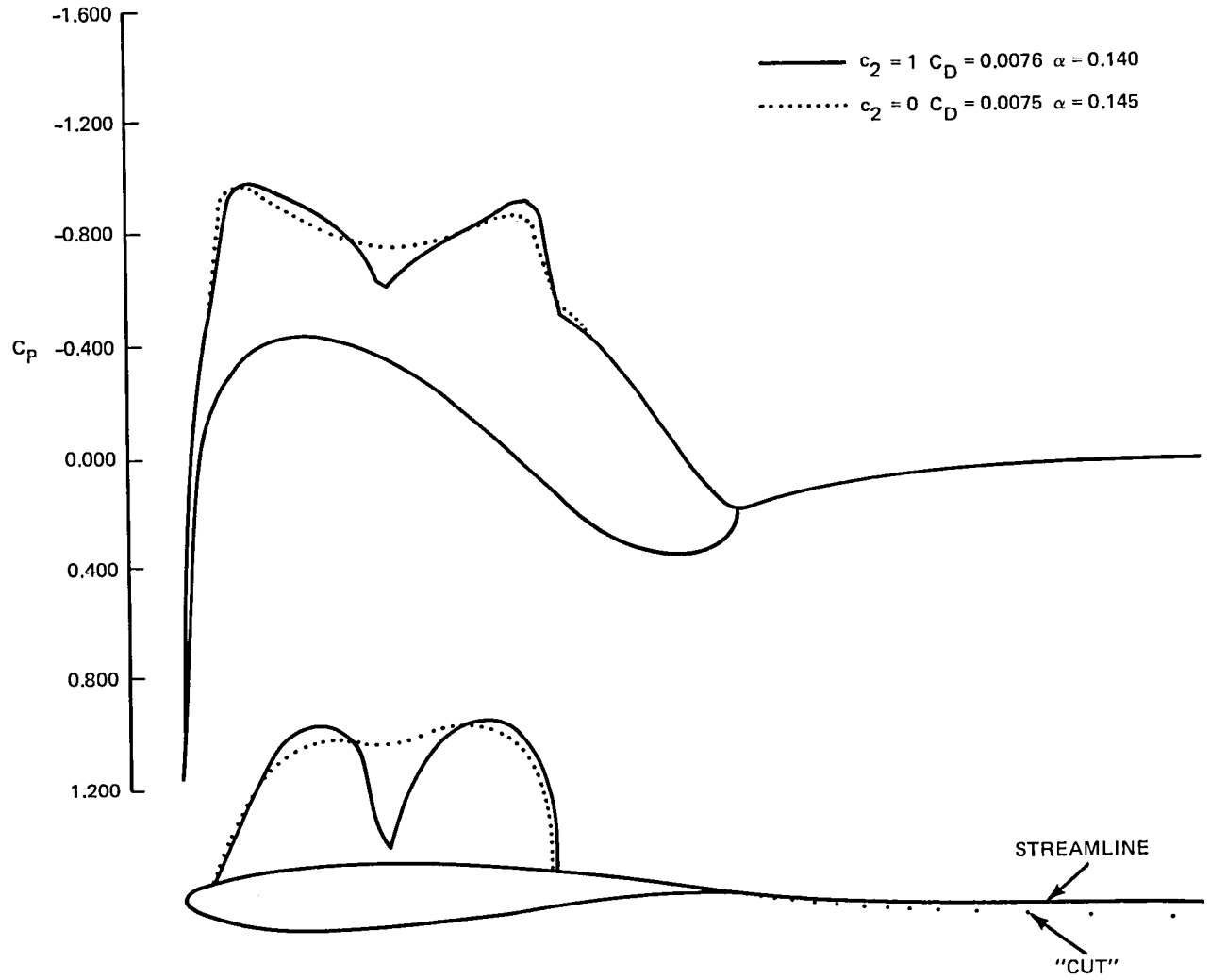

Figure 13 GK1 — Comparison of the First and Second Order Accurate Viscous Solutions at $M_\infty = 0.752$, $C_L = 0.521$, $R_e = 21.5 \times 10^6$ ($X_r = 0.10$)

momentum losses in the boundary layer. For subcritical flow, C_{D_∞} is equal to the total drag of airfoil and should be equal to C_{DB} as determined by surface integration. In general, however, these two evaluations of the drag will not be equal with the differences due both to, numerical errors in the solution of the governing equations and to approximations in the formulation of the viscous effects. The momentum drag (i.e., $2\theta_\infty$) seems to be relatively insensitive to the details of the numerical method and the formulation of the viscous theory, and is thought to be the more accurate prediction of drag in subcritical flows. In these cases the difference between profile and integrated drag is a useful measure of the overall accuracy of the theoretical model.

The results in the tables include solutions for (A) the inviscid theory, (B) the full viscous theory, (C) the full viscous theory less the trailing-edge corrections, (D) less the wake-curvature term, and (E) less the wake-thickness terms. In the latter solution the wake is modeled as a constant thickness extension of the displacement surface on the airfoil surface. We have also carried out solutions neglecting the trailing-edge corrections and both the wake curvature and thickness terms. This version of the theory, (F), includes only the displacement effect on the airfoil surface and is, therefore, equivalent to the formulation employed in the BGKJ (Refs. 12 & 15) method and its derivatives (Refs. 13 & 14). For the two supercritical cases studied using this latter formulation, we have also obtained solutions with the N-C version of our method (labeled (G) in the Table 2B). In addition, for the two RAE 2822 cases considered in Tables 2A, B, we have also included available results from the RAE non-conservative method (Ref. 17). The RAE method accounts for both wake-thickness and wake-curvature but not trailing-edge interaction effects.

The results for the subcritical RAE 2822 case are listed in Table 2A. Comparisons of the inviscid (A) and full viscous (B) solutions illustrate the large effect of the boundary layer on lift. Even for this subcritical case, the presence of the boundary layer causes a nearly 1/3 decrease in lift. The results given in lines (C), (D), and (E) illustrate the effect of the individual terms in the matching conditions. Comparisons of the results in lines (A)-(E) indicate that the largest effect is caused by the displacement thickness on the airfoil surface with the other terms also producing significant effects. The influence of wake thickness on drag and lift and of wake curvatures on lift are the most pronounced of these secondary influences. The effect of wake thickness on lift was unanticipated since we would expect predominately symmetric effects from this source. However, on reflection, this behavior is not surprising. The neglect of the wake-thickness term is seen to lead to an increase in pressure at the trailing edge which in turn, induces a significant increase in boundary-layer thickness near the trailing edge. The increase is largest on the upper surface because of the larger initial boundary-layer thickness on this surface. It is this differential increase in boundary-layer thickness caused by the neglect of the wake-thickness term that leads to the observed lift reduction. We also call attention to the insensitivity of the momentum drag, C_{D_∞}, to differences in the theoretical model and to the good agreement between the two evaluations of drag in the full viscous solution (B). The good agreement evident

TABLE 2A - RAE 2822 AIRFOIL AT $M_\infty = 0.676$ $\alpha = 1.06^\circ$

$R_e = 5.7 \times 10^6$ $X_T = 0.11$

Mode	Theoretical Model	C_D	C_{D_∞}	C_L	C_{PTE}
(A)	Inviscid	0	0	0.571	0.438
(B)	Full Viscous	0.0084	0.0083	0.431	0.234
(C)	(B) Less TE Corrections	0.0080	0.0083	0.416	0.234
(D)	(B) Less Wake Curvature	0.0081	0.0083	0.454	0.234
(E)	(B) Less Wake Thickness	0.0069	0.0082	0.398	0.289
(F)	(B) Less TE Corrections, Wake Curvature & Thickness	0.0064	0.0082	0.399	0.278
(C')	RAE (NC) (Ref 17)	0.0081	0.0083	0.430 (0.420)	0.226

in this case is an encouraging indication of the overall accuracy of the present method. The underprediction of the integrated drag and the poor agreement with C_{D_∞} when the wake-thickness terms are suppressed (E), are indications of the importance of these terms. The comparisons in Table 2A indicate that the formulation based on airfoil displacement thickness only, underpredicts the drag by 25% and the lift by 7% in this case.

The results of the N-C RAE method of Ref. 17 (C'), which is equivalent to the formulation employed in case (C) of the present method, are in good agreement. Two values of the lift coefficient are given for the RAE method. The higher value results from a version of their method that employs considerable numerical smoothing of the wake curvature terms near the trailing edge. The smaller value, obtained with less smoothing, is in better agreement with the results of case (C) of the present method. It was reported in Ref. 17 that convergence difficulties were experienced in this latter version and its use was not recommended. This difficulty is likely related to the neglect of trailing edge interaction effects in their formulation.

A similar series of calculations were carried out for the same airfoil at a higher free-stream mach number, resulting in a supercritical flow. The results are listed in Table 2B. In this case the integrated drag includes wave drag and so is no longer equal to the momentum drag, C_{D_∞}. The difference between C_{DB} and C_{D_∞} is a relatively accurate measure of the wave drag in the full viscous solution (case (B)), but not in the other cases because of the inadequacies of the viscous formulation clearly evident in the subcritical results (Table 2A). The neglect of wake and trailing edge interaction effects in this supercritical case leads to a 35% underprediction of the drag coefficient (case (F)) compared to the full viscous solution. We have also repeated case (F) with the N-C formulation (Line (G) in Table 2B). The N-C scheme leads to a weaker, more forward shock wave but to a higher drag. This extra drag arises from a spurious mass generation at the shock wave caused by N-C differencing. This spurious drag increase is also evident in the comparison of the RAE results (case (C')) with the present, equivalent formulation using F-C differencing (case (C)).

The solutions for the pressure distribution on the airfoil surface are given in Fig. 14. Included in the figure are the inviscid solution (A), the full viscous solution (B), and the viscous solution less the trailing correction and both wake terms (F). Both F-C and N-C calculations of the latter case are included. These results illustrate the very large effect of the boundary layer on the flow field in supercritical conditions even at the relatively large Reynolds number of the computations. The boundary layer drives the shock wave forward from X = 0.80 to X = 0.55, significantly reduces the pressure level on the upper surface, and increases it on the lower surface of the airfoil. These effects produce a reduction in the lift coefficient by nearly a factor of two. The neglect of the wake and trailing-edge contributions to the matching conditions is seen to drive the shock wave forward by about 5% and to reduce the lift by 10% and drag by 35% below the full viscous solution (see Table 2B). The switch to a N-C scheme is seen to drive the shock wave even further forward.

The details of the pressure distribution near the trailing edge for the full viscous solution at the higher Mach number, $M_\infty = 0.725$, is plotted on an expanded scale in Fig. 15. Included in this figure are the "composite" and "outer" solutions computed from the full viscous theory. The composite solution contains contributions from the "outer" and "inner" solution as given by Eq. (66) which account for the

TABLE 2B - RAE 2822 AIRFOIL AT $M_\infty = 0.725$, $\alpha = 2.3^o$, $R_e = 6.5 \times 10^6$ $X_T = 0.03$

Mode	Theoretical Model	C_D	C_{D_∞}	C_L	$C_{P_{TE}}$
(A)	Inviscid	-	-	1.300	0.5265
(B)	Full Viscous	0.0110	0.0098	0.726	0.222
(C)	(B) Less TE Corrrections	0.0101	0.0096	0.700	0.227
(D)	(B) Less Wake Curvature	0.0112	0.0100	0.758	0.224
(E)	(B) Less Wake Thickness	0.0080	0.0093	0.661	0.276
(F)	(B) Less TE Corrections, Wake Curvature & Thickness	0.0072	0.0043	0.658	0.271
(G)	(F) With Nonconservative Differencing	0.0081	0.0092	0.648	0.269
(C')	RAE (NC)[5]	0.0119	-	0.699	0.219

pressure variations across the boundary layer and wake. The outer solution clearly exhibits the wake pressure jump imposed as part of the viscous matching conditions. The pressure jump is largest at the trailing edge and rapidly decays away from the trailing edge both in the wake and on the airfoil surface. The relatively large jump in pressure at the trailing edge (ΔC_p 0.2) is indicative of the importance of normal pressure gradients near trailing edges. The crossing of the outer solution on the airfoil is a typical property of the viscous wake solution which clearly distinguishes it from jet-flap solutions with positive blowing coefficient.

The RAE 2822 is an airfoil with moderate rear loading. A similar series of calculations have also been carried out for a more highly rear-loaded supercritical airfoil developed by the NASA-Langley Research Center. The calculations for this case were carried out for a free-stream Mach number of $M_\infty = 0.768$ and an angle of attack of $\alpha = -0.151$, resulting in a lift coefficient in the full viscous solution of $C_L = 0.832$.

The solutions for this case are listed in Table 3. The airfoil has a nonzero trailing-edge thickness which requires an estimate for the base-drag contribution to C_{DB}. This contribution amounted to 7 counts of drag for all cases considered in Table 3.

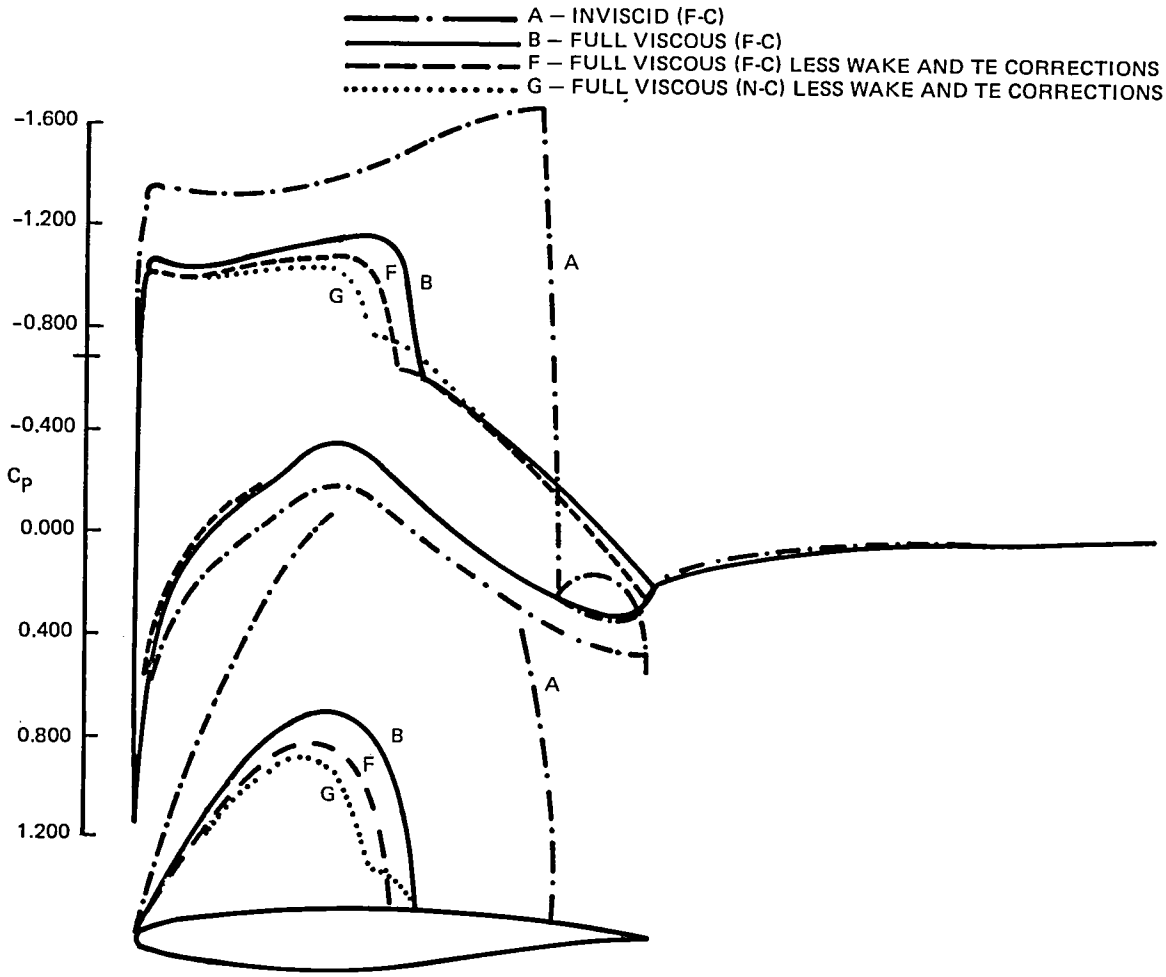

Figure 14 RAE 2822 – Effect of the Wake and Trailing Edge Corrections on the Theoretical Pressure Distribution at $M_\infty = 0.725$, $\alpha = 2.3^\circ$, $R_e = 6.5 \times 10^6$ ($X_T = 0.03$)

The shock position in the inviscid solution at this incidence and Mach number appears to be downstream of the trailing edge and, because of this, the inviscid solution could not be computed with the circle plane code used in the present study. The viscous solution could be determined without difficulty. The inclusion of the boundary layer in the viscous solutions drove the shock wave forward to 73% chord, again demonstrating the very large effect of the boundary layer on the flow field at transonic speeds.

The results in Table 3 indicate that the trailing-edge correction and the variation of profile drag with the theoretical model are much larger than in previous cases. We also note that the neglect of trailing-edge correction and the wake terms

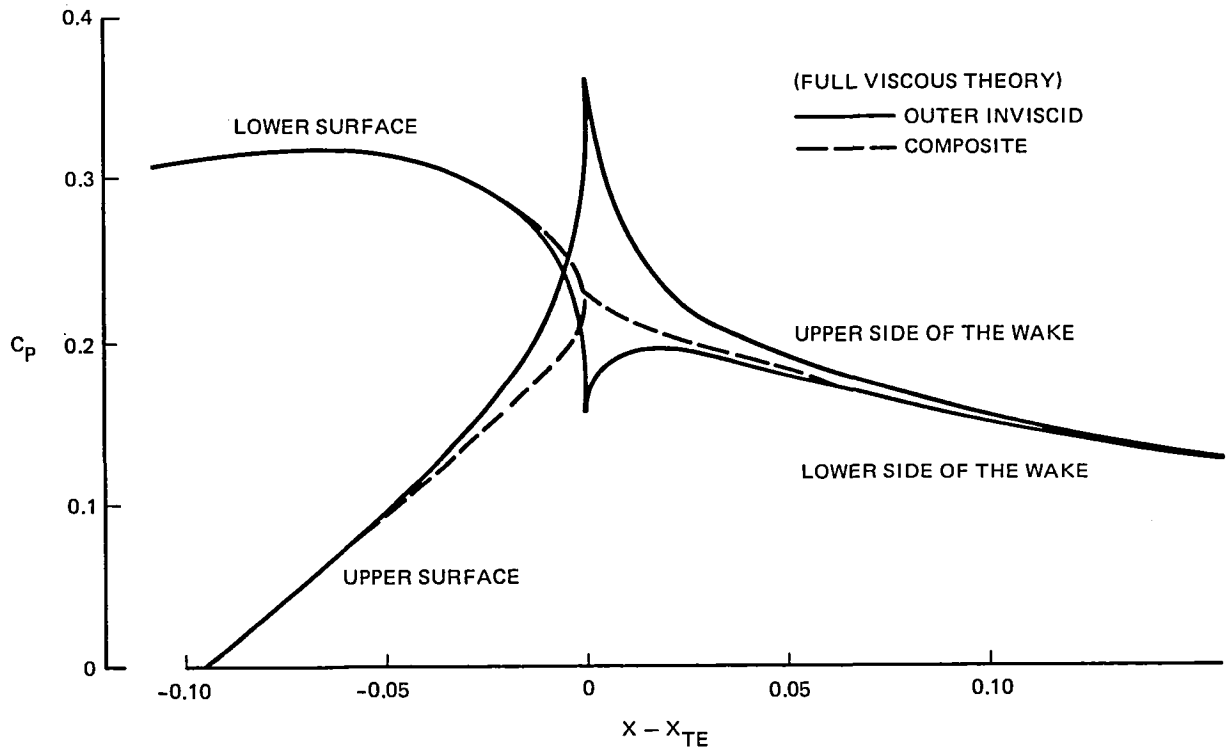

Figure 15 RAE 2822 — Details of the Pressure Distribution Near the Trailing Edge at $M_\infty = 0.725, \alpha = 2.3^\circ, R_e = 6.5 \times 10^6$ ($X_T = 0.03$)

(F) leads to a 30% an underprediction of drag and the use of a N-C formulation leads to a partially compensating increase of drag of about 10%.

5.3 THEORETICAL PREDICTION OF PROFILE DRAG AT SUBCRITICAL CONDITIONS

At low Mach number subcritical conditions, the total drag of an airfoil is equal to the profile drag given by the sum of skin friction and pressure drag. As discussed previously, the profile drag can be evaluated either by integrating the surface pressure and shear-stress distributions or from momentum considerations, by $C_{DB} = 2\theta_\infty$. The total drag can also be estimated from the Squire-Young approximation based on momentum thickness at the trailing edge. The difference between the integrated drag, C_{DB}, and the more accurate momentum drag, C_{D_∞}, is a useful measure of the error of the theory. In Table 4 we compare the theoretical results for the integrated and momentum drags for several airfoils at a variety of subcritical flow conditions. In this table C_{DB} is the total integrated drag, C_D is the integrated drag less the base drag, C_{D_∞} is momentum drag evaluated from $C_{D_\infty} = 2\theta_\infty$ and C_{DSY} is

total drag evaluated from the Squire-Young formula. The results in the table also include experimental data based on wake-rake measurements (Refs. 70-73).

TABLE 3 ADVANCED SUPERCRITICAL AIRFOIL AT $M_\infty = 0.768$ $\alpha = -0.151^0$

$R_e = 7.7 \times 10^6$ $X_T = 0.28$

Mode	Theoretical Model	C_{DB}	C_{D_∞}	C_L	C_{PTE}
(A)	Inviscid	NOT AVAILABLE			
(B)	Full viscous	0.0122	0.0082	0.852	0.137
(C)	(B) Less TE corrections	0.0097	0.0078	0.808	0.156
(D)	(B) Less wake curvature	0.0131	0.0091	0.871	0.120
(E)	(B) Less wake thickness	0.0105	0.0079	0.835	0.155
(F)	(B) Less TE corrections, wake curvature & thickness	0.0088	0.0079	0.821	0.168
(G)	(F) With nonconservative differencing	0.0098	0.0074	0.768	0.155

The agreement between the integrated and momentum drags for the RAE 2822, GK1 and the NASA LaRC airfoils is strong evidence that the present method produces accurate prediction of the absolute level of drag at subcritical conditions. The difference between C_D and C_{DB} for the NASA airfoil arises from a thrust on the finite base of this airfoil. The agreement between the integrated and momentum drags is noticeably poorer for the NACA 0012 airfoil. This airfoil has a significant base ($\Delta y/c = 0.0026$) and a relatively large trailing-edge angle of 16^0. These geometric features make the solution for the integrated drag very sensitive to the pressure levels near the trailing edge. The under-prediction of the integrated drag in this case is very likely caused by neglect of strong-interaction effects associated with the trailing-edge angle. The ratios of trailing-edge thickness to boundary-layer momentum thickness ($\Delta y/\theta_{TE}$) is 1.2 for the NASA airfoil and 0.4 for the NACA 0012 cases in Table 4, indicating that the approximations used for the base pressure is adequate for these cases. The theoretical results for the Squire-Young evaluation of the drag is nearly identical to the drag based on far-field momentum thickness in all cases considered in the table. The momentum drag, C_{D_∞}, which is thought to be the

more accurate theoretical prediction, is also in very good agreement with the data from the RAE, Langely, and Ohio State University wind tunnels. The drag from the NAE tunnel seems to be consistently high by about 10 counts compared to the present theory. The good agreement observed in other cases (compare, in particular, the Ohio State and NAE data for the NACA 0012 airfoil) suggests this is due to a consistent error in the NAE measurements.

TABLE 4 PROFILE DRAG RESULTS

Case	Present Theory				Experiment	
	C_D	C_{DB}	C_{D_∞}	$C_{D_{SY}}$	$C_{D\ Exp}$	Source
RAE 2822 M_∞=0.676 C_L=0.576 R_e=5.7 X 10^6 X_T=0.11	-	0.0087	0.0085	0.0085	0.0085	RAE (Ref. 70)
RAE 2822 M_∞=0.676 C_L= -0.121 R_e=5.7 X 10^6 X_T=0.11	-	0.0081	0.0082	0.0083	0.0079	RAE (Ref. 70)
GKI M_∞=0.511 C_L=0.431 R_e=21.5 X 10^6 X_T=0.10	-	0.0063	0.0064	0.0064	0.0078	NAE (Ref. 73)
GKI M_∞=0.622 C_L=0.458 R_e=21.5 X 10^6 X_T=0.10	-	0.0065	0.0066	0.0066	0.0070	NAE (Ref. 73)
NASA LRC M = 0.78 C_L=0.42 R_e=7.7 X 10^6 X_T=0.28	0.0079	0.0070	0.0070	0.0069	0.0072	NASA LRC
NACA 0012 M_∞=0.575 C_L=0.006 R_e=4.7 X 10^6 X_T=0.10	0.0079	0.0072	0.0082	0.0082	0.0081	Ohio State Univ. (Ref. 72)
NACA 0012 M_∞=0.693 C_L=0.017 R_e=22.1 X 10^6 X_T=0.05	0.0065	0.0057	0.0067	0.0068	0.0078	NAE (Ref. 71)

In Table 5 the profile drag prediction of the full viscous theory for the NACA 0012 airfoil tested at Ohio State University are compared with parallel wake solutions obtained with the present computer code and with the predictions of the BGKJ and Carlson methods presented in Ref. (72). As discussed above, the momentum drag from the full viscous solution is in good agreement with the experimental data. The integrated drag shows a significant error for reasons previously mentioned. The theoretical pressure distribution is compared with experimental data in Fig. 16. The agreement is good, except near the trailing edge, where the theory indicates a more positive pressure. This is consistent with the error in integrated drag.

TABLE 5 NACA 0012 AT ZERO LIFT

$M=0.575 \quad R_e=4.68 \times 10^6 \quad X_T=0.10$

Theory	C_D	C_{DB}	C_{D_∞}	$C_{D_{SY}}$
Present - Full viscous	0.0079	0.0072	0.0082	0.0082
Present - Parallel wake	0.0063	0.0054	0.0081	0.0081
BGKJ (Ref. 72)	0.0047	0.0036*	-	-
Carlson (Ref. 72)	0.0051	0.0042*	-	-
Experiment (Ref. 72)	0.0081			

(* Obtained by subtracting $\Delta C_{P_B} = 0.0009$ from C_D)

Neglect of the wake-thickness term leads to substantial increase in the error in integrated drag but does not affect the solution for momentum drag. A significant part of the discrepancy between the two evaluations of drag is due to the contribution of the base, which in this case amounts to seven counts of thrust. We note the very large underprediction of the drag by both the BGKJ and Carlson methods. With the base drag included, these methods are seen to underpredict the drag by a

factor of two. The base-drag contribution was not included in the original solutions presented in Ref. (72). We have corrected these solutions for base drag using the base-drag increments determined from our parallel-wake solution in order to provide a uniform basis for comparison.

The results in this section demonstrated that the absolute value of the profile drag can be adequately determined from the integrated drag of the full viscous solution. This was demonstrated in Table 4 for airfoils with small trailing edge angles. The trailing edge angles of the GK1. NASA-LaRC RAE 2822, and NACA 0012 airfoil are 0, 3.87, 8.67, 15.96 degrees, respectively. This differs from the conclusion reached by Smith and Cebeci (Ref. 74) in a study of boundary-layer methods for predicting profile drag. In their study they concluded that profile drag predictions based on integrated shear and pressures were inadequate, and they recommend exclusive use of the Squire-Young formula. The present study indicated that Smith and Cebeci's difficulties with integrated drag were due entirely to the neglect of the wake-thickness terms in their boundary-layer model. Calculation of the Joukowski profile with the present method showed relatively good agreement between the integrated and momentum drags. The results are summarized in Table 6.

We note that the present results for integrated drag obtained with the wake-thickness terms neglected agree well with the results of Ref. (74) and that both methods underpredict the drag by about a factor of two for the 30% thick airfoil.

The results in this section demonstrated the importance of the base drag contribution for certain airfoils with open trailing edges. The contribution of the base drag was an important element in obtaining favorable agreement between theory and experiment of the NASA LaRC airfoil. The poorer agreement obtained the the NACA 0012 is indicative of the importance of strong interaction effects associated with the large trailing-edge angle of this airfoil. Further improvements in the prediction of profile drag of airfoils with sizeable trailing edge angles can be achieved by incorporating an appropriate strong interaction solution into the theoretical formulation.

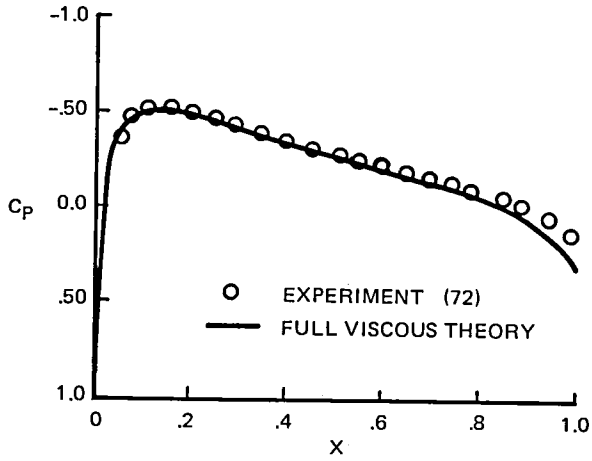

Figure 16 NACA 0012 - Pressure Distribution at Zero Lift at $M_\infty = 0.575$, $Re = 4.68 \times 10^6 (X_T = 0.10)$

TABLE 6 PROFILE DRAG FOR JOUKOWSKI AIRFOILS AT ZERO INCIDENCE

$M_\infty = 0.05 \quad R_e = 10 \times 10^6 \quad X_T = 0.10$

	Present Theory			Theory of Ref. (73)		
t/c	c_f	C_D	$C_{D_{SY}}$	c_f	C_D	$C_{D_{SY}}$
0.10	0.0058	0.0064 (0.0063)	0.0066	0.0057	0.0062	0.0065
0.15	0.0060	0.0070 (0.0067)	0.0074	0.0058	0.0065	0.0072
0.20	0.0061	0.0075 (0.0069)	0.0081	0.0060	0.0067	0.0080
0.25	0.0062	0.0082 (0.0069)	0.0092	0.0061	0.0065	0.0090
0.30	0.0063	0.0091 (0.0063)	0.0105	0.0062	0.0054	0.0102

( ) Denotes results obtained with parallel wake formulation

5.4 COMPARISONS OF TRANSONIC RESULTS WITH EXPERIMENTAL DATA

In this section we present comparisons between theoretical computations and wind-tunnel data for the GK1 the NASA LaRC, and the RAE 2822 airfoils. The comparisons considered in this section include a number of cases of supercritical flow with shock waves. The theoretical method described in this study does not provide for a proper asymptotic description of the shock-wave boundary-layer interaction process. A rational analysis of shock-wave boundary-layer interactions in trubulent flow should account for the penetration of the shock wave into the boundary layer and normal pressure gradients across the boundary layer. In the present study, normal pressure-gradient effects are only accounted for near the trailing edge. At shock waves, the present method reduces to a standard, free-interaction type analysis employing a Prandtl boundary-layer description of the shear layer. This theoretical scheme does not permit shock waves, with the attendant discontinuous pressure distribution, to impinge on the boundary layer. A discontinuity in pressure or edge velocity in the present method would lead to a delta function behavior in the surface source velocity in the viscous matching conditions (since $v_\sigma \approx dU_e/ds$) and to a breakdown of the present method. The results of extensive computations suggest this does not occur in the present method. Instead, interaction between the inviscid and boundary-layer regions leads to an adjustment in the solution that avoids this type of singular breakdown. Within the present method, the behavior near shock wave appears to be as sketched in Fig. 17.

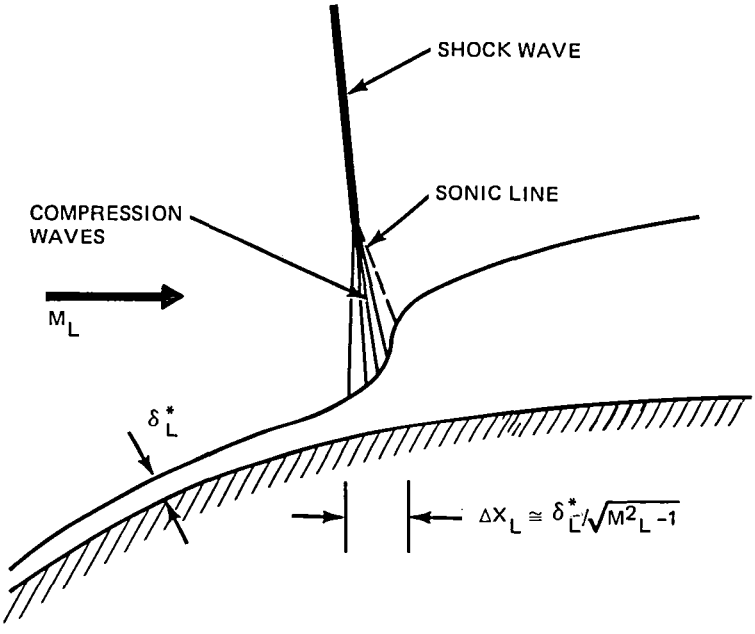

Figure 17 Schematic of a Shock-Wave Boundary Layer Interaction in the Present Formulation

In this model, the approach of the shock wave to the boundary layer causes a rapid buildup of displacement thickness which, in turn, generates a narrow band of compression waves. These compressions act to spread the shock wave and prevent a discontinuity from impinging on the boundary layer. The interaction spreads the pressure jump over a distance, $\Delta X \approx \delta_L^* / \sqrt{M_L - 1}$, where δ_L and M_L are the displacement thickness and local Mach number just upstream of the shock wave. For the cases considered in the present study, the interaction length is typically in the order of $\Delta X \approx 0.005$. Since the minimum grid spacing on the fine mesh is about twice this value, it is clear that the present computations do not resolve the flow near the shock wave. Nevertheless, results presented in this section show that the present method does lead to reasonable predictions of shock wave/boundary layer interactions. It has been known for some time, from experiments on airfoils, that a turbulent boundary layer reduces the pressure rise across a shock wave to about half of that predicted by the shock conditions for a normal shock wave. This behavior is predicted reasonability well in the present method and, in addition, also gives a good overall prediction the pressure distribution near the shock wave.

GK1 Airfoil. - The first group of results are for the GK1 supercritical airfoil. the airfoil is 11.5% thick, has a cusped trailing edge, and a moderate degree of aft camber. The data are from tests at the NAE transonic wind tunnel at Ottawa (Ref. 73) at a Reynolds number of 21.5 million with the tunnel walls set at 20.5% porosity. The airfoil was aerodynamically smooth and was tested with natural transition. The location of the transition point was not determined in the experiments. The calculations were carried out with transition fixed at 10% chord which appears to be a reasonable estimate, considering the high Reynolds number of the test. The theoretical solutions were found to be insensitive to small changes in the transition location. Recent studies (Ref. 75) have indicated the presence of significant wall interference in the NAE wind tunnel. The studies indicate the need for both downwash and blockage corrections to the angle of attack and free-stream Mach number with the corrections varying with both free-system Mach number and lift coefficient. Unfortunately, corrections were not yet available for the data considered in this section. Therefore, in the present comparison, we avoid the need for angle of attack correction by comparing theory and experiment at the same value of the lift coefficient. Small Mach number shifts are applied to the data to obtain agreement in the shock positions. The quantity, α_G, appearing in the Figure is the geometric angle of attack of the airfoil in the experiment.

The comparison of the surface pressure distribution for two subcritical and two supercritical cases are given in Figs. 18 to 21. We note the good agreement of the pressure distribution near the trailing edge with experiment and the very good predictions of the pressure levels behind the shock wave. The Mach number shift of $\Delta M_\infty = 0.008$ applied to the data of Fig. 21 is consistent with levels of the blockage correction predicted in Ref. 75. The experimental drags are high compared to the theoretical value in all cases with the largest discrepancy arising in the $C_L = 0.821$ case. The difference in this case is surprisingly high considering the relatively close agreement of the pressure distribution. as discussed previously, the differences in drag seem to be due to experimental error. Some evidence for this was presented in Ref. 76.

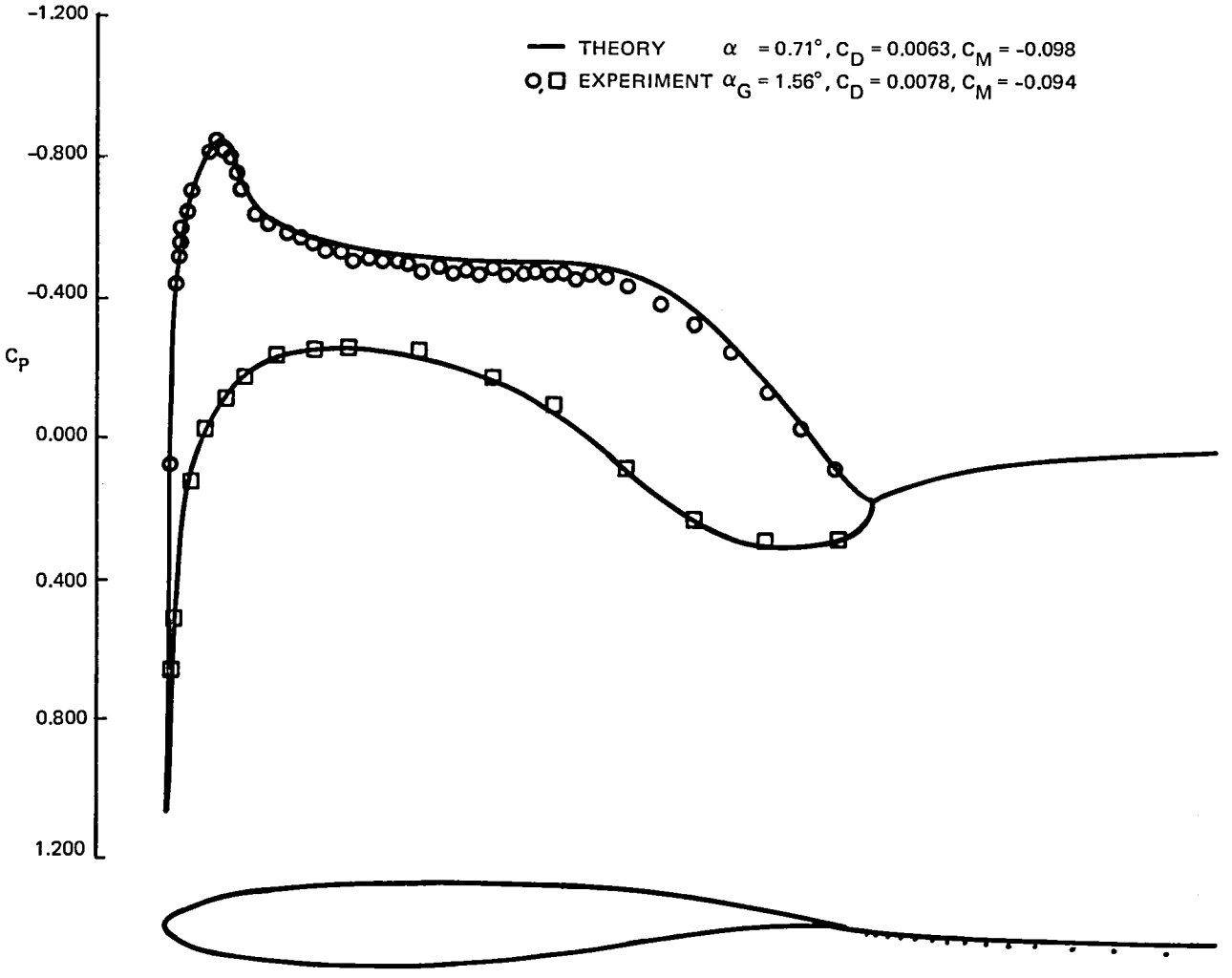

Figure 18 GK 1 — Pressure Distribution at $M_\infty = 0.511$, $C_L = 0.431$, $R_e = 21.5 \times 10^6$ ($X_T = 0.10$)

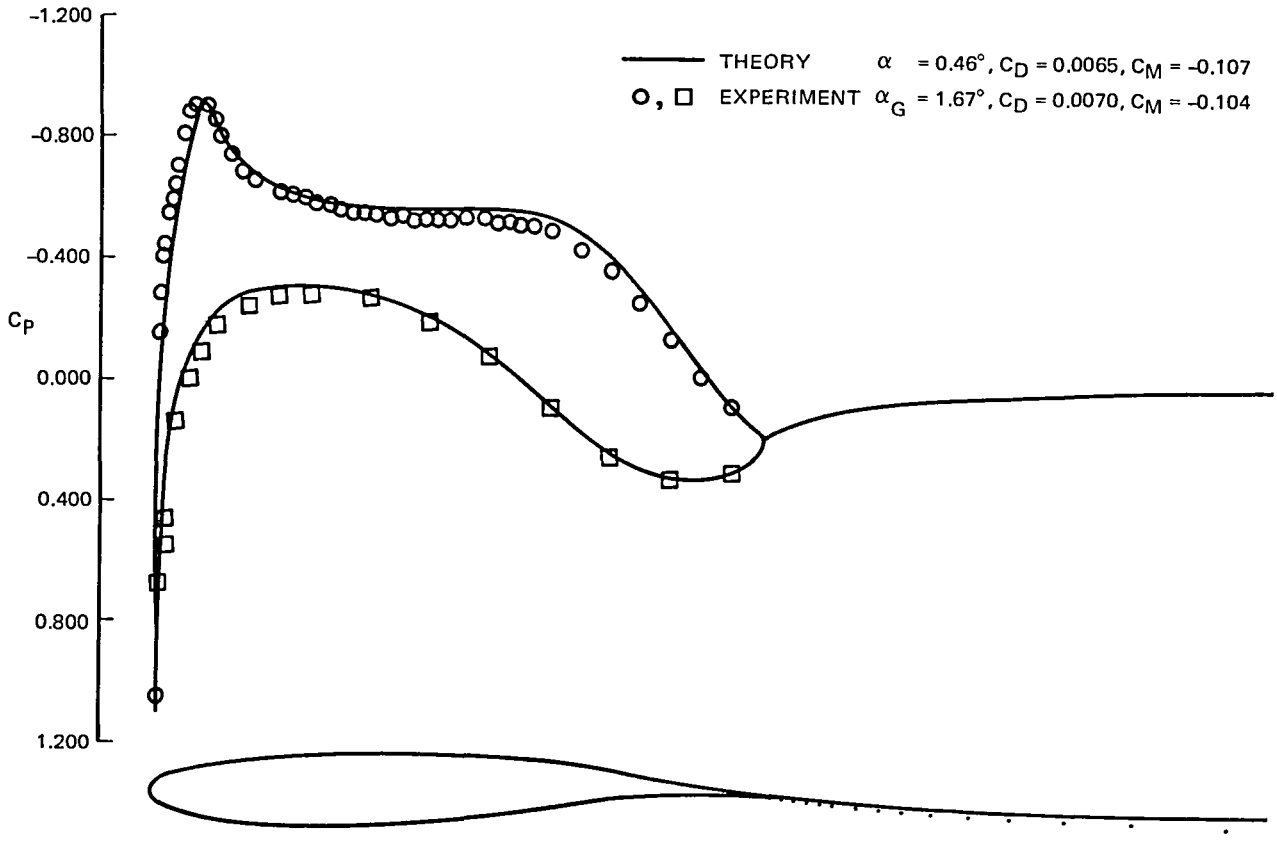

Figure 19 GK1 — Pressure Distribution at $M_\infty = 0.622$, $C_L = 0.442$, $R_e = 21.5$ ($X_T = 0.10$)

The solution for the drag polar is compared with experiment and with solutions to the Navier-Strokes equations* in Fig. 22. The theoretical solutions were obtained with a small Mach number shift of M = -0.005. The present solutions give a reasonable prediction of the overall shape of the drag polar but the level of the data is about 15% higher than the computation. The poor agreement of the Navier-Strokes solutions with both the data and the present computations is most likely due to poor spatial resolution since only about 50 points were employed on the airfoil in the calculation.

NASA-La RC Supercritical Airfoil. - This airfoil is a 10% thick, heavily rear-loaded, supercritical airfoil with a trailing-edge angle of 3.87° that was designed and tested at the NASA LaRC. The airfoil was tested in the 8 foot transonic pressure tunnel at a Reynolds number Re = 7.7 X 10^6 and a nominal Mach number of M_∞ = 0.78. Transition was fixed with roughness strip at 28% chord.

* Unpublished results supplied by Dr. G. S. Deiwert of NASA Ames Research Center.

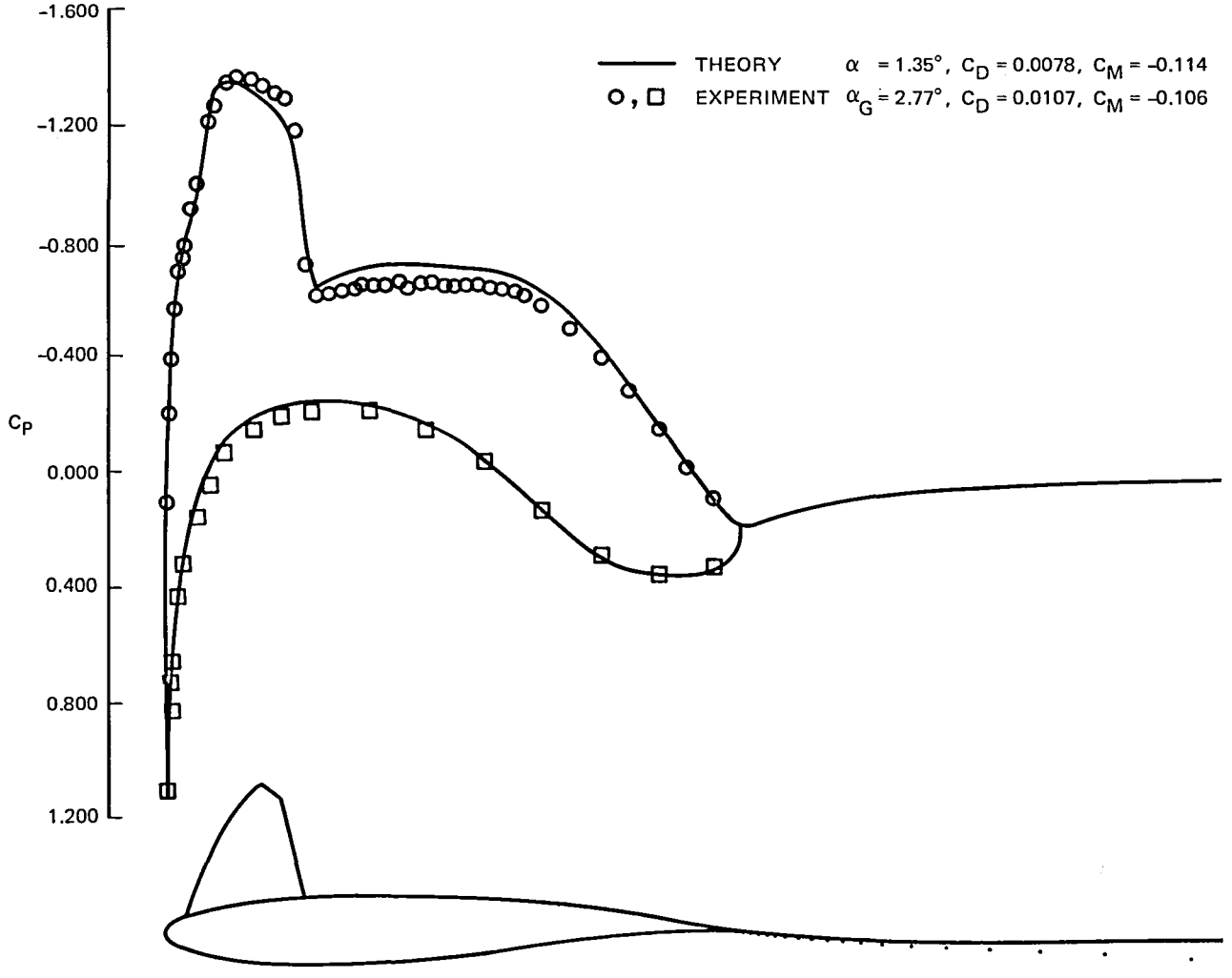

Figure 20 GK1 — Pressure Distribution at M_∞ = 0.699, C_L = 0.669, R_e = 21.5 x 10^6 (X_T = 0.10)

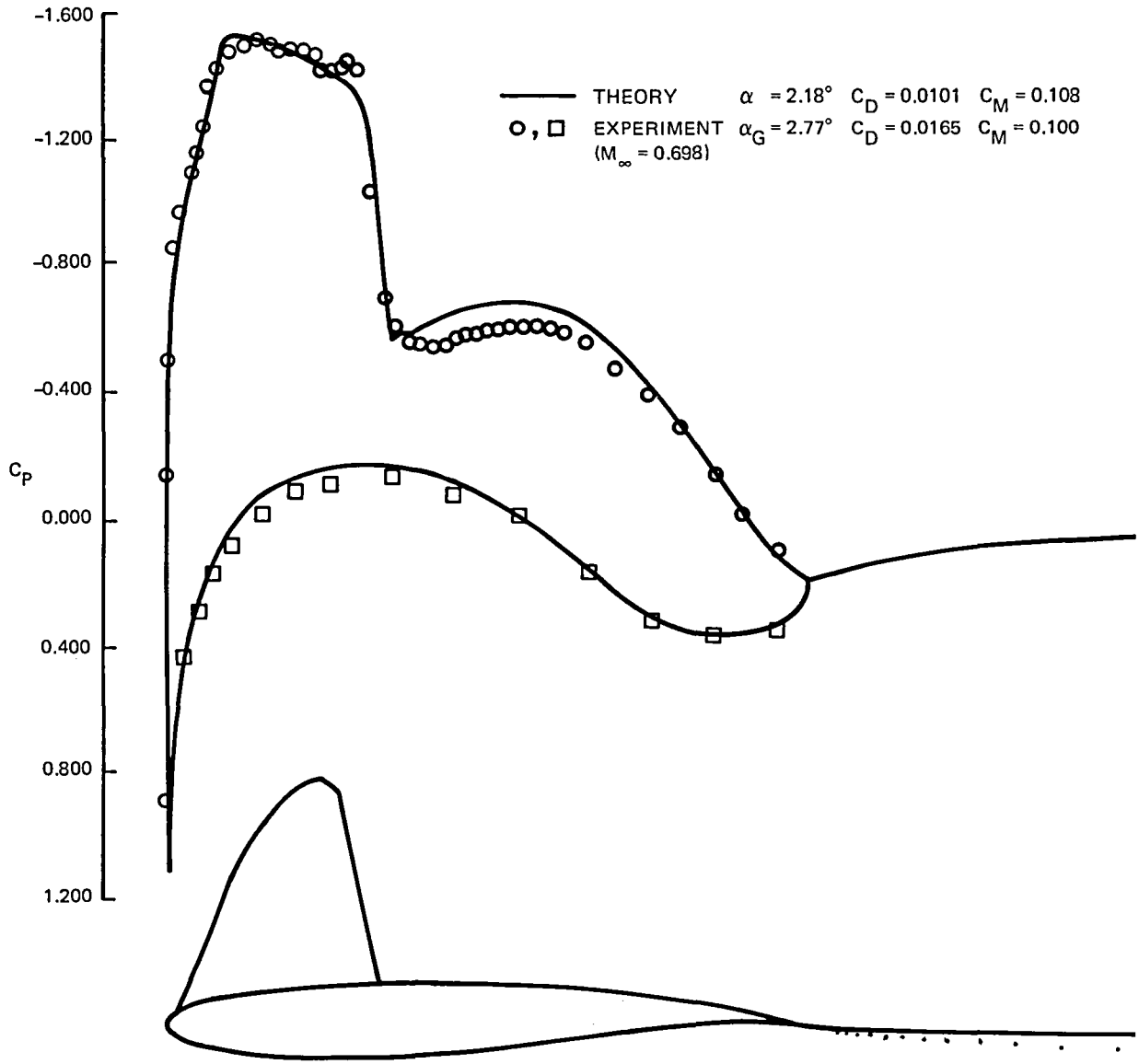

Figure 21 GK1 – Pressure Distribution at $M_\infty = 0.691$, $C_L = 0.821$, $R_e = 21.5 \times 10^6$, ($X_T = 0.10$)

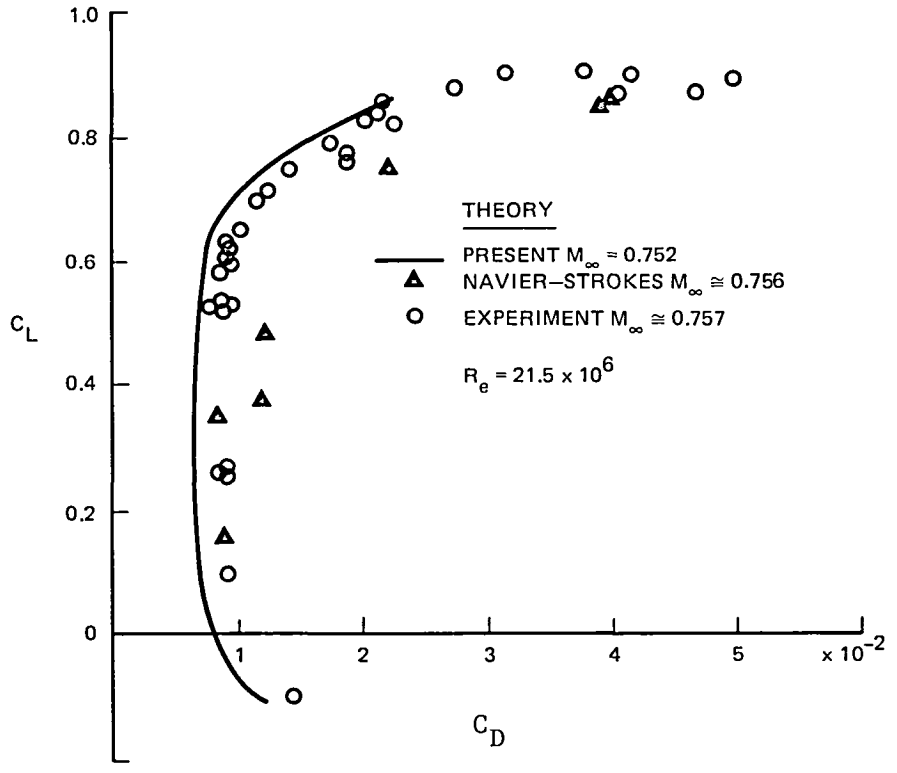

Figure 22 GK1 — Drag Polar at M = 0.752, $R_e = 21.5 \times 10^6$, ($X_T = 0.10$)

This tunnel is known to be subject to relatively large tunnel-wall interference effects, but, unfortunately, wall corrections have not been determined. We applied a blockage correction of $\Delta M_\infty = -0.012$ to improve the overall agreement of shock position.

The calculations for the drag polar are compared with wind-tunnel data in Fig. 23. Theoretical solutions from the full viscous theory are presented along with solutions obtained with the wake and trailing-edge correction terms deleted from the matching conditions. In the latter case solutions are presented for both F-C and N-C difference schemes. The results of the full viscous theory show good agreement with experiment over a wide range of lift coefficients. The results show that neglect of the wake and trailing-edge terms leads to noticeable underpredictions of drag and that N-C differencing leads to a substantial overprediction of drag when shock waves are present.

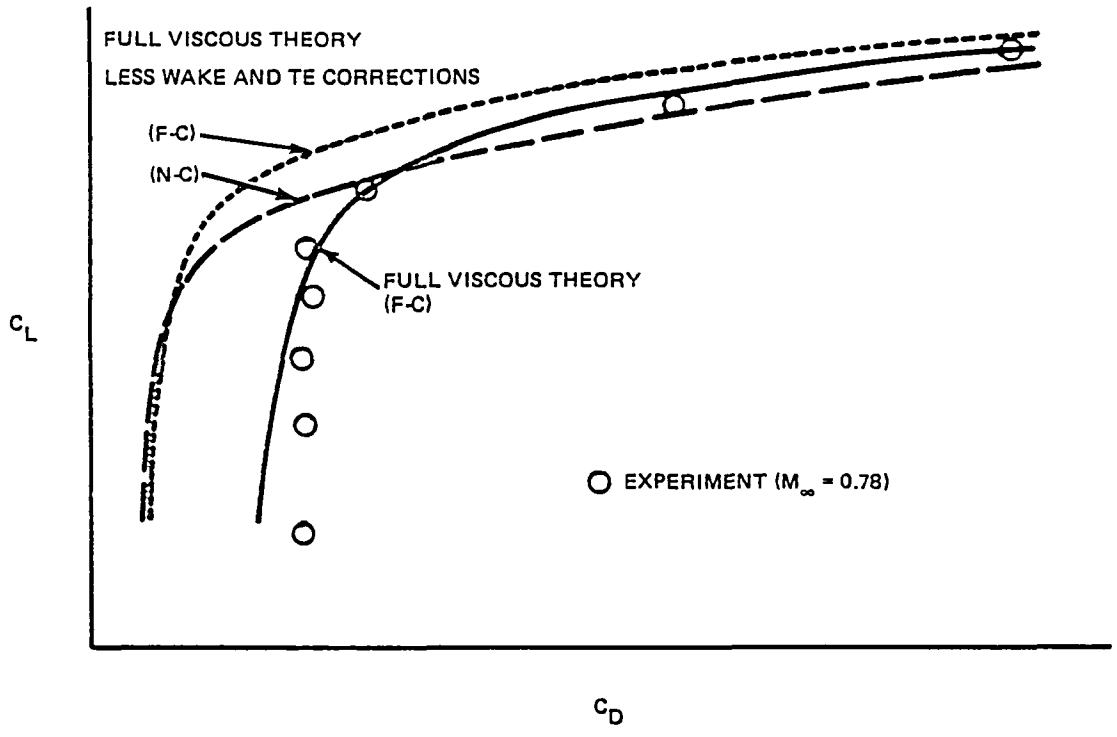

Figure 23 NASA LaRC — Drag Polar at $M_\infty = 0.768$, $R_\theta = 7.7 \times 10^6$, $(X_T = 0.28)$

In Fig. 24 we compare the theoretical and experimental pressure distribution for the highest lift coefficient of the drag polar. The comparisons are carried out at the same lift coefficient ($C_L = 0.94$) because of the uncertainties in the effective angle of attack in the wind tunnel. Note the relatively good agreement in the pressure distribution near the shock wave. Although the boundary-layer approximations used in the present theory are certainly not valid near shock-wave interaction regions, the present method does produce reasonable solutions in these regions. The results also show a smooth pressure distribution near the trailing edge. The elimination of all numerical smoothings from the present method has eliminated the wiggles that appeared in solutions obtained with earlier versions (Refs. 5 & 8) of the method. The slightly higher pressures in the theoretical solution between the shock wave and the trailing edge are likely due to the neglect of strong interaction effects associated with the nonzero, trailing-edge angle of this airfoil.

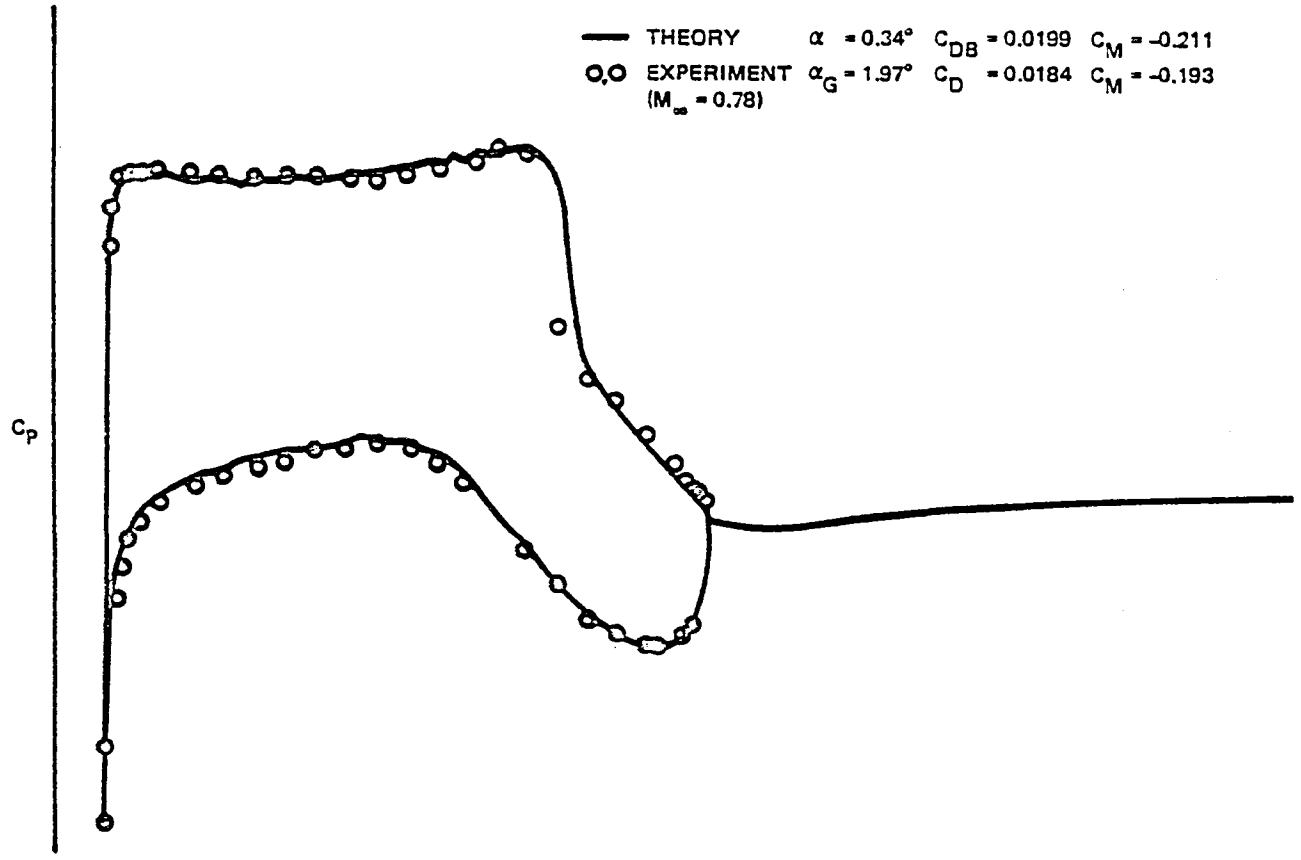

Figure 24 NASA LaRC — **Pressure Distribution at M_∞ = 0.768, C_L = 0.94, R_θ = 7.7 x 10^6 (X_T = 0.28)**

In Fig. 25 we present the theoretical solutions for the skin friction and displacement thickness on the upper surface of the airfoil. The discontinuities near the leading edge are due to transition from laminar to turbulent flow at 28% chord. The skin friction shows a nearly discontinuous drop to zero at the shock wave indicating that the flow is close to shock-induced separation and probably close to stall. We also call attention to the steep and nearly discontinuous jump in displacement thickness through the shock wave and the large increase in displacement thickness between the shock wave and trailing edge.

RAE 2822 Airfoil. - The airfoil is 12% thick supercritical section with a moderate amount of rear-loading and a trailing edge angle of 8.67°. The airfoil was subject to extensive testing (Ref. 70) in the RAE 8 x 6 foot transonic tunnel in which measurements of both surface pressures and boundary layer development were carried out. The examples considered in this report were carried out at Reynolds numbers from 2.7×10^6 to 6.5×10^6 and at two nominal Mach numbers, $M_\infty = 0.676$ and $M_\infty = 0.73$, with the lower Mach number resulting in subcritical flow and the higher value yielding supercritical flow. The supercritical cases covered a range of incidence resulting in a variation of shock strength from moderate to strong-enough to cause shock- induced boundary-layer separation. Transition was fixed at 11% chord in the lower Mach number (sub-critical) cases and at 3% chord in the higher Mach number (supercritical) cases. The momentum and displacement thicknesses, shape factor, and skin friction were determined from velocity-profile measurements made at a number of locations on the model, and the drag was determined from wake rake measurements. All theoretical solutions were carried out at the measured lift coefficients. The supercritical cases employed a small blockage correction of $\Delta M_\infty = 0.003$ which is consistent with recommendations[#] of Ref. 18.

The pressure distribution for the two subcritical cases are compared with experimental data in Figs. 26 and 27. These cases were for a Mach number of $M_\infty = 0.676$, Reynolds number $Re = 5.7 \times 10^6$, and $C_L = 0.566$ and $C_L = -0.121$. The agreement with experimental data is generally excellent over the entire airfoil

---

It was actually suggested in Ref. 18 that $\Delta M_\infty = 0.004$ be used as a blockage correction. However, this reference became available only after the present calculations are completed. The slight difference of $\Delta M_\infty = 0.001$ did not warrant a repeat of the computations.

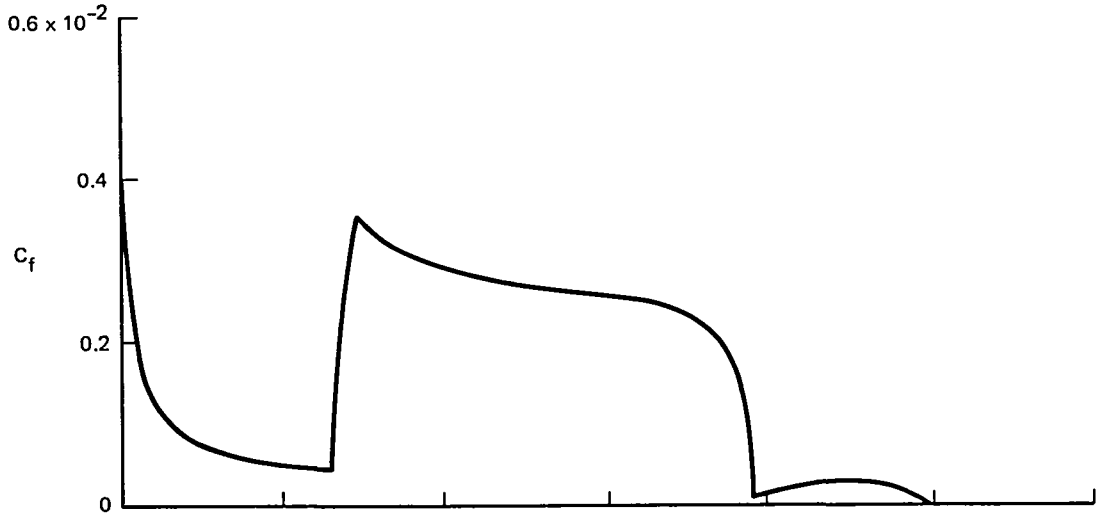

(a) SKIN FRICTION

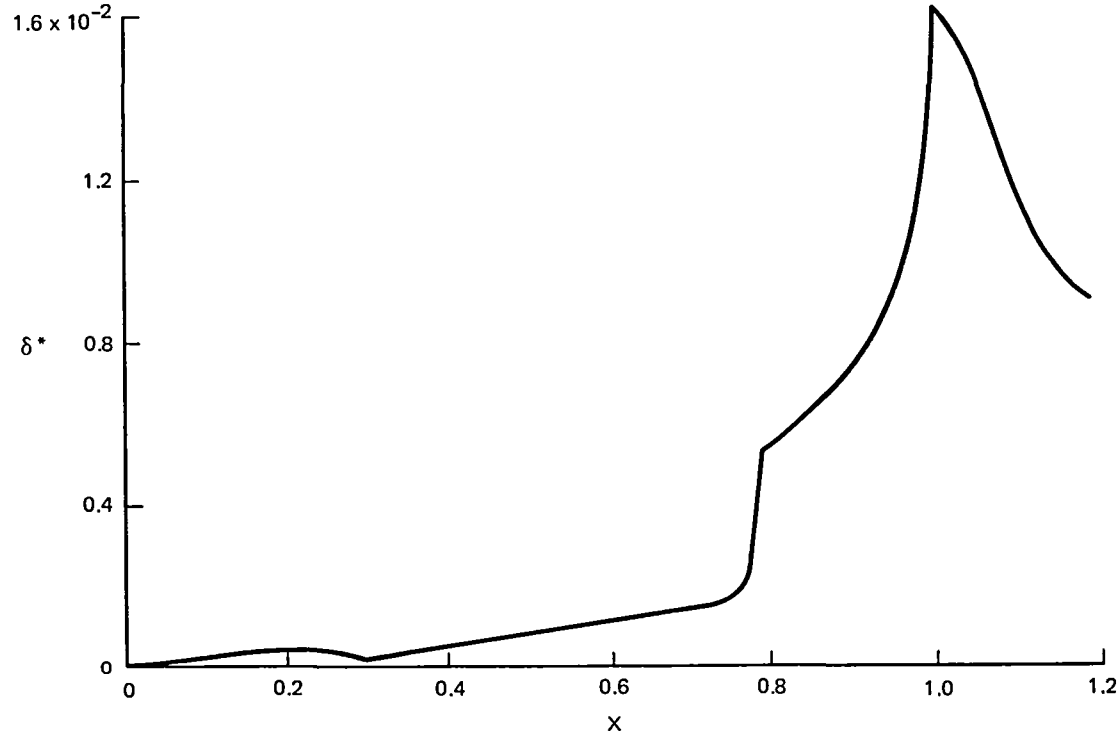

(b) DISPLACEMENT THICKNESS

Figure 25 NASA LaRC Supercritical Airfoil – Boundary Layer Development on the Upper Surface at $C_L = 0.94$

$M_\infty = 0.768$ $R_e = 7.7\ 10^6$ ($X_T = 0.28$)

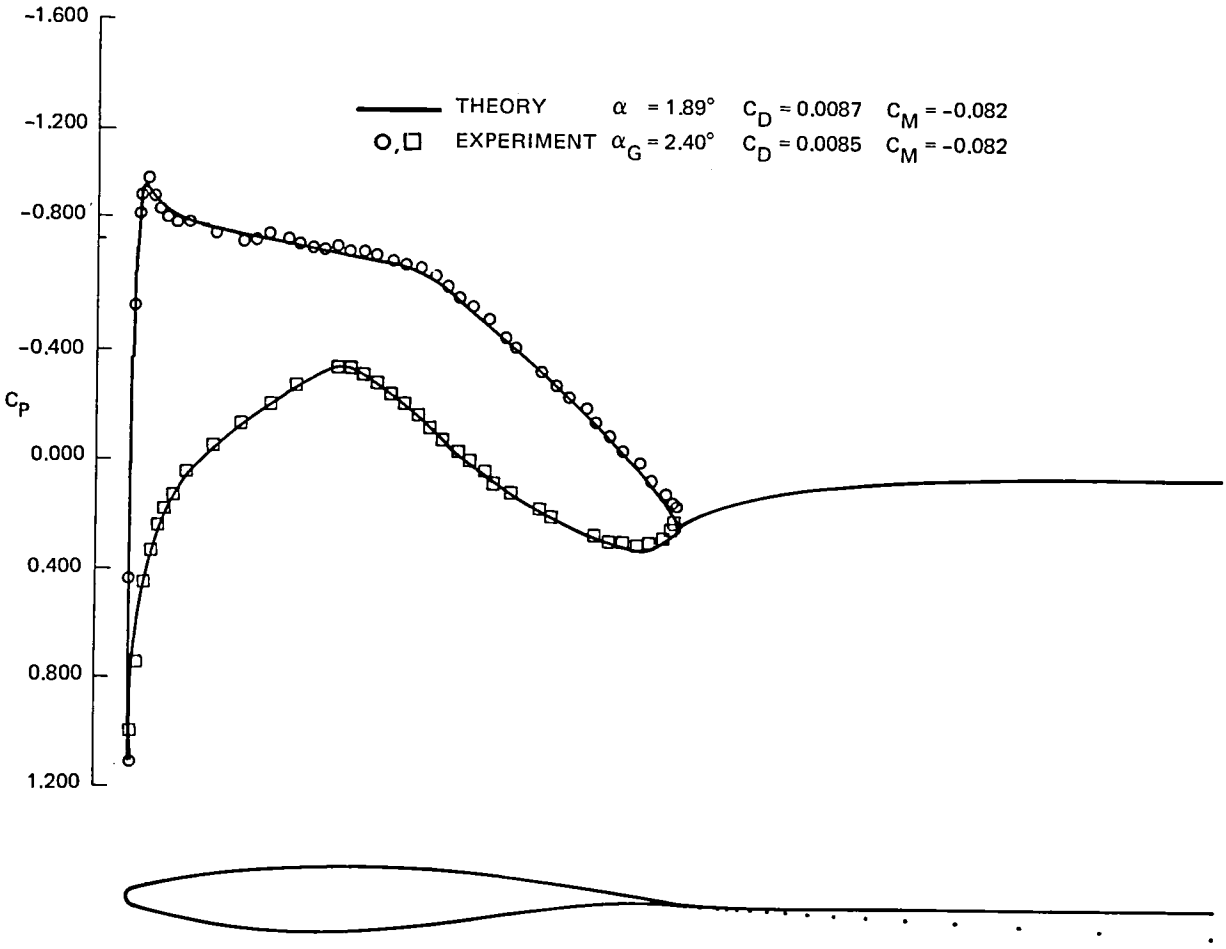

Figure 26 RAE 2822 — Pressure Distribution at $M_\infty = 0.676$, $C_L = 0.566$, $R_e = 5.7 \times 10^6$ ($X_T = 0.11$)

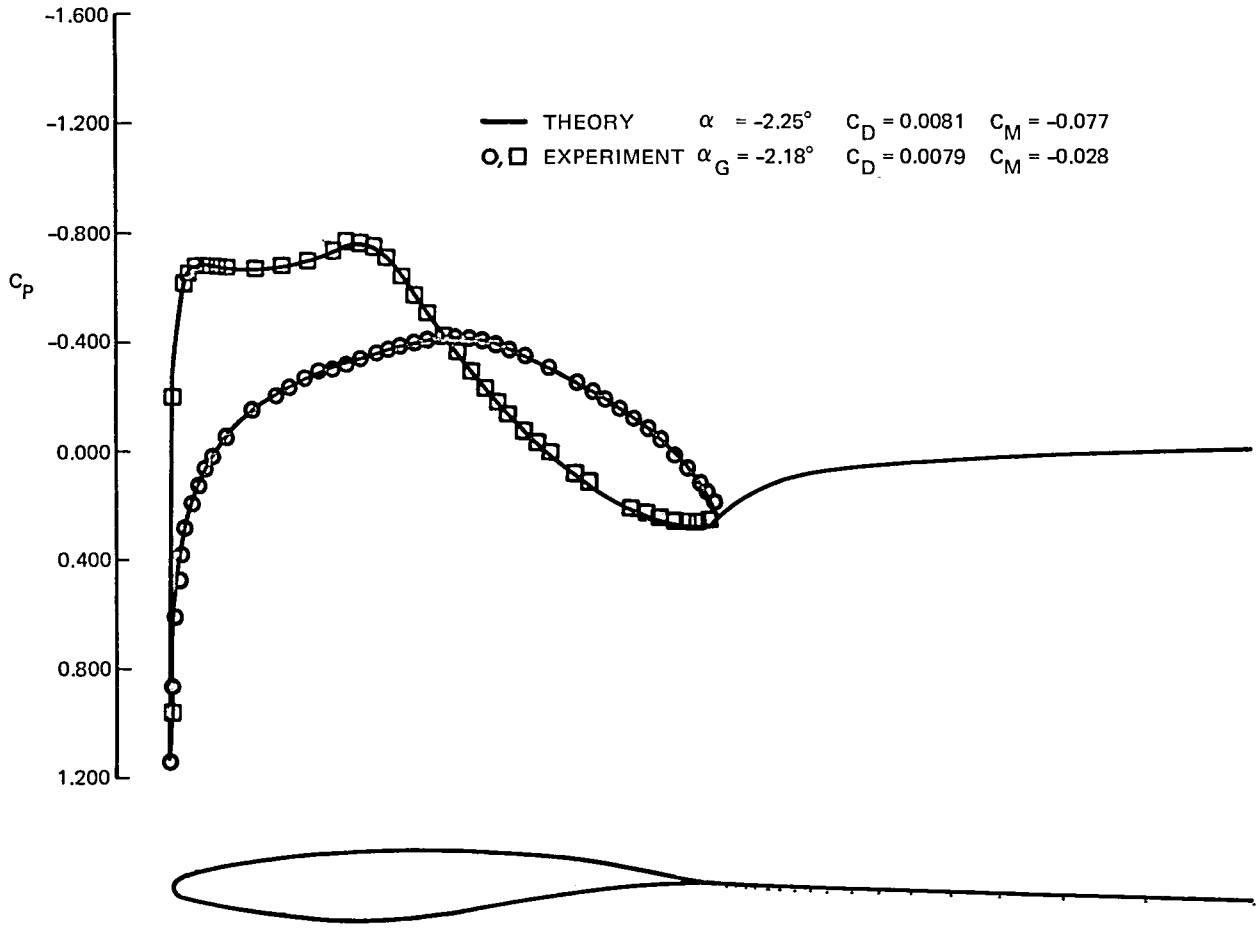

Figure 27 RAE 2822 – Pressure Distribution at $M_\infty = 0.676$, $C_L = -0.121$, $R_e = 5.7 \times 10^6$ ($X_T = 0.11$)

for both cases, with a tendency of the theory to predict a slightly higher pressure on the upper surface near the trailing edge. This trend appears in all the RAE 2822 cases considered, and is likely due to total pressure losses across the shock wave that are not accounted for in the potential flow formulation. As previously discussed, the prediction of drag for these two subcritical cases was also in very good agreement with experimental data (see Table 4).

The pressure distribution for three supercritical cases tested at a Reynolds number of Re = 6.5 x 10^6 and a nominal Mach number of M_∞ = 0.73 are compared with experiment in Figs. 28, 29 and 30. Both F-C and N-C solutions are shown in the comparisons. In addition, in the last case for C_L = 0.803, we have included a solution carried out at the experimentally quoted Mach number to illustrate the effect of a small Mach number shift (ΔM_∞ = 0.003) on the solution. The F-C solution clearly shows the best agreement with experiment. In all three cases the agreement between theory and experiment is excellent on the lower surface and the shock-wave position and strength on the upper surface are well predicted in the F-C solutions. This set of results also shows very good agreement with experiment for the pressure rise through the shock wave. Both the theoretical and experimental results indicate that the pressure rise across the shock wave is only about one-half of that required by the normal shock-wave relations. The overall levels of the pressure distribution on the upper surface of the airfoil are also reasonably will predicted. The small discrepancies between theory and experiment over the forward part of the upper surface is probably due to both the roughness strip used to fix transition and wall-interference effects. The overprediction of the pressure on the upper surface near the trailing edge in Figs. 28 and 29 is likely due to effects associated with the nonzero trailing-edge angle not accounted for in our trailing-edge solution. The discrepancy is somewhat larger in the higher lift case of Fig. 30, probably because of the stronger shock wave and closeness of the boundary layer to separation. The poorer agreement may be due to shortcomings in the lag entrainment method at high values of the shape factor.

Since the flow field in these last three cases is supercritical, the total drag is given by the sum of wave drag and profile drag. We have previously shown that the profile drag of this airfoil can be well predicted by integration of the pressure and shear stress. Since the present method seems to give a good prediction of shock

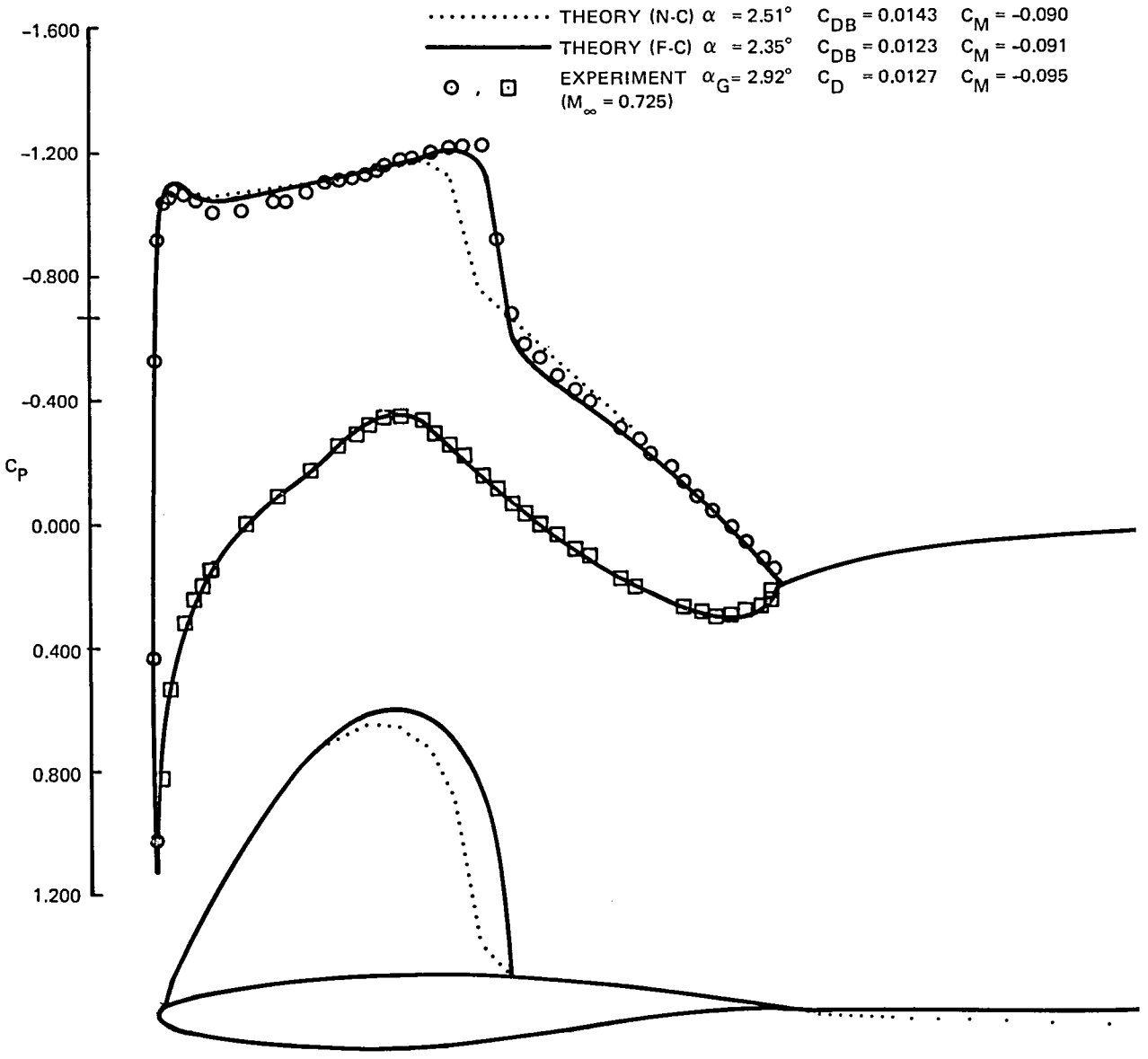

Figure 28 RAE 2822 -- Pressure Distribution at $M_\infty = 0.728$, $C_L = 0.743$, $R_e = 6.5 \times 10^6$ ($X_T = 0.03$)

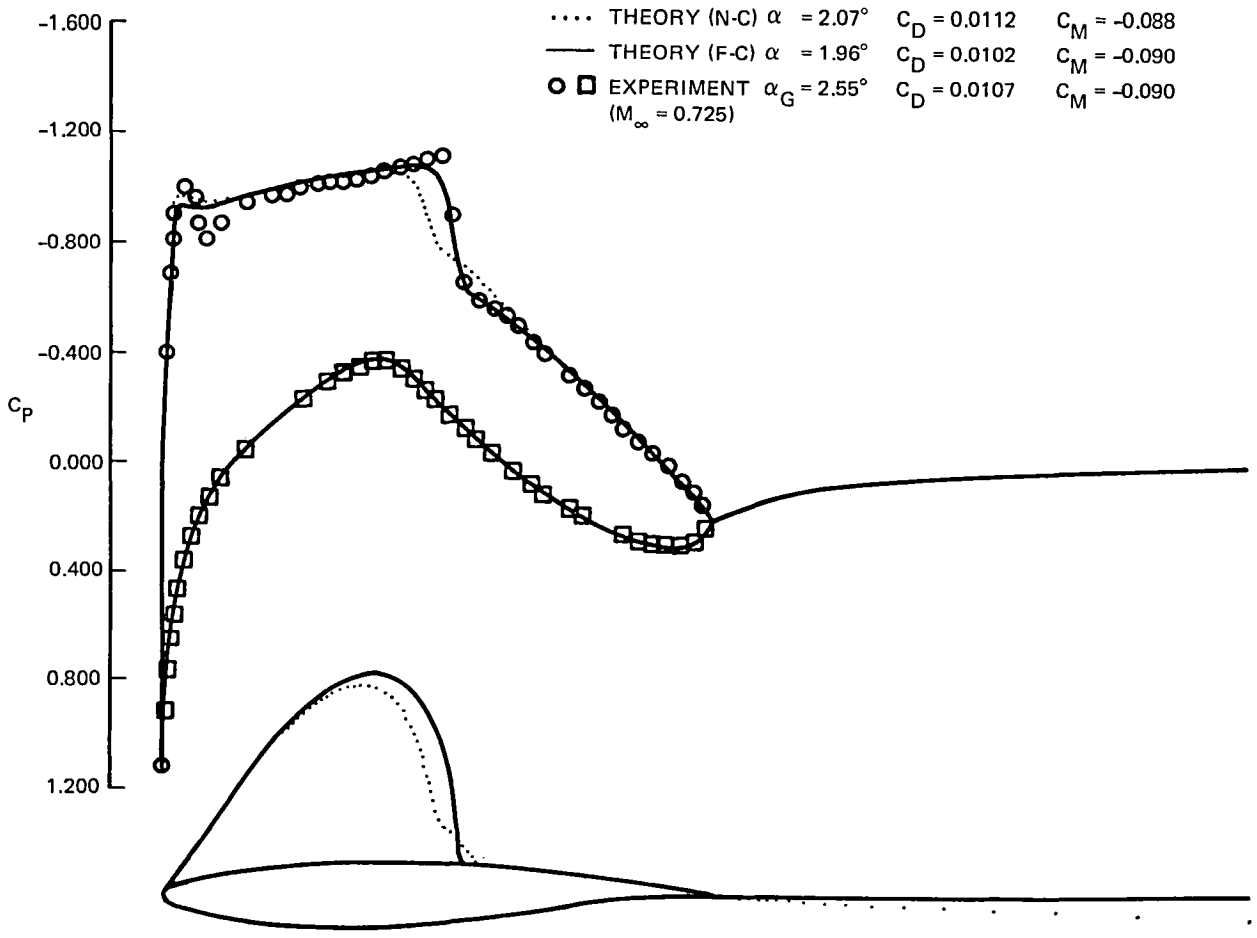

Figure 29 RAE 2822 – Pressure Distribution at $M_\infty = 0.728$, $C_L = 0.658$, $R_e = 6.5 \times 10^6$ ($X_T = 0.03$)

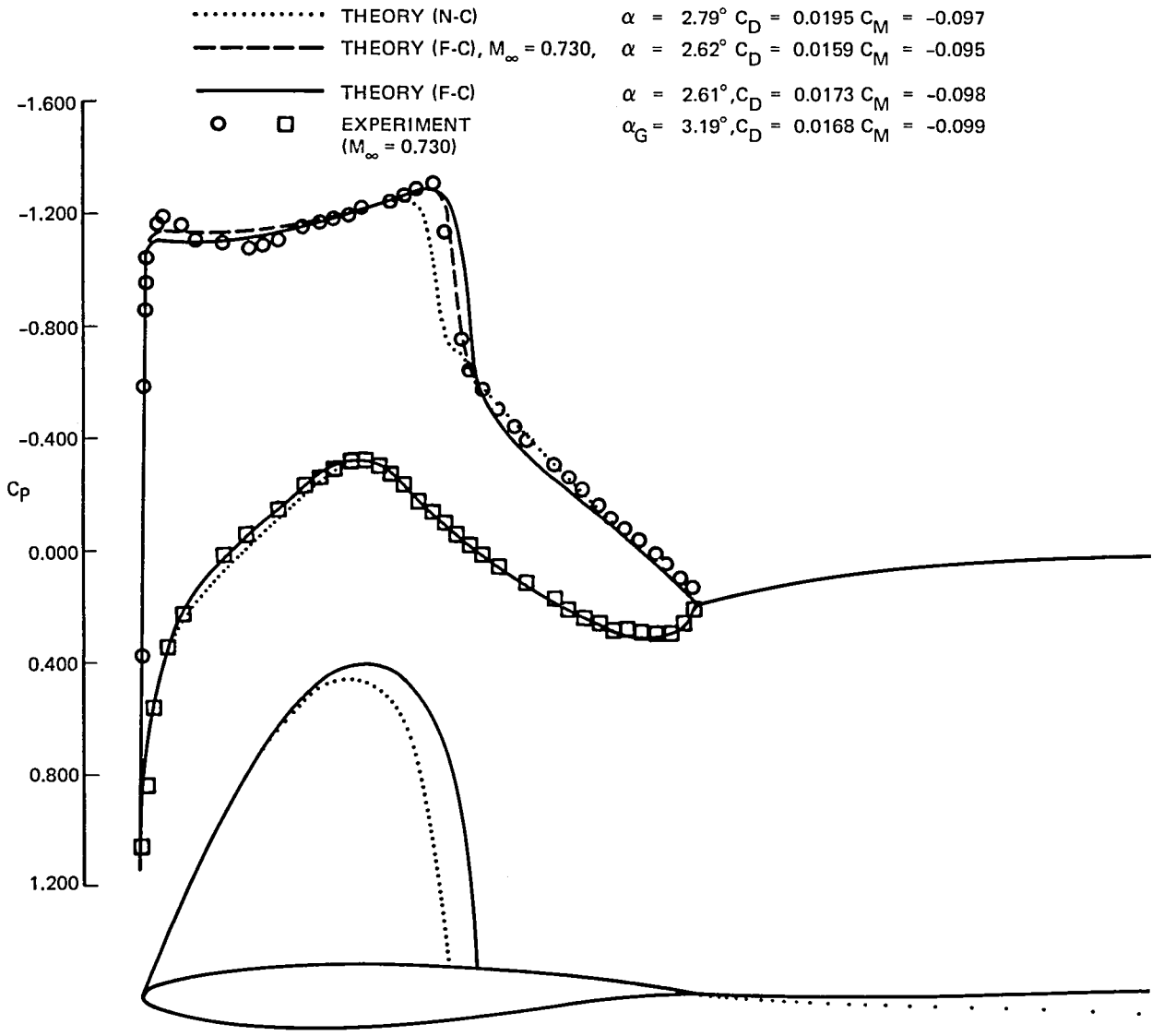

Figure 30 RAE 2822 — Pressure Distribution at M_∞ = 0.733, C_L = 0.803, R_e = 6.5 x 10^6 (X_T = 0.03)

strength, it can also be expected to give useful predictions of wave drag and total drag. This expectation is borne out in the comparison of the drag polar in Fig. 31. The theoretical solutions are integrated drags determined from the surface pressure and shear stress distributions. We should point out that useful estimates for the wave drag can be determined by subtracting the momentum drag (equal to $2\theta_\infty$) from the total drag computed by the surface integrations. We note that the F-C solution is in good agreement with the measured values of drag. The small underprediction of the theory evident in the figure amounts to no more than five counts of drag. About half of the difference is due to the use of first-order differencing ($c_2 = 0$) in the inviscid solution. The remaining discrepancy can be associated with the slight overestimate of the pressures on the upper surface near the trailing edge that was pointed out earlier. These results clearly show that the N-C scheme leads to an inferior prediction of both shock wave location and drag.

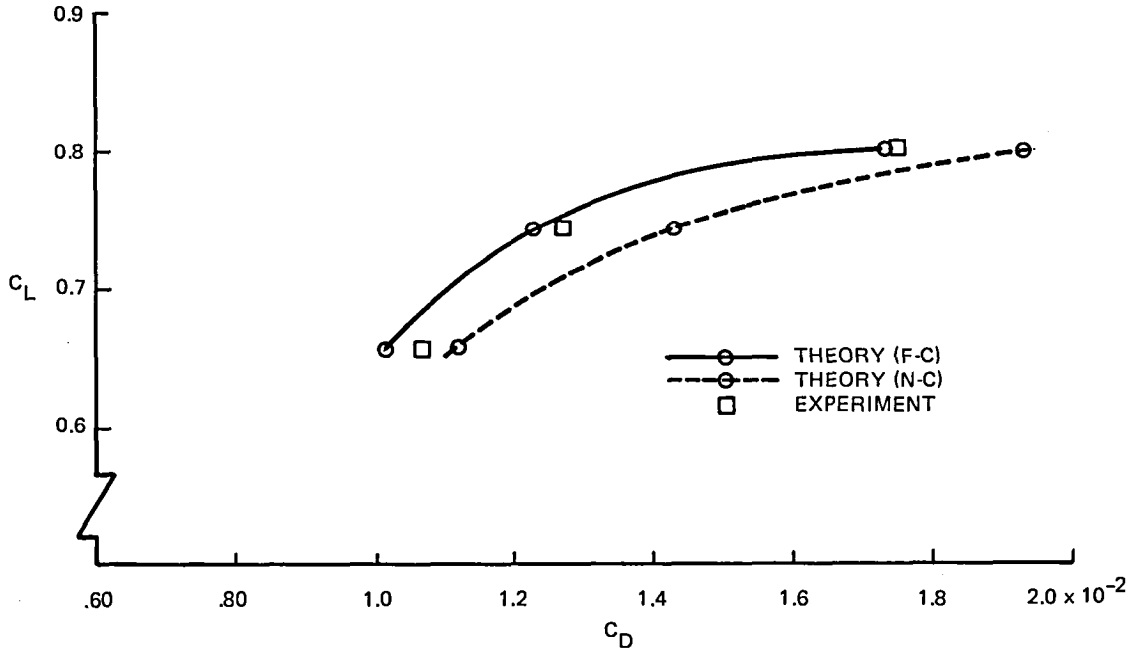

Figure 31 RAE 2822 – Drag Polar at $M_\infty \cong 0.73$, $R_e = 6.5 \times 10^6$, ($X_T = 0.03$)

The theoretical solution (F-C) for the boundary-layer development on the upper surface of the airfoil is compared with experimental measurements for the two subcritical cases in Figs. 32 and 33 and for two supercritical cases in Figs. 34 and 35. Included in these figures are the solutions for the displacement and momentum thicknesses (δ^*, θ), shape factor (h), skin friction (c_f), and, for the two supercritical cases, the solution for the source velocity, ($V_e(s)$) on the airfoil surface.

The two subcritical flows in Figures 32 and 33 involve mild pressure gradients and boundary layers not close to separation. The discontinuities near the leading edge are due to transition from laminar to turbulent flow. Both theory and experiment show rapid increases of displacement thickness and shape factor near the trailing edge that are typical of airfoil flows. The agreement between theory and experiment for all quantities is good for both cases. The good agreement observed just downstream of transition indicates that the transition jump conditions employed in the theoretical model were adequate. The close agreement between the theoretical and experimental values of the momentum thickness at the trailing edge is consistent with the good predictions of profile drag in these two cases.

The boundary-layer development for the two higher-lift, supercritical cases is given in Figs. 34 and 35. The overall agreement between theory and experiment is relatively good over the entire upper surface aside from a tendency to slightly underpredict δ^*, θ, and h between the shock wave and the trailing edge. The higher lift case considered in Fig. 35 contains data from two different probes. The differences between the two data sets provide some measure of the uncertainty in the data. The experimental displacement thickness shows a very rapid and nearly discontinuous rise through the shock wave, followed by a more gradual but larger growth toward the trailing edge. The theory gives a good representation of this behavior in both cases. The solution for the skin friction shows the characteristic behavior near shock waves; a rapid, nearly discontinuous fall followed by a gradual increase resulting in the development of a minimum in skin friction at the shock wave. This behavior is reflected in the solution of the shape factor which shows a very steep rise followed by a more gradual decrease behind the shock wave. The agreement between theory and experiment for c_f and h is quite good except for the

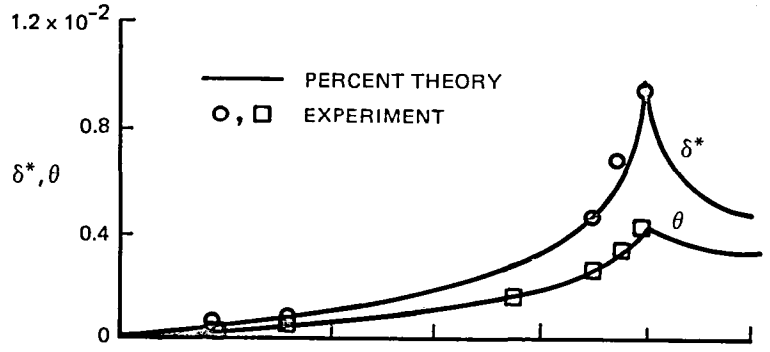

(a) DISPLACEMENT AND MOMENTUM THICKNESS

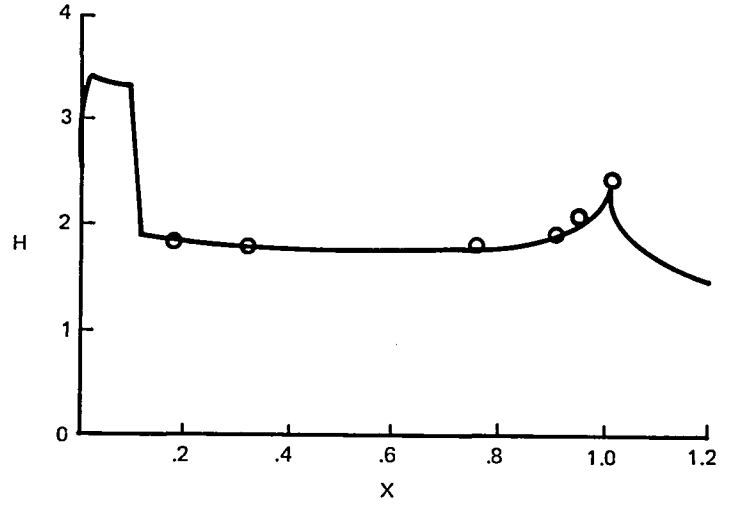

(b) SHAPE FACTOR

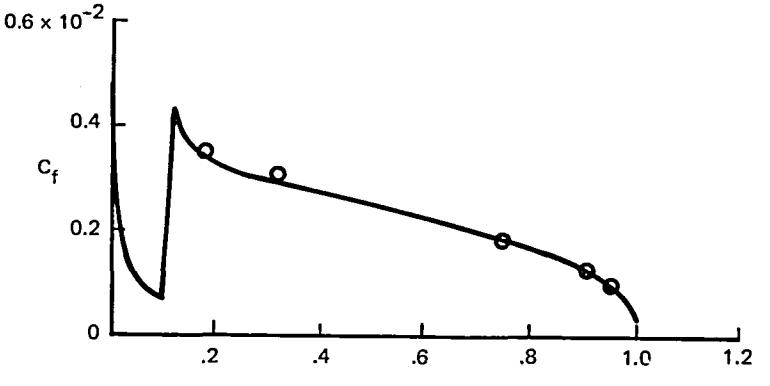

(c) SKIN FRICTION

Figure 32 RAE 2822 — Boundary Layer Development at $M_\infty = 0.676$, $C_L = 0.566$, $R_e = 5.7 \times 10^6$ ($X_T = 0.11$)

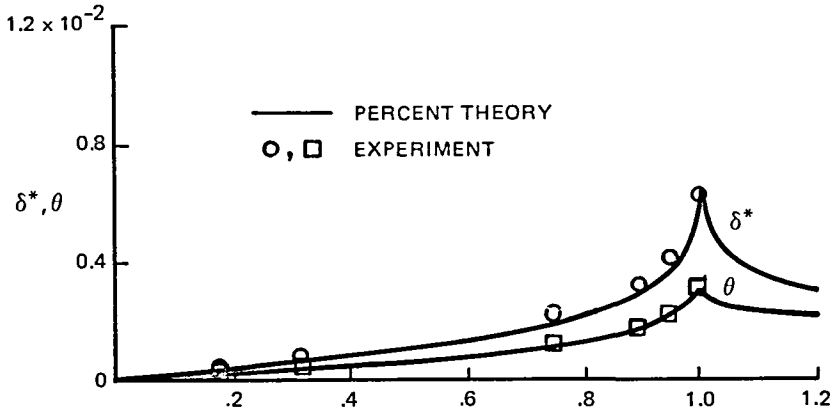

(a) DISPLACEMENT AND MOMENTUM THICKNESS

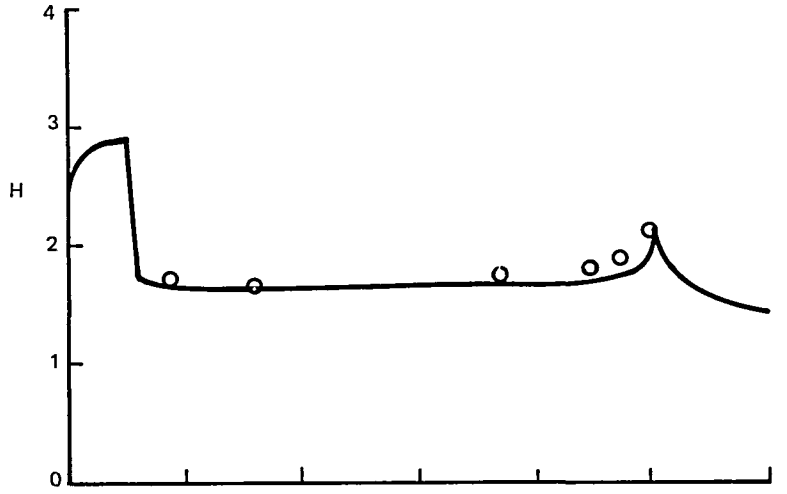

(b) SHAPE FACTOR

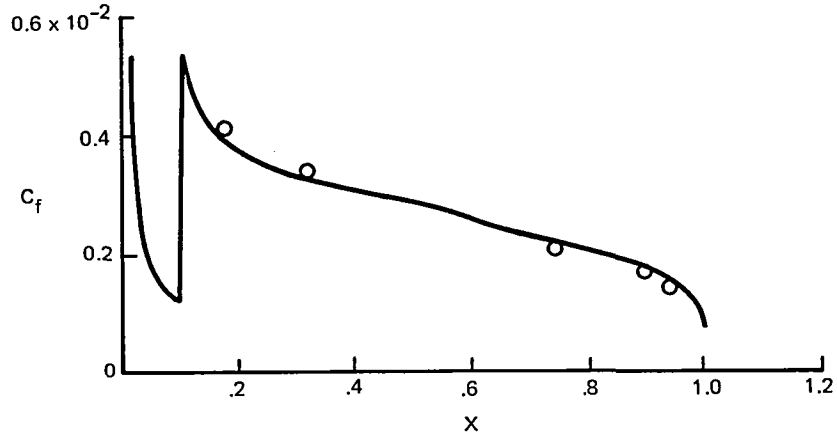

(c) SKIN FRICTION

Figure 33 RAE 2822 – Boundary Layer Development at $M_\infty = 0.676$, $C_L = -0.121$, $R_e = 5.7 \times 10^6$, ($X_T = 0.11$)

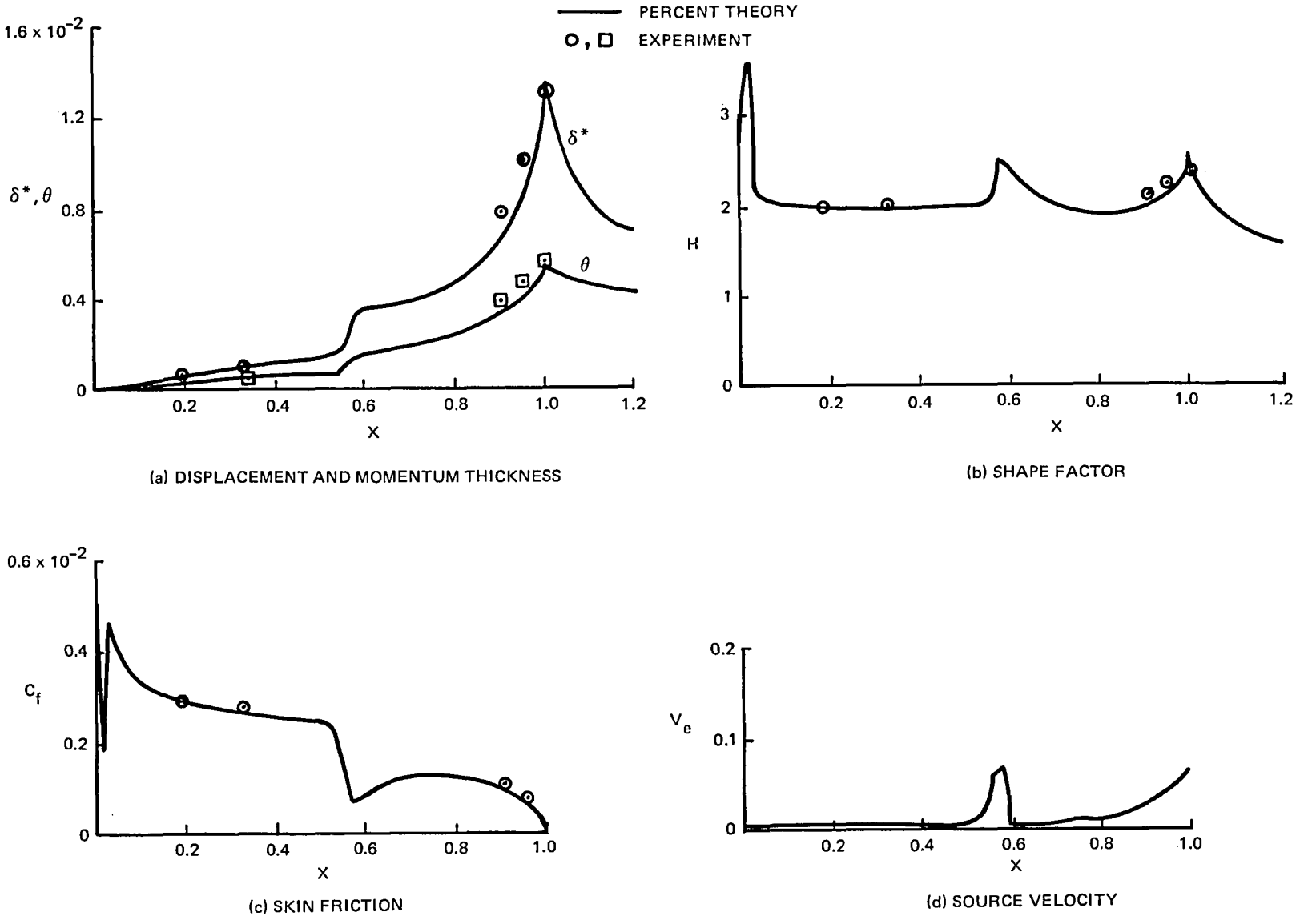

Figure 34 RAE 2822 – Boundary Layer Development at $M_\infty = 0.728$, $C_L = 0.743$, $R_e = 6.5 \times 10^6$ ($X_T = 0.11$)

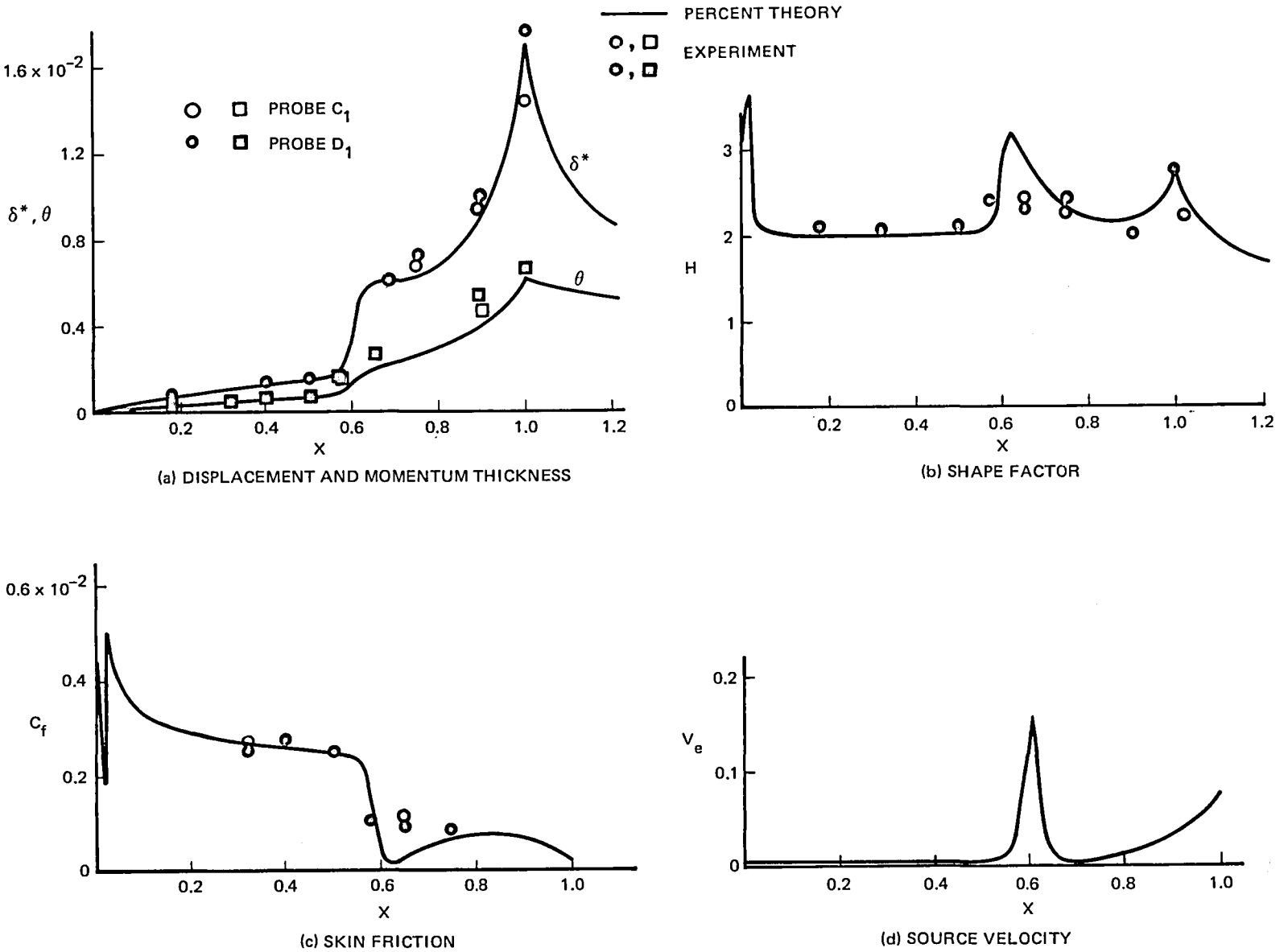

(a) DISPLACEMENT AND MOMENTUM THICKNESS

(b) SHAPE FACTOR

(c) SKIN FRICTION

(d) SOURCE VELOCITY

Figure 35 RAE 2822 — Boundary Layer Development at $M_\infty = 0.733$, $C_L = 0.803$, $R_e = 6.5 \times 10^6$, ($X_T = 0.11$)

points immediately behind the shock wave in the $C_L = 0.803$ case in Fig. 35. The shock strength in the case is relatively large (The local Mach number upstream of the shock wave was $M_L = 1.31$), and the boundary layer is on the verge of separating at the foot of the shock wave.

The theoretical solutions for the corrected source velocity for the $C_L = 0.743$ and $C_L = 0.803$ cases are shown in Figs. 34d and 35d, respectively. These solutions show a large and highly localized increase of the source velocity at the shock wave followed by a more gradual, but equally significant, growth toward the trailing edge. These results clearly show the highly localized nature of the shock wave/boundary layer interaction in the present theoretical model The interacting boundary-layer description basically truncates the delta function behavior that would otherwise arise at the shock impingement point were interaction not allowed in the formulation. The resulting source velocity displays a highly peaked but finite distribution which increases in amplitude with increasing shock strength (Compare Figs. 34d and 35d.)

The final case considered is for $M_\infty = 0.753$, $C_L = 0.743$, $Re = 6.2 \times 10^6$, and $X_T = 0.03$. The main difference from the previous cases is a higher Mach number and a much lower Reynolds number. These conditions lead to a more rearward and stronger shock wave ($M_L = 1.35$) which, combined with the lower Reynolds number, leads to massive separation at the foot of the shock wave. The pressure distribution and boundary-layer parameters are compared with experiment in Figs. 36 and 37, respectively. The agreement between the theoretical and experimental pressure distributions remains excellent on the lower surface but deteriorates noticeably on the upper surface. The overall levels of the pressure in front of the shock wave are in good agreement on the upper surface except near the leading edge where the discrepancy is much larger. However, in the theoretical solution, the shock wave is too far aft, its strength is overpredicted, and the pressure levels behind the shock wave are overpredicted. The experimental pressures on the upper surface are much lower near the trailing edge, showing clear signs of trailing-edge divergence-a classical indicator of boundary-layer separation. Although both the theoretical and experimental skin friction distributions clearly show separation, pressure divergence

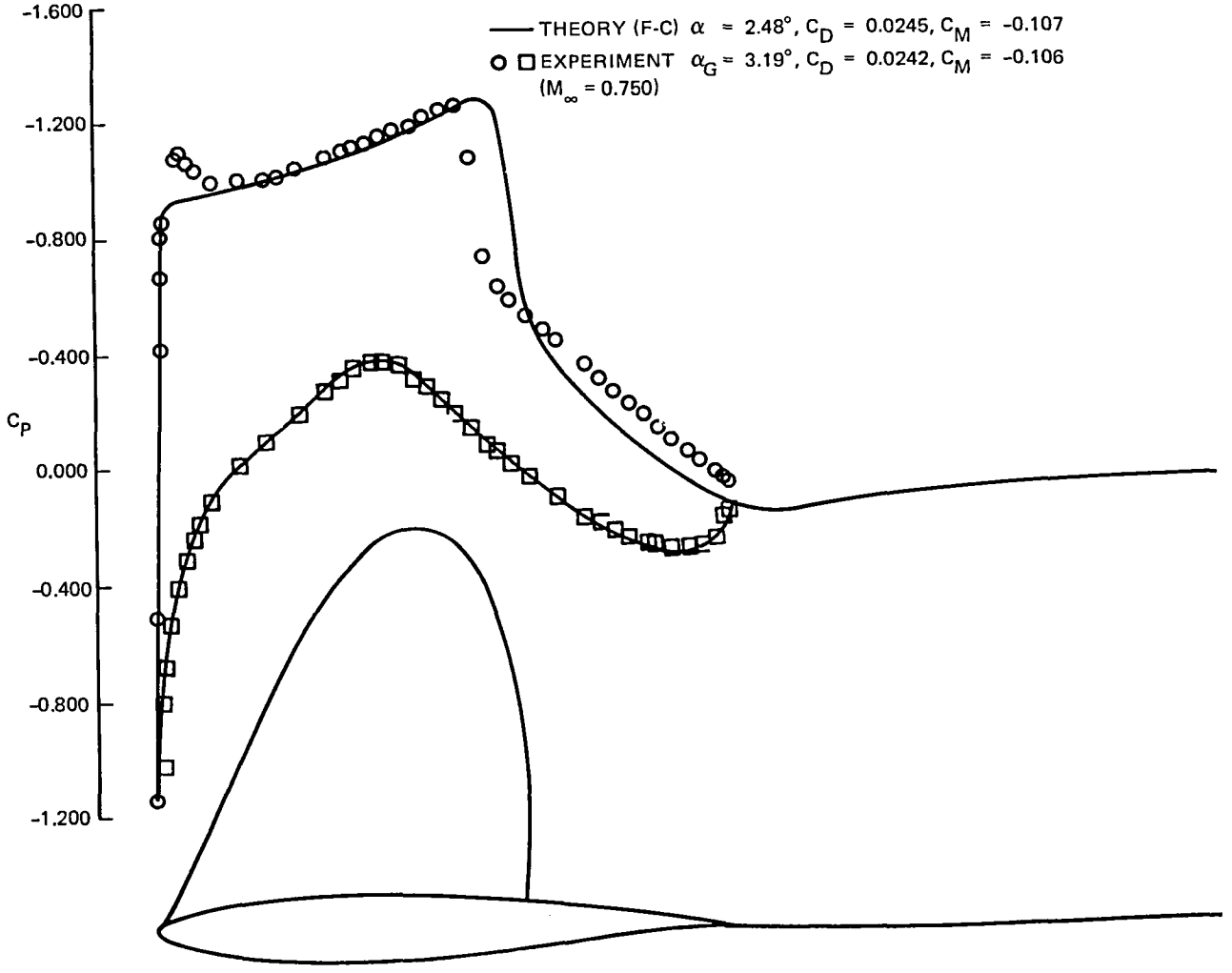

Figure 36 RAE 2822 — Pressure Distribution at $M_\infty = 0.753$, $C_L = 0.743$, $R_e = 6.2 \times 10^6$ ($X_T = 0.11$)

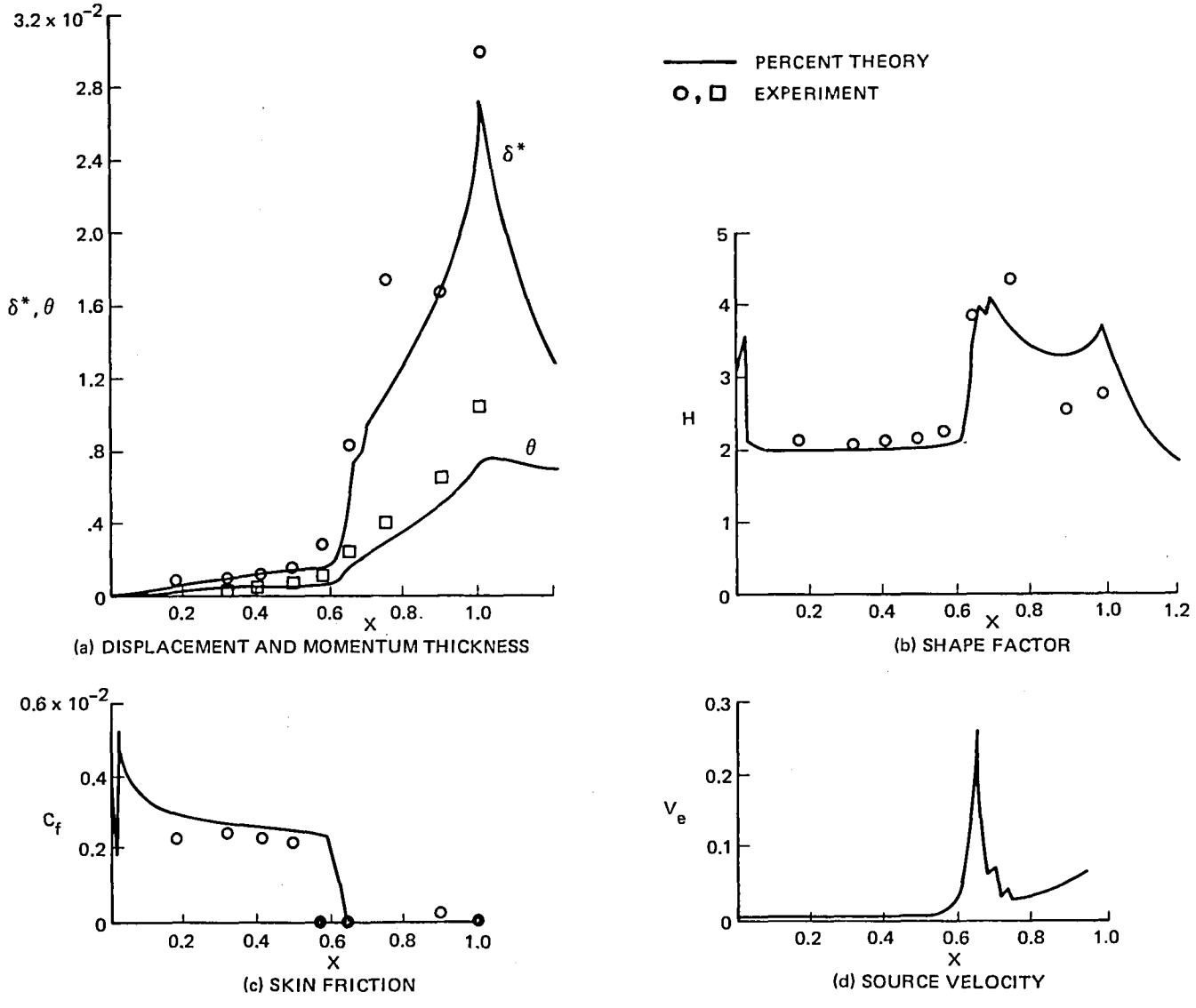

Figure 37 RAE 2822 — Boundary Layer Development at $M_\infty = 0.753$, $C_L = 0.743$, $R_e = 6.2 \times 10^6$ ($X_T = 0.11$)

at the tailing edge is not apparent in the theoretical results and this must be considered a major shortcoming of the therory. The failure of the theory to adequately predict the pressure distribution behind the shock wave is likely due to an inadequacy in the lag-entrainment method at high values of the shape factor. The comparisons of the displacement and momentum thicknesses given in Fig. 35a show that the theory gives a reasonably good description of boundary-layer growth in front of and through the shock-pressure rise. However, it is seen that the theory seriously underpredicts the boundary-layer growth behind the shock wave. It is this underprediction of the boundary-layer thickness behind the shock wave that is most likely responsible for the observed discrepancy in shock position. The failure of the method behind the shock wave is also evident in the comparison of the shape factor in Fig. 37b. The comparison of the skin friction is given in Fig. 37c. The values of the skin friction in the reversed flow could not be determined in the experiment. However, the presence of separation could be detected and such points are indicated by the filled symbols in Fig. 37c. As previously noted, the skin friction in the theoretical model is set to zero in regions of separation. Note that both theory and experiment predict separation behind the shock wave.

The solution for the surface source velocity in Fig. 37d shows an extremely large increase at the shock wave because of separation. In general, this is a rather extreme case for the present theory, which was not intended to deal with regions of extensive separated flow. Nevertheless, the present theory does seem to provide a reasonably good prediction of the overall features of the flow and a surprisingly accurate prediction of the drag. The theoretical drag was $C_{DB} = 0.0245$ compared to the experimental value of $C_{DB} = 0.0242$. In view of the significant differences between the theoretical and experimental shock strength and location and displacement-thickness distributions, this good prediction of the drag should be considered fortuitous.

Collyer and Lock (Ref. 18) recently carried out similar comparisons between the RAE 2822 data and results of their method. Their method is similar in many respects to the present full viscous-flow theory in that both include the wake-thickness and wake-curvature terms in the matching conditions. The Collyer-Lock method differs from the present method in three ways: (1) it does not account for the strong interaction at the trailing edge; (2) it requires significant numerical smoothings particularly near the trailing edge while the present method uses no smoothings; and

(3) it employs a special partially-conservative (P-C) scheme while the present method uses a standard fully-conservative (F-C) method. The P-C differencing method involves an arbitrary parameter, λ, that weighs the relative proportion of conservative ($\lambda = 1$) to non-conservative ($\lambda = 0$) differencing used in the method. The position of the shock wave and the value of the drag in the P-C method seemed to be sensitive to the value of λ. Good agreement with data was demonstrated in Ref. 18 but for values of λ that were varied for the different cases. The present work clearly indicated that the best results were obtained with the fully-conservative difference scheme in all cases.

Comparisons of the RAE 2822 data set with Deiwert's (Ref. 20) Navier-Stokes (NS) method were also recently carried out by Swafford in Ref. 77. The Navier-Stokes calculations showed very poor agreement with the RAE 2822 data. The poor performance of the NS method in this case was very likely due to the coarse grid employed in the computations of Ref. 77 (Fourty points were used around the airfoil in the NS computations compared to the 160 points used in the present set of calculations.) The coarse grid notwithstanding, the NS method required about ten times greater computer time than the present interacting boundary-layer method.

6. CONCLUDING REMARKS

In this report we described important extensions to the usual interacting boundary-layer theory for computing the viscous effects on airfoils. Our method was based on formal asymptotic expansions of the full Reynolds equations of turbulent flow for $Re \to \infty$. Formal analysis indicated that both wake-induced effects and normal pressure-gradient effects near trailing edges contribute to the lowest-order solution. Consequently, both must be retained along with standard displacement effects on the airfoil in order to obtain a consistent formulation. The main contributions of the present work were the determination of the local trailing-edge solution and the development of systematic procedures for incorporating wake and trail-edge interaction effects into the theoretical description. The inner solution accounted for normal pressure gradient effects across the boundary layer in the vicinity of the trailing edge and is valid for airfoils with cusped or nearly cusped trailing edges.

Results presented in this report for a variety of airfoils indicated that the new method gave reasonable predictions of the pressure distribution, shock location, forces, and moments on airfoils in transonic flows. In particular, the new method seems to give very accurate predictions of the absolute levels of the drag. Comparative studies have indicated that both the wake and trailing-edge corrections terms make an important contribution that must be included in the formulation if accurate predictions of section characteristics are to be obtained. Neglect of either contribution leads to noticeable errors in shock position, pressure distribution, lift, and drag. In addition, the present study clearly indicated the superiority of conservative finite-difference formulations. The use of non-conservative differencing leads to substantial over-predictions of the drag and to shock positions that are too far forward. The present method is more complete and is clearly an improvements over previous boundary-layer type methods. It agrees well with experiment, requires little computing time, and is, therefore, well suited to aerodynamic design. The method requires about 10 minutes on an IBM 370-168 computer to obtain converged solutions for unseparated cases. This is about three times that required for a corresponding calculation of an inviscid flow. These computer times are for unsmoothed versions of

the theory. Faster run times can be achieved with numerical smoothings but only at the expense of noticeably degraded solutions.

The present method does not properly treat the details of shock wave/boundary layer interactions. These interactions produce significant normal pressure gradients in the boundary layer that are completely ignored in the simple interacting boundary-layer equations used in our approach. Nevertheless, the new method seems to give adequate predictions of the pressure distributions in the shock-wave interaction zones. It is a well known experimental fact that the pressure rise through a shock wave is about half that required by the normal shock-wave relations. This behavior is well represented by the present method which also seems to give a consistently good prediction of the pressure level behind the shock wave. The consequences of using a crude description of the shock wave/boundary layer interaction process do not appear to be great. The overall increase in displacement thickness through the shock wave is reasonably well predicted by the present method, and this seems to be the most important ingredient in obtaining good overall predictions of the section characteristics of airfoils in supercritical flow.

The present method has two other more important deficiencies that should be mentioned. Namely, it does not properly treat the flow near the trailing edge of an airfoil with non-zero trailing edge angles, and it does not adequately deal with boundary layer separation. Fortunately, the present method seems to yield reasonably good predictions when applied to more general airfoils with non-zero trailing edge angles provided the trailing edge angles are small. However, the solution for the NACA 0012 airfoil ($\theta_{TE} = 16°$) showed pressures that were somewhat too high near the trailing edge and drags that were substantially lower than experimental values. These discrepancies were undoubtedly caused by pressure variations across the boundary layer in the vicinity of the trailing edge that are not accounted for in our local inner solution. These extra pressure variations across the boundary layer are generated by the curved streamlines associated with the local wedge flow near the trailing edge. These effects can be incorporated into the method through an appropriate generalization of our inner trailing-edge solution. This improvement of the theory would very likely result in better predictions of drag for this type of airfoil and should therefore be pursued. Although the present method functions for separated flow has produced reasonably good agreement with experiment in some cases, it is clearly not satisfactory in this regard. The lag-entrainment method was developed

from a data base for attached boundary layers and was not intended to deal with separated flows or with boundary layers with large shape factors. Treatment of separation in the present method can be improved through improvements in the lag-entrainment method (Some effort in this direction has been reported (Ref. 78).) or through the use of other integral methods (Ref. 79) specifically designed for separated turbulent boundary-layers. In addition, the iteration scheme used to solve the coupled inviscid and boundary layer equations loses some effectiveness when separation is present. In these situations, solutions can be obtained only through the use of drastically reduced relaxation factors, resulting in very long computer times. Improved convergence can probably be achieved through the use of an iteration scheme developed by Carter (Ref. 80) and LeBalleur (Refs. 81 & 82) for separated flows.

The most important result of the present work is the demonstration that a simple interacting boundary-layer approach can be effective tool for predicting viscous effects on airfoils. Unfortunately, because of uncertainties in the experimental data, due primarily to wind-tunnel wall interference, this must be regarded as a tentative conclusion. A more clear-cut validation of the new theory would require improved wind-tunnel tests with either small wall effects or accurate and well-documented corrections.

7. EPILOGUE

The present report was completed in early 1980 and the computations reported herein were carried out with a preliminary version of the GRUMFOIL computer code designated MCMJ-4. Since that time, the GRUMFOIL code has undergone extensive modification to incorporate a variety of improvements made to the theoretical formulation. First, the hybrid, SLOR-direct solver, used to solve the full potential equation, was replaced with a multi-grid method (Ref. 3) which accelerated convergence by a factor of five in computing time. Second, an improved, second order artificial viscosity and far field treatment was incorporated into the finite difference scheme used for the inviscid flow. These significantly reduced the spatial truncation error, improved the reliability of the second-order versions of the code, and reduced by one-half the number of mesh points required to achieve a given accuracy. Finally, the turbulence closure relations employed in the original Green's lag entrainment method modified to improve the treatment of separated flow, and the direct method employed for the global, viscid-inviscid iteration was replaced with Carter's semi-inverse method to permit solution of the resulting turbulent boundary layer equations when separation is present. Together, these changes led to a more accurate, robust, and faster code which is capable of treating flows with extensive regions of separated flow and which runs about ten times faster than the original MCMJ-4 version. Further details of the new code, designated MCMJ-9N, are given in Ref. 83. The user manual in the companion volume, Ref. 69, is based on the new MCMJ-9N version of the code.

8. REFERENCES

1. Ballhaus, W.F., Jameson, A. and Albert, J., "Implicit Approximate Factorization Schemes for the Efficient Solution of Steady Transonic Flow Problems," AIAA. J., Vol. 16, No. 6, 1978, pp. 573-579.

2. Holst, T.L., "A Fast, Conservative Algorithm for Solving the Transonic Full-Potential Equation," Proceedings: AIAA Computational Fluid Dynamics Conference, July 1979, pp. 109-121.

3. Jameson, A., "Acceleration of Transonic Potential Flow Calculations on Arbitrary Meshes by the Multiple Grid Method," Proceedings: AIAA Computational Fluid Dynamics Conference, July 1979, pp. 122-146.

4. Melnik, R.E. and Chow, R., "Asymptotic Theory of Two Dimensional Trailing Edge Flows," NASA Conference on Aerodynamic Analysis Requiring Advanced Computers, NASA SP-347, 1975 (also Grumman Research Department Report RE-510J, 1975).

5. Melnik, R.E., Chow, R., and Mead, H.R., "Theory of Viscous Transonic Flow Over Airfoils at High Reynolds Number," Paper No. 77-680, AIAA 10th Fluid and Plasma Dynamics Conference, Albuquerque, N.M., June 1977.

6. Jameson, A., "Numerical Computation of Transonic Flow with Shock Waves," Symposium Transsonicum II, Springer-Verlag, New York, 1975.

7. Jameson, A., "Transonic Potential Flow Calculations Using Conservation Form," Proceedings: AIAA 2nd Computational Fluid Dynamics Conference, June 1975, pp. 148-161.

8. Melnik, R.E., "Wake Curvature and Trailing Edge Interaction Effects in Viscous Flow Over Airfoils," Advanced Technology Airfoil Research Conference, NASA CP-2045, Part 1, 1978.

9. Rott, N. and Crabtree, L.F., "Simplified Laminar Boundary-Layer Calculations for Bodies of Revolution and for Yawed Wings," J. Aeron. Sci. Vol. 19, 1952.

10. Green, J.E., Weeks, D.J., and Brooman, J.W.F., "Prediction of Turbulent Boundary Layers and Wakes in Compressible Flow by a Lag-Entrainment Method," British ARC, R&M No. 3791, 1977.

11. Melnik, R.E., "Recent Developments in a Boundary Layer Theory for Computing Viscous Flows Over Airfoils," paper presented at USAF/FRG Data Exchange Meeting, Meersberg, Germany, April 1979.

12. Bauer, F., Garabedian, P., and Korn, D., Supercritical Wing Sections, Lecture Notes in Economics and Mathematical Systems, No. 66, Springer-Verlag, 1972.

13. Bavitz, P.C., "An Analysis Method for Two-Dimensional Transonic Viscous Flow," NASA TN D-7718, 1975.

14. Carlson, L.A., "Inverse Transonic Airfoil Design Including Viscous Interaction," Advances in Engineering Sciences, NASA CP-2001, 1976.

15. Bauer, F., Garabedian, P., Korn, D., and Jameson, A., "Supercritical Wing Sections II," Springer-Verlag, New York, 1975.

16. Lock, R.C., "Research in UK On Finite Difference Methods for Computing Steady Transconic Flows," Symposium Transsonicum II, Springer-Verlag, New York 1975.

17. Collyer, M.R., "An Extension to the Method of Garabedian and Korn for the Calculation of Transonic Flow Past an Aerofoil to Include the Effect of a Boundary Layer and Wake," British ARC, R&M No. 3328, 1978.

18. Collyer, M.R. and Lock, R.C. "Prediction of Viscous Effects in Steady Transonic Flow Past an Aerofoil," Aeronautical Quarterly, Vol XXX, August 1979.

19. Lock, R.C., "The Prediction of Viscous Effects on Aerofoils in Transonic Flow," British RAE TM Aero 1780, Sept. 1978.

20. Deiwert, G.S., "Computation of Separated Transonic Turbulent Flow," AIAA J., Vol. 14, 1976.

21. Thwaites, B., Incompressible Aerodynamics, Oxford University Press, 1960.

22. Baldwin, B.S. and Lomax, H., "Thin Layer Approximation and Algebraic Model for Separated Turbulent Flows," AIAA 16th Aerospace Sciences Meeting, Paper No. 78-257, Jan. 1978.

23. Steger, J.L., "Implicit Finite Difference Simulation of Flow About Arbitrary Geometries," AIAA J., Vol. 16, No. 7, July 1978, pp. 679-686.

24. Mahgoub, H.E.H. and Bradshaw, P., "Calculation of Turbulent-Inviscid Flow Interactions with Large Normal Pressure Gradients," AIAA J. Vol. 17, No. 10, October 1979, pp. 1025-1029.

25. Mellor, G.L., "The Large Reynolds Number Asymptotic Theory of Turbulent Boundary Layers," Int. J. Engr. Sci., Vol. 10, 1972.

26. Bush, W.B. and Fendell, F., "Asymptotic Analysis of Turbulent Boundary Channel and Boundary Layer Flow," J. Fluid Mech., Vol. 56, 1972.

27. Yajnik, K., "Asymptotic Theory of Turbulent Shear Flows," J. Fluid Mech., Vol. 42, 1970.

28. Afzal, N., "A Higher Order Theory for Compressible Turbulent Boundary Layers at Moderately Large Reynolds Numbers," J. Fluid Mech., Vol. 57, 1973.

29. Lighthill, M.J., "On Displacement Thickness," J. Fluid Mech., Vol. 4, 1958.

30. Stüper, J., "Auftriebsverminderung eines Flügels durch seinen Widerstand," Z.F.M., Vol. 24, 1933, pp. 439-441.

31. Pinkerton, R.M., "Calculated and Measured Pressure Distributions over the Midspan Section of NACA 4412 Airfoil," NACA TR-563, 1936.

32. Nitzberg, G.E., "The Theoretical Calculation of Airfoil Section Characteristics at Large Reynolds Numbers," A.C.R. 4112, 1944.

33. Preston, J.H., "The Calculation of Lift Taking Account of the Boundary Layer," British ARC, R&M 2725, 1949.

34. Preston, J.H., and Sweeting, N.E., "The Experimental Determination of the Boundary Layer and Wake Characteristics of a Simple Joukowski Aerofoil with Particular Reference to the Trailing Edge Region," British ARC, R&M 1998, 1943.

35. Preston, J.H., "Note on the Circulation in Circuits Which Cut the Wake of an Airfoil at Right Angles," British ARC, R&M 2957, 1954.

36. Spence, D.A. and Beasley, J.A., "The Calculation of Lift Curve Slopes, Allowing for Boundary Layer, with Application to the RAE 101 and 104 Aerofoils," British ARC, R&M 3137, 1960.

37. Firmin, M.C.P., "The Calculation of Pressure Distribution, Lift and Drag, on Single Aerofoils at Subcritical Speeds. Part I Interim Method," British RAE TR 72235, 1973.

38. Hall, M.G. and Firmin, M.C.P., "Recent Developments in Methods for Calculating Transonic Flows over Wings," ICAS Paper 74-18, 1974.

39. Lock, R.C., "Calculation of Viscous Effects on Aerofoils in Compressible Flow," paper presented at Fifth Australian Conference on Hydraulics and Fluid Mechanics, Dec., 1974.

40. Stewartson, K., "On the Flow Near the Trailing Edge of a Flat Plate II," Mathematika, Vol. 16, 1969, pp. 106-121.

41. Jobe, C.E. and Burggraf, O.R., "The Numerical Solution of the Asymptotic Equations of Trailing-Edge Flow," Proc. Roy. Soc. Series A Vol. 340, 1974, pp. 91-111.

42. Veldman, A.E.P. and van de Vooren, A.I., "Drag of a Finite Flat Plate," Proceedings of the Fourth International Conf. on Numerical Methods in Fluid Dynamics, Springer-Verlag, New York, 1975.

43. Brown, S.W. and Stewartson, K., "Trailing Edge Stall," J. Fluid Mech., Vol. 42, 1970.

44. Chow, R. and Melnik, R.E., "Numerical Solutions of the Triple Deck Equations for Laminar Trailing Edge Stall," Proceedings of the Fifth International Conference on Numerical Methods in Fluid Dynamics, Springer-Verlag, New York 1976.

45. Robinson, J.L., "Similarity Solutions in Several Turbulent Shear Flows," National Physical Lab., Rept. NPL Aero-1242, 1967.

46. Alber, I.E., "The Turbulent Wake of a Thin Flat Plate," Paper No. 79-1545, AIAA 12th Fluid and Plasma Dynamics Conf., July 1979.

47. Melnik, R.E. and Grossman, B., "Analysis of the Interaction of a Weak Normal Shock Wave with a Turbulent Boundary Layer," AIAA Fluid and Plasma Dynamics Conference, Paper No. 74-598, June 1974.

48. Melnik, R.E. and Grossman, B., "Further Developments in an Analysis of the Interaction of a Weak Normal Shock Wave with a Turbulent Boundary Layer," Symposium Transsonicum II, Springer-Verlag, New York, 1975 (Also issued as Grumman Research Department Report RE 511J, November 1975).

49. Adamson, T.C. Jr. and Feo, A., "Interaction Between a Shock Wave and a Turbulent Boundary Layer in Transonic Flow," SIAM J. Appl. Math., Vol. 29, 1975, pp. 121-145.

50. Melnik, R.E. and Grossman, B., "Interactions of Normal Shock Waves with Turbulent Boundary Layers At Transonic Speeds," in Transonic Flow Problems in Turbomachinery, Hemisphere Publ. Co., 1977 (also issued as Grumman Research Department Report RE 517J, 1977)

51. Adamson, T.C. Jr. and Messiter, A.F., "Normal Shock Wave - Turbulent Boundary Layer Interactions in Transonic Flow near Separation," in Transonic Flow Problems in Turbomachinery, Hemisphere Publ. Co., 1977, pp. 392-414

52. Messiter, A.F., "Interaction Between a Normal Shock Wave and a Turbulent Boundary Layer at High Transonic Speeds, Part I: Pressure Distribution," ZAMP, Vol. 31, May 1979, pp. 205-226.

53. Liou, M.S. and Adamson, T.C. Jr., "Interaction Between a Normal Shock Wave and a Turbulent Boundary Layer at High Transonic Speeds, Part II: Wall Sheer Stress," ZAMP, Vol. 31, May 1979, pp. 227-246.

54. Inger, G.R. and Mason, W.H., "Analytical Theory of Transonic Normal Shock - Turbulent Boundary Layer Interaction," AIAA J., Vol. 14, Sept. 1976, pp. 1266-1272.

55. Panaras, A.G. and G.R. Inger, "Transonic Normal Shock - Turbulent Boundary Layer Interaction in Pressure Gradient Flows," ASME Paper 77-GT-34, March 1977.

56. Lighthill, M.J., "On Boundary Layers and Upstream Influence, II - Supersonic Flows Without Separation," Proc. Royal Soc. Series A, Vol. 217, 1953.

57. Viviand, H., "Application des Methodes Asymptotiques a L'etude des Couches Visqueuses Libres," La Recherche Aerospatiale, No. 431, July-Aug. 1969, pp. 17-21.

58. Van Dyke, M., Perturbation Methods in Fluid Mechanics, 2nd Ed., The Parabolic Press, Stanford, Calif. 1975.

59. Horlock, J.H. and Lakshminarayana, A.B., "Secondary Flow: Theory, Experiment and Application in Turbomachinery Aerodynamics," Annual Reviews of Fluid - Mechanics, Vol. 5, Annual Reviews Inc., Palo Alto, Calif. 1973.

60. Gakhov, F.D., Boundary Value Problems, Addison-Wesley, Reading, 1966.

61. Thwaites, B., "Approximate Calculation of the Laminar Boundary Layer," Aeron. Quart., Vol. 1, 1969.

62. Crabtree, L.F., "Prediction of Transition in the Boundary Layer on an Aerofoil," J. Roy. Aeron. Soc., Vol. 62, July 1958.

63. Michel, R., "Determination of Transition Point and Calculation of Drag of Wing Sections in Incompressible Flow," Publication No. 58 ONERA, 1958.

64. Stevens, W.A., Goradia, S.H., and Braden, J.A., "Mathematical Model for Two-Dimensional Multi-Component Airfoils in Viscous Flow," NASA CR-1843, July 1971.

65. Schlichting, H., Boundary Layer Theory, Sixth edition, McGraw Hill, New York, 1968, pp. 640-642.

66. Maise, G. and McDonald, H., "Mixing Length and Kinematic Eddy Viscosity in a Compressible Boundary Layer," AIAA J., Vol. 6, No. 1, Jan. 1968.

67. Alber, I.E. and Coats, D.E., "Analytical Investigations of Equilibrium and Non-equilibrium Compressible Turbulent Boundary Layers," AIAA J., Vol. 9, No. 5, May 1971.

68. Hunter, L.G. and Reeves, B.L., "Results of a Strong-Interaction, Wake-Like Model of Supersonic Separated and Reattaching Flows," AIAA J., Vol. 9, 1971.

69. Mead, H.R. and Melnik, R.E., "GRUMFOIL: A Computer Code for the Viscous Transonic Flow Over Airfoils," NASA CR-3806, 1985.

70. Cook, P.H., McDonald, M.A., and Firmin, M.C.P., "Airfoil RAE 2822 Pressure Distributions and Boundary Layer Measurements," in Experimental Data Base for Computer Program Assessment, AGARD-AR-138, 1979.

71. Thibert, J.J., Grandjacques, M., and Ohman, L., "NACA 0012 Airfoil" in Experimental Data Base for Computer Program Assessment, AGARD-AR-138, May 1979.

72. Freuler, R.J. and Gregorek, G.M., "An Evaluation of Four Single Element Airfoil Methods," in Advanced Technology Airfoil Research, NASA CP-2045, Part I, 1978.

73. Kacprzynski, J.J., "A Second Series of Wind Tunnel Tests, Shockless Lifting Airfoil No. 1," NAE Project Report 5X5/0062, 1972.

74. Smith, A.M.O. and Cebeci, T., "Remarks on Methods for Predicting Viscous Drag in Aerodynamic Drag," AGARD CP-124, 1973.

75. Mokry, M. and Ohman, L.H., "Application of the Fast Fourier Transform to Two-Dimensional Wind Tunnel Wall Interference," J. of Aircraft, Vol. 17, No. 6, 1980.

76. Ohman, L.H., Kacprzynski, J.J., and Brown, D., "Some Results from Tests in the NAE High Reynolds Number Two-Dimensional Test Facility on Shockless and other Airfoils," Canadian Aero. and Space J., Vol. 19, 1973.

77. Swafford, T.W., "Calculation of Skin Friction in Two-Dimensional, Transonic Turbulent Flow," AEDC TR-79-12, April 1979.

78. East, L.F. Smith, P.D., and Merryman, P.J., "Prediction of the Development of Separated Turbulent Boundary Layers by the Lag-Entrainment Method," British RAE, TR 77046, 1977.

79. Kuhn, G. and Nielsen, J.N., "Prediction of Turbulent Separated Boundary Layers," AIAA J., Vol. 12, No. 7, 1974.

80. Carter, J.E., "A New Boundary-Layer Inviscid Interaction Technique for Separated Flow," Proceedings: AIAA Computational Fluid Dynamics Conference, July 1979, pp. 45-55.

81. LeBalleur, J.C., "Couplage Visueux - Non Visqueux: Analyse du Probleme Incluant Decollements et Ondes de Choc," Rech. Aerosp. No. 1977-6, pp. 340-358.

82. LeBalleur, J.C., "Couplage Visquex - Non Visquex: Methode Numerique et Applications aux Ecoulements Bidimensionnels Transsoniques et Supersoniques," Rech. Aerosp. No. 1978-2, pp. 65-76.

83. Melnik, R.E., Mead, H.R., and Jameson, A., "A Multi-Grid Method for the Computation of Viscid/Inviscid Interaction on Airfoils," AIAA 21st Aerospace Sciences Meeting, Paper AIAA 83-0234, January 1983.

1. Report No.	2. Government Accession No.	3. Recipient's Catalog No.
NASA CR-3805		

4. Title and Subtitle	5. Report Date
AN IMPROVED VISCID/INVISCID INTERACTION PROCEDURE FOR TRANSONIC FLOW OVER AIRFOILS	October 1985
	6. Performing Organization Code
7. Author(s)	8. Performing Organization Report No.
R. E. Melnik, R. R. Chow, H. R. Mead, and A. Jameson	RE-682
	10. Work Unit No.
9. Performing Organization Name and Address	
Grumman Aerospace Corporation Bethpage, NY 11714	11. Contract or Grant No. NAS1-12426
	13. Type of Report and Period Covered
12. Sponsoring Agency Name and Address	Contractor Report
National Aeronautics and Space Administration Washington, DC 20546	14. Sponsoring Agency Code 505-31-13-01

15. Supplementary Notes

Langley Technical Monitors: Jerry C. South, Jr., and Frank C. Thames
Final Report

16. Abstract

This paper describes a new interacting boundary-layer approach for computing the viscous transonic flow over airfoils. The theory includes a complete treatment of viscous-interaction effects induced by the wake and accounts for normal pressure gradient effects across the boundary layer near trailing edges. The method is based on systematic expansions of the full Reynolds equation of turbulent flow in the limit of Reynolds numbers, $Re \to \infty$. The theory employs a local inner solution to describe the strong interaction region at trailing edges. Procedures are developed for incorporating the local trailing-edge solution into the numerical solution of the coupled full-potential and integral boundary-layer equations. Although the theory is strictly applicable to airfoils with cusped or nearly-cusped trailing edges and to turbulent boundary layers that remain fully attached to the airfoil surface, the method has been successfully applied to more general airfoils and to flows with small separation zones. Comparisons of theoretical solutions with wind-tunnel data indicate the present method can accurately predict the the section characteristics of airfoils including the absolute levels of drag.

17. Key Words. (Suggested by Author(s))	18. Distribution Statement
Viscous Transonic Flow Airfoils Viscid/Inviscid Interaction	Unclassified - Unlimited Subject Categories 02 and 34

19. Security Classif. (of this report)	20. Security Classif. (of this page)	21. No. of Pages	22. Price
Unclassified	Unclassified	132	A07

N-305

For sale by the National Technical Information Service, Springfield, Virginia 22161

NASA-Langley, 1985

National Aeronautics and
Space Administration
Code NIT-3

Washington, D.C.
20546-0001